Development of Three Dimensional Human Skin Equivalents Based on Decellularized Extracellular Matrix and Tyrosine-Derived Polycarbonate Polymers for In-Vitro Drug Screening Applications

By

PEI-CHIN TSAI

A Dissertation Submitted to the Graduate School- New Brunswick

Rutgers, The State University of New Jersey

In partial fulfillment of the requirements for the degree of

Doctor of Philosophy

Graduate Program in Pharmaceutical Sciences

Written under the direction of

Professor Bozena Michniak-Kohn, Ph.D.

And approved by

_____

_____

_____

_____

New Brunswick, New Jersey

May, 2016

ABTRACT OF THE DISSERTATION

Development of Three Dimensional Human Skin Equivalents based on Decellularized Extracellular Matrices and Tyrosine-Derived Polycarbonate Polymers for *In-Vitro* Drug Screening Applications

By PEI-CHIN TSAI

Dissertation Director:

Professor Bozena Michniak-Kohn

Three-dimensional (3D) human skin equivalents (HSEs) are *in-vitro* models that have morphology and function similar to native human skin. Traditionally, drug discovery for lead compounds rely on conducting efficacy and safety studies through 2D monolayer culture. However, the lack of similarly of 2D monolayer culture to those of *in-vivo* conditions often leads to failure in later development stages. 3D skin equivalents are more complex in terms of structures and functions. They mirror the environment experienced by the normal cells in the body, reflecting cell-cell interaction, cell-matrix interaction, drug response and thus may be potential tools for drug screening.

In this study, development of full-thickness HSEs through novel scaffold materials has been investigated. One approach was to use the top-down approach, in which decellularized matrices obtained and treated from native porcine peritoneal tissues were being investigated as matrix scaffolds to construct HSEs. The second approach was to use the bottom-up approach, where biodegradable tyrosine-derived polymers synthesized at the New Jersey Center of Biomaterials (NJCBM) were electrospun into fibrous porous scaffolds.

Scaffold morphological and mechanical properties were analyzed. Decellularized porcine peritoneal matrix was shown to possess similar Young's Modulus compared to human cadaver skin. Cell-matrix interactions between human dermal cells and various scaffolds were studied using viability assays and fluorescent microscopy imaging. Both decellularized peritoneal matrices and poly(DTE carbonate) scaffolds showed cellular compatibility to human dermal cells. Later, various HSEs models of co-cultured human dermal fibroblasts and human keratinocytes were developed. Differentiated multiple epithelial layers were observed on the models and keratinocyte proliferation markers (i.e., keratin15) and the presence of keratinocyte differentiation markers (i.e., involucrin) were recorded. From the functional aspect, decellularized matrix based-HSEs were able to predict skin irritation *in-vitro*. The model differentiated non-irritant from irritant compounds based on cell viability and multiple cytokine secretions (i.e., IL-1α, IL-1ra, IL-6, IL-8 and GM-CSF).

In conclusion, decellularized extracellular matrices and tyrosine-derived polycarbonate scaffolds are promising matrices for the culture of 3D HSEs constructs. The future development of decellularized extracellular matrix and tyrosine-derived polycarbonate scaffolds-based HSEs will offer more useful applications in drug discovery and drug development in pharmaceutical industries.

Dedication

To my parents:

Mom, you were the one who inspired me to do research in science.

Dad, you were the one who encouraged me to pursue a Ph.D degree.

To my husband:

Zhao-Jun, who walked me through this journey with love and support.

Without them, this would not have been possible.

Acknowledgement

I would like to express my deepest gratitude to my Ph.D. advisor Dr. Bozena Michniak- Kohn, who gave me the opportunity to work in a highly interdisciplinary research center where I encountered many innovative projects and industrial collaborations. Over the past five years, she encouraged me to explore my own career/research interests and gave me the opportunity to grow.

I would like to thank Dr. Zheng Zhang, a true mentor and a cheerful friend. There were countless weekends that we discussed manuscripts and book chapters through e-mail communications. I couldn't have finished the Ph.D program, if it wasn't for Dr. Zheng Zhang who told me not to give up at those times when I had doubts.

I would like to thank Dr. Charles Florek, a wonderful industrial collaborator who involved greatly with the decellularized-HSEs work. In addition, he constantly encouraged me, gave many feedbacks and put effort in seeking funding from DSM for this project.

I would like to thank Dr. Tamara Minko and Dr. Leonid Kagan for being part of my committees and also giving me opportunity to be a Teaching Assistant in their courses. Without the assistantship from them and the Department of Pharmaceutics, I would not be able to finish my PhD studies.

I would like to thank my friends and colleagues at Laboratory of Drug Delivery (LDD): Tannaz Ramezanli, Dina Wadie, Golshid Keyvan, Mania Dorrani, and Krizia Karry for all the support and growing together. The lab will be different without them. I would like to thank Manting Chiang for reading this thesis work.

Great appreciation to all the collaborators Dr. Serom Lee, Dr. Jean Lo, Dr. Anandika Dhaliwal, Dr. Xiao-Li Sun, Dr. Rajani Bhat, Dr. Pietrangelo, and Dr. Oluwatoyin Adeleke for together publishing manuscript and review papers.

This research was sponsored by DSM, Center for Dermal Research, and New Jersey Center for Biomaterials.

Table of Contents

List of Tables

List of Figures

List of Abbreviations

Roman letters

ACN	acetonitrile
3D	three-dimensional
ANOVA	analysis of variance
DCM	dichloromethane
DMEM	Dulbecco's Modified Eagle Medium
DMF	dimethyl formamide
DMSO	dimethyl sulfoxide
DTE	desaminotyrosyl-L tyrosine ethyl ester
ECM	extracellular matrix
EDTA	ethylenediaminetetraacetic acid
EGF	epidermal growth factor
ELISA	Enzyme-linked immunofluorescent assay
FBS	fetal bovine serum
FGF	fibroblasts growth factors
H&E	hematoxylin & eosin
HaCaT	spontaneously transformed immortal human keratinocytes
HDF	human dermal fibroblasts
HEKn	primary neonatal human keratinocytes
HFP	hexafluoroisopropanol
HPLC	high performance liquid chromatography
HSEs	human skin equivalents

IGF-I	insulin-like growth factor-I
Mn	number average molecular weight
Mw	weight average molecular weight
MW	molecular weight
NaOH	sodium hydroxide
NJCBM	New Jersey Center for Biomaterials
OECD	Organisation for Economic Co-operation and Development
PBS	phosphate buffered saline
PDI	polydispersity index
RA	retinoic acid
SEM	scanning electron microscopy
TCPS	tissue cultured polystyrene
TFA	trifluoroacetic acid
Tg	glass transition temperature
TGF-α	transforming growth factor alpha
THF	tetrahydrofuran

Units

uL	microliters
mL	milliliters
um	micrometers
mg	milligrams

cm	cetermeters
hr	hours
rpm	rate per minute
	weight per volume
w/v	percent
	volume per volume
v/v	percent
w/w	weight per weight percent
MPa	megapascal
kV	kilovolts
mm	millimeters
min	minute
C	degree Celcius

1 Chapter 1. Introduction and Specific Aims

1.1. Introduction

There is a general need for better *in-vitro* models to facilitate the discovery of new drugs and formulation development in the pharmaceutical industry. Many molecules that show high efficacy in two-dimensional (2D) monolayer cell cultures tend to fail in later animal or clinical studies, thus providing misleading toxicological and efficacy data. This failure is often due to the oversimplified structure of 2D monolayer cell cultures that do not fully represent the *in-vivo* conditions. Three-dimensional (3D) tissues offer higher complexity, which correlate more closely with *in-vivo* conditions. Many of these screening methods utilizing 3D systems have been adopted for toxicology studies.

However, a 3D tissue that mimics *in-vivo* skin architecture and functions fully remains a challenge and has not yet been achieved. Although many of the current models can generate stratified epidermal structures, the barrier functions are still different from native human skin. A single skin tissue model that has all the skin structures (hair follicles, sweat glands, neurons) is still not available. In addition, reliable, robust and validated *in-vitro* drug screening assays using 3D skin tissue are still under investigation.

In our study, we intend to construct full-thickness skin models by using innovative scaffold materials (i.e., decellularized matrices and biodegradable polymers). The use of decellularized material is a “top-down” approach, where native skin tissues are being treated to leave behind scaffolds of connective tissue. These scaffolds are then repopulated with various types of dermal cells to regenerate full-thickness HSEs. On the other hand, the use of biodegradable polymers (i.e., poly(DTE carbonate)) is the “bottom-

up" approach, where the polymers will be electrospun into fibrous scaffolds that will then be repopulated with dermal cells.

The functions of constructed HSEs will be tested to see the potential applications for drug screening. Functional endpoints such as cell viability and cytokine secretions of the assay will be determined. Ultimately, we intend to generate fully function HSEs that are based on innovative biomaterials to facilitate the discovery of drug candidates and support the further development of drug products in the pharmaceutical industry.

1.2. Specific Aims

The ultimate goal of this study is to develop and optimize human skin equivalents from various scaffolds to establish screening tools for pharmaceutical drug development. In order to reach our goal, this research has been divided into three major aims:

Specific Aim 1: *To investigate the use of decellularized matricies as dermal scaffolds to establish human skin equivalents.*

Investigate the use of decellularized matrices to establish HSEs. We aim to study the effect of different parameters such as keratinocyte cell types, cell seeding positions, cell seeding methods and media composition on the HSE models.

Specific Aim 2: *To explore the ability of decellularized matrix-based full-thickness HSEs to predict in-vitro skin irritation of compounds. Study the cellular response of human dermal cells on a decellularized matrix and characterize epithelial structures in*

established human skin equivalents. In addition, the functional aspect of the cultured HSEs will be validated.

We plan to study the attachment and viability of human dermal cells on different surfaces of the decellularized matrices. HSEs will be contructed by co-culturing keratinocytes and fibroblasts on the matrices and the models will be characterized using histology and immnohistochemical staining to evaluate the epithelial development.

The *in-vitro* applications (i.e., screening *in-vitro* skin irritation) of HSEs will be investigated. The cell viability and secretion of pro-inflammatory cytokines will be measure following topical application of selected chemicals to the HSEs.

Specific Aim 3: *To fabricate poly(DTE carbonate) polymeric scaffolds using electrospinning techniques. We will investigate the cellular response on electrospun polymeric scaffolds and characterize the morphology and architecture of constructed polymeric-based HSEs.*

Poly(DTE carbonate) will be electrospun into fibrous scaffolds. The scaffolds fibers and pore size in the mesh will be characterized using scanning electron microscopy. Tensile strength properties will be determined by mechanical testing and surface properties will be evaluated by contact angle measurement. Human dermal cell attachment and viability on the electrospun scaffolds will be examined using confocal microscopy. Epithelial development of poly(DTE carbonate)-HSEs will be monitored by histology and by staining for keratinocyte proliferation and differentiation markers.

Chapter 2. Background and Significance

2.1. Human Skin

Skin, the largest organ in the body, functions as a protective barrier as well as maintains fluid homeostasis, provides thermoregulation of the human body, mediates sensory detection and is the major site for transdermal and topical delivery of actives. Human skin consists of three major layers: (a) the epidermal layer, which is mainly composed of proliferated and differentiated keratinocytes and (b) an underlying dermal layer that is rich in fibroblasts, connective tissue and (c) hypodermal layer that consists of adipocytes and blood vessels (Figure 2.1).

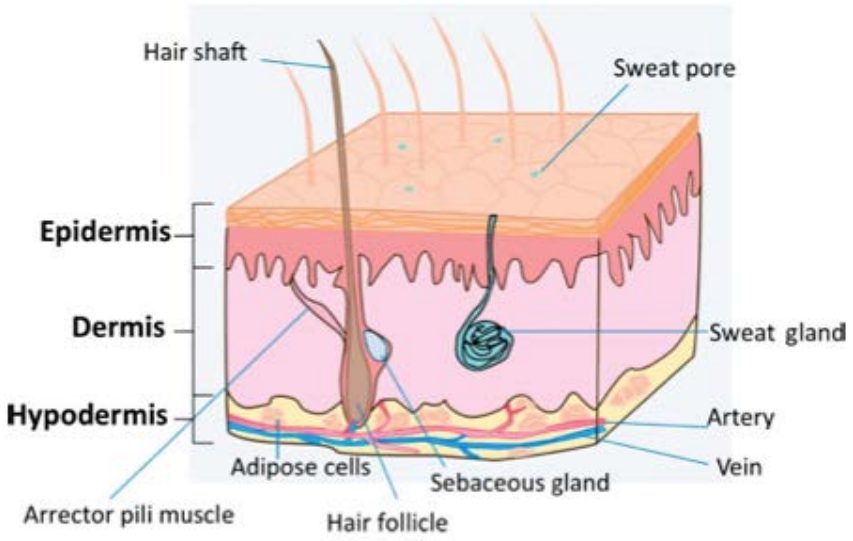

Figure 2.1 Schematic image of human skin consisting the three major layers (a) epidermis, (b) dermis and (c) hypodermis. The appendages such as hair shaft, hair follicle, sweat gland, sebaceous gland and arrector pilli muscle are illustrated. [1]

The epidermis is a stratified squamous epithelium and is divided into sub-layers: *stratum basale, stratum spinosum, stratum granulosum, and stratum corneum* (Figure

2.2). The *stratum basale* is located right above the basement membrane that connects the epidermis and dermis. The basal layer is responsible for the constant renewal of the skin cells (the turnover takes approximately 40 to 56 days and is dependent on age), based on constant mitosis of the basal cells.[2] As the keratinocytes move outwards and upwards, they begin to generate daughter cells. The daughter cells then begin to differentiate, flatten their nuclei and produce lamellar bodies to form the *stratum spinosum*. As the journey of the cells continues, the *stratum granulosum*, a layer above the *stratum spinosum* is formed. The granular layer contains anucleated keratinocytes that have only granular cytoplasm and the extracellular space between the cells is filled with the lamellar bodies that were released through exocytosis. In the final stage of keratinocyte differentiation, the cells reach the outermost layer, the *stratum corneum.* The cytoplasm of the cells in the *stratum corneum* is rich in keratin and the cells are surrounded by intercellular lipids, forming “brick and mortar” structures. The *stratum corneum* contains about 40% protein, 40% water and 18-20% of lipids and forms the major barrier in skin for the transport of actives.[3]

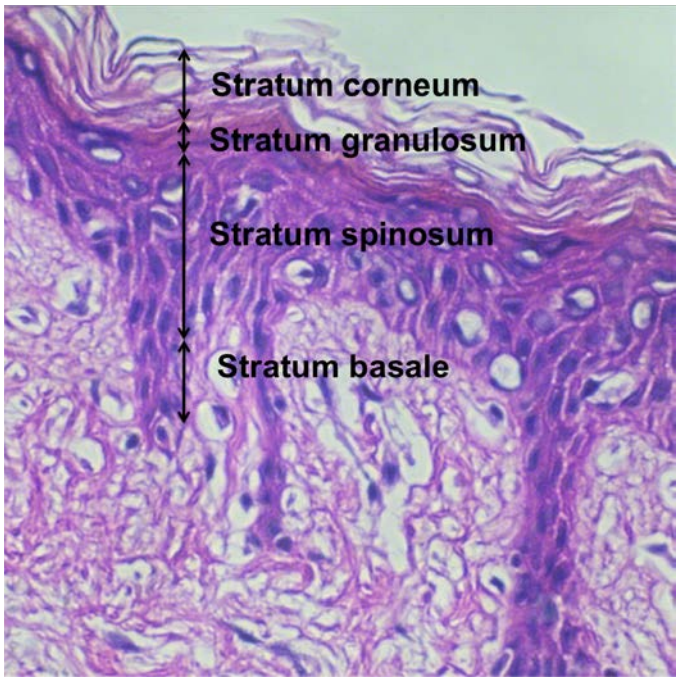

Figure 2.2 Histological H&E images indicating the four sub-layers of epidermis, *stratum corneum, stratum granulosum, stratum spinosum, stratum basale*.

Beneath the epidermis lies the dermis that is 3 to 5 mm thick, supporting the overlying epidermis and consists of fibroblasts in an extracellular matrix (ECM) of woven fibrous proteins. The dermis is divided into two layers, (1) papillary dermis which is superficial and contains blood vessels which provide nutrition for the epidermis above, and (2) the reticular dermis, which is thicker and contains sebaceous glands, sweat glands, hair follicles, blood vessels, lymph vessels and nerve endings. Overall, the dermis is a hydrophilic compartment of skin and is the systemic absorptions site for many drugs. On the other hand, the hypodermis is a subcutaneous layer with loose connective tissues that lies under the dermis. This layer is rich in fibroblasts, adipose cells and macrophages and fat. The subcutaneous layer regulates body temperature and provides a protective padding for organs. In addition, the fat layer acts as a reservoir site for many hydrophobic drugs.

2.2. Human Skin Equivalents (HSEs)

Human skin equivalents (HSEs) are *in-vitro* skin models that are intended to resemble native skin, both in anatomy and functions. These models are critical to pre-clinical drug development and can be utilized as screening tools to aid the selection of lead drug candidates. They provide alternative models for testing drug safety and efficacy in addition to cell culture and animal models. Different types of HSEs and their *in-vitro* applications are discussed below.

2.2.1. Reconstructed Human Epidermis (RHE)

Reconstructed Human Epidermis (RHEs) consists of differentiated keratinocytes cultured on acellular inert filter substrates. For example, SkinEthic™ (Episkin, France) is a commercially available RHE that consists of normal human keratinocytes on an inert polycarbonate filter; Episkin™ (Episkin, France) and EpiDerm™ (MatTek, Ashland, USA) consists of normal human keratinocytes on a collagen matrix (Figure 2.3). The commercially available RHE models exhibit a multistratified epidermis, expression of epidermal differentiation markers (e.g., Keratin K1, loricrin, filaggrin) and skin lipids (e.g., phospholipids, cholesterol, triglycerides and ceramides).

Figure 2.3 Histological image of commercially avaliable reconstructed human epidermis, SkinEthic™ (Episkin, France), Episkin™ (Episkin, France), EpiDerm™ (MatTek, Ashland, USA).

The RHEs have been validated for *in-vitro* skin corrosion and irritation studies under OECD TG431 and 439 guidelines, respectively. However, their usefulness for *in-vitro* permeation testing still remains questionable. Although these models possess a differentiated *stratum corneum*, these epidermis-only skin equivalents have inferior barrier properties if compared with normal human skin.[4] Schmook et al.[5] compared the permeation profiles of drugs with different hydrophilicities using commercially available RHEs, SkinEthic™ (Episkin, France) to those of human, rat and porcine skin. The authors found that the flux for relatively hydrophilic compound (salicylic acid) was comparable to human skin. However, for more hydrophobic drugs such as clotrimazole and hydrocortisone, the flux was about 900 and 200 fold higher, respectively. In another study, a commercially available RHE, EpiDerm™ (MatTek, Ashland, USA) revealed a five times higher flux compared to heat-separated human epidermis in a permeability study using flufenamic acid (lipophilic model drug).[6] In general, it is considered that RHEs exhibit higher permeability compared to that of human epidermis. Although the flux value is being overestimated, the RHEs could differentiate the relative ranking of the compounds. A validation study performed by ten laboratories demonstrated that the ranking of a wide spectrum of test substances (mannitol, benzoic acid, caffeine, nicotine, digoxin, flufenamic acid, testosterone, clotrimazole, ivermectin) permeating through three RHE models, Episkin (Episkin, France), EpiDerm™ and SkinEthic™ could reflect the permeation through human epidermis under both infinite and finite dose conditions.[4] In addition, the obtained permeation data had a tendency toward lower variability compared with human epidermis.

2.2.2. Full-thickness HSEs

The full-thickness HSE models contain keratinocytes grown on a dermal substrate populated with fibroblasts to form epidermal and dermal compartments. The full-thickness models resemble native skin more than RHEs based on the increased complexity of the model. Recently, more advanced models that incorporate Langerhans cells (MUTZ-3)[7], neuron cells, and melanocytes to the HSEs have been developed (Figure 2.4). Disease models that include melanoma cells or a psoriatic epidermis have also been reported. The *in-vitro* applications widely range from investigation of cellular pathways and mechanism of disease models to characterization of drug permeation profiles.

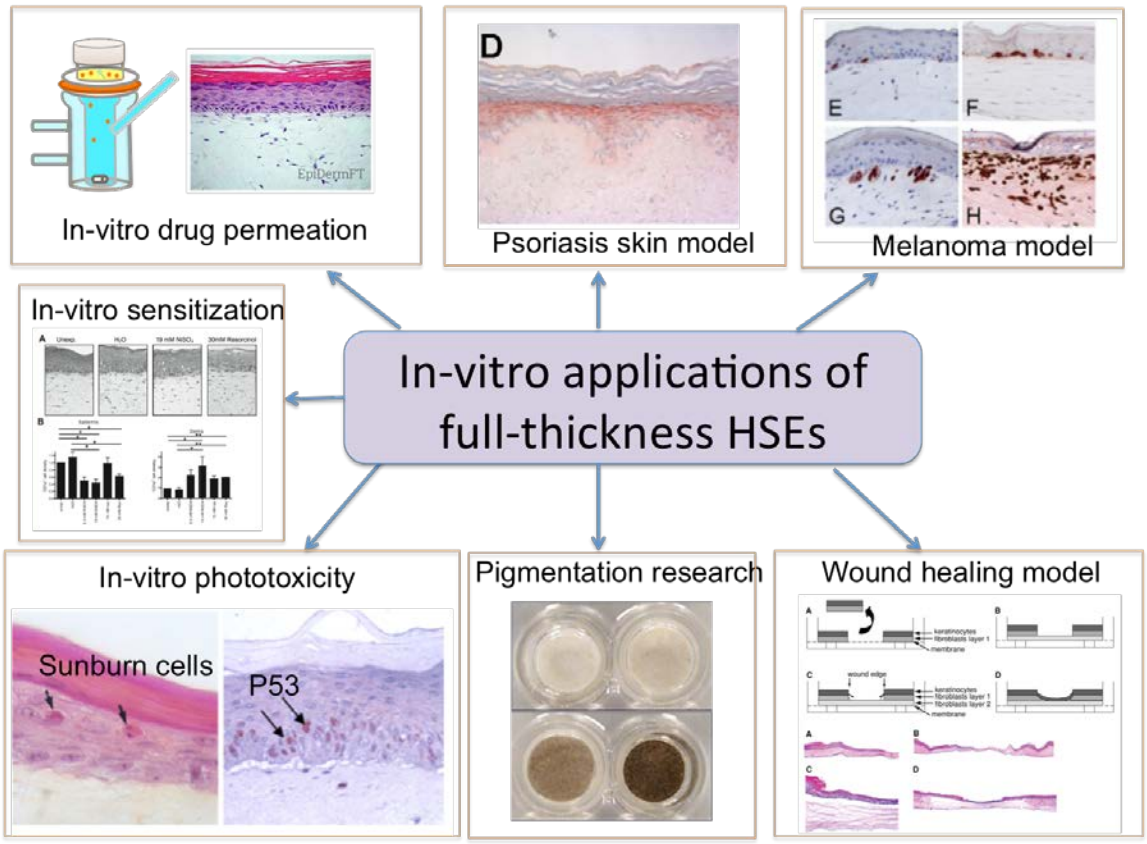

Figure 2.4 Examples of various full-thickness HSEs models and their applications.

Table 2.1 Reported full-thickness HSEs models for research.

Epidermal cells	Dermal cells	Dermis substrate	Application	Ref.
Primary human keratinocytes; MUTZ-3 LC	Primary human dermal fibroblasts	Collagen	Study cutaneous immune response	7
Human keratinocytes		De-epidermized abdominal dermis	Psoriatic skin model	8
Human keratinocytes	Primary human dermal fibroblasts; melanoma	Bovine type 1 collagen	Study melanoma progression	9
HaCaT	Primary human fibroblasts	Collagen	HSV disease model	10
Primary human keratinocytes	Primary human fibroblasts; human melanocytes	Bovine type 1 collagen	Study skin pigmentation	11
Primary human keratinocytes	Human fibroblasts	Bovine type 1 collagen	Wound healing model	12
Primary human keratinocytes	Human fibroblasts	Bovine type 1 collagen	*In-vitro* permeation testing	13
Primary human keratinocytes	Human fibroblasts; sensory neurons; HUVEC	Bovine type 1,3 collagen sponge	Study influence of neuron to wound healing	14

2.3. Materials for constructing HSEs scaffolds

2.3.1. Decellularized extracellular matrix (dECM)

Decellularized extracellular matrix (dECM) is an acellular tissue that has its cellular component removed. In 2001, researchers obtained skin tissue from human cadavers and mechanically removed the epidermis from the dermis using forceps to form “deepidermalized dermis (DED)”.[15] DED was investigated for wound healing therapy since the DED could potentially replace split-thickness skin grafts for many burn patients. The removal of the epidermis way minimize rejection in grafting and also leave behind

some basement membrane, collagen type IV and collagen type VII on the dermis that are essential for the reattachment and proliferation of host fibroblasts and keratinocytes.

Over the years, the decellularization techniques continue to be modified with more control of the decellularization process.[16] In addition to physical (e.g., agitation, freeze-thaw) removal of cellular and nuclear material in the tissue, chemical (e.g., Triton X-100) and enzymatic (e.g., trypsin) processes were investigated to obtain optimum decellularized scaffolds with desired architectures and ECM compositions (Figure 2.5).

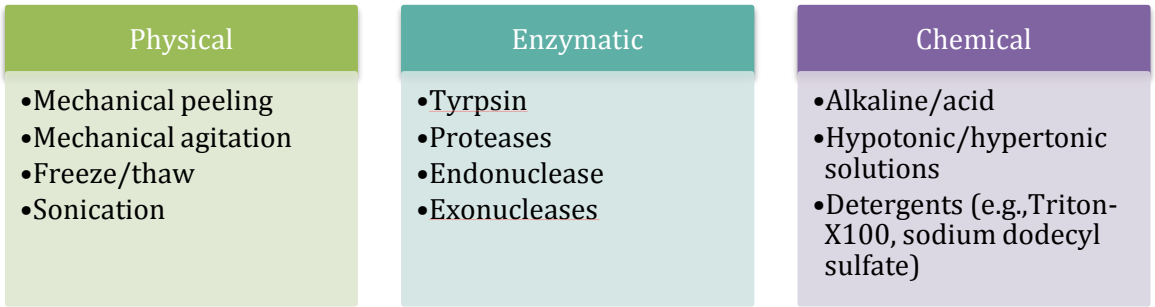

Figure 2.5 Examples of decellularization techniques to remove cellular and nuclear components from tissues.

Decellularized tissue are now often utilized in tissue regeneration, where commercially available acellular biological scaffolds such as porcine small intestinal mucosa (Oasis®; Cook Biotech), porcine dermis (Permacol™; Medtronic), cryopreserved human cadaver dermis (Alloderm®; LifeCell) and amniotic membrane (Aminograft®; Biotissue) have been used to treat partial thickness burns, skin wounds and diabetic ulcers. However, the use of more recent and advanced decellularized material as a dermal matrix to construct *in-vitro* skin models for drug screening has not been investigated.

2.3.2. Polymeric scaffolds

2.3.2.1. Natural polymers

Natural polymers are mostly derived from animal sources. The most common natural polymeric scaffold used for HSEs is type 1 collagen sponge or gel. The native dermis consists of 90% of type 1 collagen and it is essential compound for the connective tissue. Several commercially available HSEs based on type 1 collagen are available and include Integra (Integra LifeScience, USA), Apligraft® (Organogenesis, USA), OrCel® (Fortificell Bioscience, USA), and Matriderm® (Medskin Solutions, Germany).

Other natural materials such as silk[17], chitosan[18] and hyaluronic acid[19] have also been reported to successfully establish dermal scaffold for HSEs. Sericin, a silk obtained from cocoons was able to form porous scaffolds using a freeze-drying method followed by crosslinking with genipin. The histological analysis of constructed HSEs showed multi-layered stratified keratinocytes and the presence of involucrin and collagen IV. Chitosan, was reported to be cross-linked with collagen and glycosaminoglycan to form HSEs dermal scaffolds. The constructed HSEs also had stratified epidermis with the presences of lipid vesicles in spinous layer and keratohyalin granules in the *stratum granular* layer, showing high morphological equivalent to normal skin.[20] Hyaluronic acid, a glycosaminoglycan is a major component of the skin ECM. It is most abundant in the skin and accounts for around 50% of the total body hyaluronic acid. Commercial dermal substitute Hyalomatrix® (Anika Therapeutics, Italy) is a non-woven bi-layered fibrous pad made from derivative of hyaluronic acid.

2.3.2.2. Synthetic polymers

Synthetic polymers are attractive materials for constructing HSE due to their ability to tune the chemical and mechanical properties to achieve desired cellular responses, cell proliferation and differentiation. It has been reported in the literature that polycaprolactone, poly(lactic acid), poly(L-lactide)-poly(ethylene glycol), and polystyrene can be used for constructing scaffolds for HSEs. Human keratinocytes cultured on polycarbonate filter were able to generate reconstructed normal and pathological human epidermis.[21] Porous scaffolds from poly(lactic acid) were prepared by solid-lipid separation and particulate- leaching method.[22] The pore diameter could be controlled in turn affected cell proliferation and nutrition transport. Similarly, human fibroblasts were found to have significant progressive growth on electrospun poly(lactic acid-co-glycolic acid) scaffolds with fiber size of 350-1,100 nm diameter.[23] The fiber size affected the attachment and growth of the fibroblasts. Cui et al. also reported the use of electrospun poly(L-lactide)-poly(ethylene glycol) scaffolds for skin tissue engineering.[24] Different blending ratios of poly(L-lactide) and poly(ethylene glycol) resulted in varying surface hydrophilicity and degradation patterns.

2.4. The application of HSEs as *in-vitro* drug testing tools

During the development of a transdermal or topical drug product, a variety of *in-vitro* assays are utilized in the screening, selection and prediction of highly permeable compounds as well as during the optimization of suitable delivery systems. The early stage of development begins with the generation of libraries, target identification and lead optimization. These processes are often heavily based on a variety of *in-vitro* testing

including identifying lead compounds that exhibit high skin permeability, low irritability and low sensitizing properties (Figure 2.6). During the development phase, assays such as *in-vitro* drug permeation play an important role for evaluating a drug's efficacy and *in-vitro* drug release ensures quality and performance of a system. Other tests such as adhesion testing, tackiness and uniformity of dosage units are also some common tests used to ensuring quality of transdermal drug products.

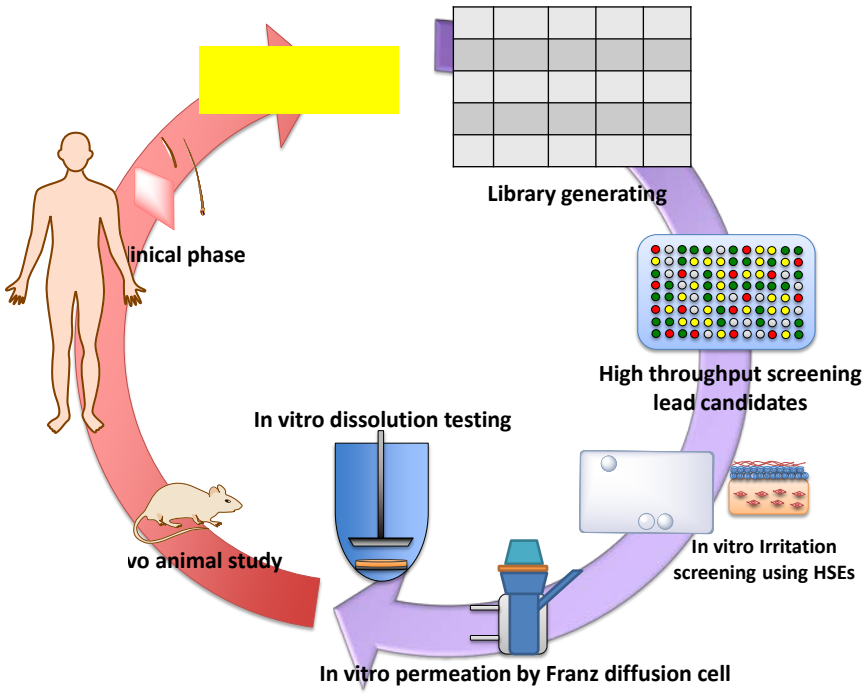

Figure 2.6 The discovery and development process for a transdermal drug product. HSEs= human skin equivalents.

2.4.1. Tools for accessing drug permeation through the skin

Much effort has been made in the past to establish RHEs and full-thickness HSEs for drug permeation testing (Table 2.2). Commercially available full-thickness models such as Graftskin™ LSE™ (Organogenesis, MA, USA), and Phenion FT® (Henkel Corp, Düsseldorf, Germany) have been evaluated for permeation testing. Schmook et al.[5] compared the permeation profile of terbinafine, clotrimazole, hydrocortisone and salicylic acid on Graftskin™ LSE™ and compared these data with those of SkinEthic™ (Episkin, France), human, porcine and rat skin. When compared to human skin, the full-thickness Graftskin™ LSE™ demonstrated an adequate barrier for salicylic acid. However, the HSEs had at least 1000 and 200 fold increase in flux for more hydrophobic drugs clotrimazole and hydrocortisone, respectively. In another study, Ackermann et al.[13] evaluated the use of full-thickness Phenion FT® as a percutaneous absorption model by comparing permeation of testosterone, caffeine, benzoic acid and nicotine with those on pig skin and RHEs (i.e., EpiDerm™, SkinEthic™, Episkin). Overall, the Phenion FT® was more permeable than pig skin but was comparable with RHEs for lipophilic compounds such as nicotine and testosterone. The authors suggested that the retarded flux of lipophilic compounds was the result of additional uptake and a reservoir formed in the dermis as well as the presence of different lipid patterns in the epidermis. In spite of the fact that Phenion FT® exhibited inferior barrier properties compared with pig skin, the reproducibility of the permeation profiles was still good.

Although the data suggests that RHEs and HSEs could potentially reflect the rank order of drug permeation and the reproducibility of RHEs and HSEs are often better than that for human skin, the major hurdle with the current HSE models lie in their over-

predicted permeability parameters compared to those from human skin. This could be caused by different lipid composition and organization of the *stratum corneum* in current HSEs models. For example, Thakoersing et al.[25] analyzed their in-house HSEs and found an increased presence of monosaturated fatty acids and hexagonal lipid packing in their *stratum corneum.* This could be contributing to the lower barrier properties of HSEs. However, Batheja et al.[26] optimized HSE growth conditions with the addition of clofibrate, fatty acids and ascorbic acid, and showed that the ceramide profile and barrier properties of their in-house collagen-based full-thickness HSEs can be improved. Another major limitation of the HSEs is the lack of appendages such as hair follicles, pilosebaceous units and sweat glands. HSEs with appendages are yet to be developed. This is important as the use of nanoparticles has been intensively investigated for topically and transdermal treating several of dermatological diseases[1] and studies have suggested that the delivery of drugs from nanoparticles occurs through the deposition in hair follicles.[27-29] Thus the incorporation of appendages in HSE models could further improve these models and add the follicular transport pathway to the HSEs.

Table 2.2 Comparison of drug permeation on commercial HSEs to human skin and pig skin.

Commercial HSEs	Company	Model drug	Compared with human skin	Compared with pig skin	Ref
RHEs					
EpiDerm™	MatTek Corp (Ashland, USA)	Flufenamic acid	Flux is five times higher		6
SkinEthic™	Episkin (Lyon, France)	Terbinafine	~ 24 fold higher in flux	~37 fold higher in flux	5
		Clotrimazole	~ 900 fold higher in flux	~ 900 fold higher in flux	
		Hydrocortisone	~ 200 fold higher in flux	~ 500 fold higher in flux	
		Salicylic acid	~ 6 fold higher in flux	~15 fold higher in flux	
Episkin	Episkin (Lyon, France)	Testosterone	~100 times higher in permeation coefficient		30
		Caffeine	~10 times higher in permeation coefficient		
Full-thickness					
Graftskin™ LSE™	Organogenesis (MA, USA)	Terbinafine	~ 24 fold higher in flux	~ 25 fold higher in flux	5
		Clotrimazole	~1000 fold higher in flux	~ 1000 fold higher in flux	
		Hydrocortisone	~200 fold higher in flux	~ 400 fold higher in flux	
		Salicylic acid	~ 2 fold higher in flux	~ 3.5 fold higher in flux	
Phenion® FT	Henkel (Düsseldorf, Germany)	Testosterone		~20 fold higher in permeation coefficient	13
		Caffeine		~200 fold higher in permeation coefficient	

2.4.2. Tools for identifying corrosivity and irritation

HSEs models allow topical application of chemical compounds and provide a more physiologically relevant platform for irritancy testing. There are several commercially available epidermal equivalents that are used for testing the irritancy potential of chemicals. Of these, three models (Episkin, Epiderm™ and SkinEthic) mentioned in OECD test guideline 439 are accepted by the EU and the FDA for skin irritation testing and measure cell viability of the epidermis[1] (Table 2.3). Less validated approaches of predicting the irritation potential of chemicals include measuring the cytokine secretion of IL-1α, IL-6, and IL-8 from the epidermal equivalent models[31].

Although reconstructed epidermal equivalents are more commonly utilized for *in-vitro* irritation screening, full thickness skin equivalents may provide a more accurate prediction and mechanistic insights due to the presence of the dermis. The inclusion of fibroblasts in the skin equivalent model may be important since the fibroblasts and keratinocytes may act synergistically during the *in-vivo* irritation response to produce secondary cytokines and chemokines such as IL-6, GM-CSF, CXCL12, CCL2 and CCL5[32]. Several full thickness skin equivalents that are commercially available include TestSkin®, Apligraf®, AST-2000®, and Skin2®. These skin models have been evaluated for their potential in predicting skin irritation by assessing the cell viability/cytotoxicity and the secretion of inflammatory soluble factors such as IL-1, IL-8, IL-6, and PGE_2 after exposure to potential irritants[31] (Table 2.3). However, currently no full thickness skin equivalent model has yet been accepted by the EU or the FDA for skin irritation prediction.

Although the use of the MTT assay on epidermal equivalents is accepted by the EU and the FDA as a suitable alternative to the *in-vivo* Draize albino rabbit test, there are still issues to be solved. These issues include batch-to-batch variation, higher cost, and a *stratum corneum* barrier that is more permeable than that of *in-vivo* human skin. Furthermore, sweating is not accounted for with current *in-vitro* assays since skin equivalent models lack sweat glands. Thus, current methods cannot predict irritation responses that may occur due to the presence of sweat[33].

Table 2.3 Summary of RHEs and full-thickness skin equivalent models for *in-vitro* irritation testing.

Reconstructed Human Epidermis	**Model Characteristics**	**Metrics**	**Ref**
Epiderm™	keratinocytes on permeable culture inserts	Cellular viability (MTT)	34
SkinEthic	keratinocytes on polycarbonate filter	Cellular viability (MTT)	34
Episkin	keratinocytes on type I collagen coated matrix with type IV collagen	Cellular viability (MTT)	34
Full-Thickness Skin Equivalents	**Model Characteristics**	**Metrics**	**Ref**
TestSkin ®	keratinocytes on fibroblasts-populated dermis with type I collagen	Secretion of prostaglandins (PGE2)	31
Apligraf ®	keratinocytes on fibroblasts-populated dermis with type I collagen	Cytokine secretion (IL-1α, IL-8)	31
Skin-2 ®	keratinocytes on fibroblasts - populated dermis on nylon mesh	Cellular Pathways (JNK1/2, p38, ERK1/2, STAT1, PLCγ)	31
AST2000 ®	keratinocytes on fibroblasts - populated dermis	Cellular viability (MTT)	31

2.4.3. Tools for identifying sensitization

Although the leading *in-vitro* assays for assessing skin sensitization all utilize submerged cell cultures, the use of skin equivalents can offer several advantages. The presence of a *stratum corneum* allows for topical application of the test treatment and allows permeation into the skin. Using a full-thickness skin equivalent also preserves key cellular interactions and synergies between keratinocytes and fibroblasts that occur during sensitization. Furthermore, the mRNA expression levels for metabolic enzymes such as members of the Cytochrome P450 family in full thickness skin equivalents were found to be more comparable to that of *in-vivo* human skin than epidermal equivalents and cells in submerged cultures[35].

There are several commercially available skin equivalents that are composed of keratinocytes on top of a fibroblast-populated bovine collagen type 1 matrix. However, only the EST-1000 epidermal model and AST-2000 full-thickness model from Cell Systems (St. Katharinen, Germany) have been evaluated for the purpose of screening skin sensitizers[36] (Table 2.4). Test sensitizers oxazolone, 1-fluoro-2,4-dinitrobenzene (DNFB) and irritants SDS and TritonX-100 were topically applied to the EST-1000 and AST-2000 and cell signaling pathways (JNK1/2, p38, ERK1/2, STAT1, PLCγ) that transduce immune responses and regulate cytokines were investigated. JNK1/2 and p38 were activated by phosphorylation exclusively with sensitizer treated conditions and ERK1/2 was only activated by irritant conditions. Since dendritic cells are a key cellular player during acute contact dermatitis, a full-thickness skin model with the inclusion of Mutz-3 derived dendritic cells (Mutz-DCs) was developed[37]. When topically challenged with sensitizers nickel sulfate and resorcinol, the Mutz-DCs migrated out of the epidermis and

into the dermis and expressed a co-stimulatory molecule CD83. Thus, the migration of the Mutz-DCs and CD83 expression in response to sensitizers indicates maturation of sensitized dendritic cells. Although this skin equivalent is promising with some of the essential cellular players present within one skin equivalent, there is limited data on this skin model and additional validation is still necessary.

Table 2.4 Summary of HSEs-based *in-vitro* alternatives for sensitization testing.

Model	Model Characteristics	Metrics	Ref
EST-1000	Epidermal equivalent	Cellular Pathways (JNK1/2, p38, ERK1/2, STAT1, PLCγ)	[36]
AST-2000	Full-thickness equivalent	Cellular Pathways (JNK1/2, p38, ERK1/2, STAT1, PLCγ)	[36]
Skin model with Mutz-DCs	Full thickness equivalent with integrated Mutz-DCs	Histology to assess Mutz-DCs migration, surface expression (CD83)	[37]

Mutz-DCS= Mutz-3 derived dendritic cells.

2.5. Conclusion

RHEs and full-thickness HSEs are reconstructed skin tissues that are intended to mimic the composition and functions of native skin. In the pharmaceutical industry, these tissues have the potential of being used as pre-clinical models to aid in the selection of lead compounds, provide safety and efficacy data that are more predictive and relevant to conventional cell culture methods. Continuous research in this field is undergoing, the use of conventional natural polymers and advanced biomaterials (e.g., decellularized tissue, biodegradable polymers) can provide new opportunities for the construction of functional HSEs for various drugs screening purposes.[38, 39] Ultimately, HSEs with ideal barrier properties, less variation in permeability data, and relevant *in-vitro*/*in-vivo* correlations will be very useful pre-clinical models to assist in the selection and development of topically applied drugs.

2.6. References

1. Zhang, Z., Tsai, P.C., Ramezanli, T., and Michniak-Kohn, B.B. Polymeric nanoparticles-based topical delivery systems for the treatment of dermatological diseases. Wiley Interdiscip Rev Nanomed Nanobiotechnol 5, 205, 2013.
2. Koster, M.I. Making an epidermis. Ann N Y Acad Sci 1170, 7, 2009.
3. Kanerva, L., Elsner, P., Wahlberg, J.E., and Maibach, H.I. Handbook of Occupational Dermatology. New York: Springer- Verlag Berlin Heidelberg; 2013.
4. Schafer-Korting, M., Bock, U., Diembeck, W., Dusing, H.J., Gamer, A., Haltner-Ukomadu, E., Hoffmann, C., Kaca, M., Kamp, H., Kersen, S., Kietzmann, M., Korting, H.C., Krachter, H.U., Lehr, C.M., Liebsch, M., Mehling, A., Muller-Goymann, C., Netzlaff, F., Niedorf, F., Rubbelke, M.K., Schafer, U., Schmidt, E., Schreiber, S., Spielmann, H., Vuia, A., and Weimer, M. The use of reconstructed human epidermis for skin absorption testing: Results of the validation study. Altern Lab Anim 36, 161, 2008.
5. Schmook, F.P., Meingassner, J.G., and Billich, A. Comparison of human skin or epidermis models with human and animal skin in *in-vitro* percutaneous absorption. Int J Pharm 215, 51, 2001.
6. Zghoul, N., Fuchs, R., Lehr, C.M., and Schaefer, U.F. Reconstructed skin equivalents for assessing percutaneous drug absorption from pharmaceutical formulations. ALTEX 18, 103, 2001.
7. Laubach, V., Zoller, N., Rossberg, M., Gorg, K., Kippenberger, S., Bereiter-Hahn, J., Kaufmann, R., and Bernd, A. Integration of Langerhans-like cells into a human skin equivalent. Arch Dermatol Res 303, 135, 2011.
8. Tjabringa, G., Bergers, M., van Rens, D., de Boer, R., Lamme, E., and Schalkwijk, J. Development and validation of human psoriatic skin equivalents. Am J Pathol 173, 815, 2008.
9. Li, L., Fukunaga-Kalabis, M., and Herlyn, M. The three-dimensional human skin reconstruct model: a tool to study normal skin and melanoma progression. J Vis Exp 2011.
10. Hogk, I., Rupp, S., and Burger-Kentischer, A. 3D-tissue model for herpes simplex virus-1 infections. Methods Mol Biol 1064, 239, 2013.
11. Duval, C., Chagnoleau, C., Pouradier, F., Sextius, P., Condom, E., and Bernerd, F. Human skin model containing melanocytes: essential role of keratinocyte growth factor for constitutive pigmentation-functional response to alpha-melanocyte stimulating hormone and forskolin. Tissue Eng Part C Methods 18, 947, 2012.
12. Egles, C., Garlick, J.A., and Shamis, Y. Three-dimensional human tissue models of wounded skin. Methods Mol Biol 585, 345, 2010.
13. Ackermann, K., Borgia, S.L., Korting, H.C., Mewes, K.R., and Schafer-Korting, M. The Phenion full-thickness skin model for percutaneous absorption testing. Skin Pharmacol and Physiol 23, 105, 2010.
14. Blais, M., Mottier, L., Germain, M.A., Bellenfant, S., Cadau, S., and Berthod, F. Sensory neurons accelerate skin reepithelialization via substance P in an innervated tissue-engineered wound healing model. Tissue Eng Part A 20, 2180, 2014.
15. Ojeh, N.O., Frame, J.D., and Navsaria, H.A. In vitro characterization of an artificial dermal scaffold. Tissue Eng 7, 457, 2001.
16. Badylak, S.F., Taylor, D., and Uygun, K. Whole-organ tissue engineering: decellularization and recellularization of three-dimensional matrix scaffolds. Annu Rev Biomed Eng 13, 27, 2011.
17. Nayak, S., Dey, S., and Kundu, S.C. Skin equivalent tissue-engineered construct: co-cultured fibroblasts/ keratinocytes on 3D matrices of sericin hope cocoons. PLoS One 8, e74779, 2013.
18. Liu, X., Ma, L., Liang, J., Zhang, B., Teng, J., and Gao, C. RNAi functionalized collagen-chitosan/silicone membrane bilayer dermal equivalent for full-thickness skin regeneration with inhibited scarring. Biomaterials 34, 2038, 2013.
19. Wang, H.M., Chou, Y.T., Wen, Z.H., Wang, C.Z., Chen, C.H., and Ho, M.L. Novel biodegradable porous scaffold applied to skin regeneration. PLoS One 8, e56330, 2013.

20. Shahabeddin, L., Berthod, F., Damour, O., and Collombel, C. Characterization of skin reconstructed on a chitosan-cross-linked collagen-glycosaminoglycan matrix. Skin Pharmacol 3, 107, 1990.
21. De Vuyst, E., Charlier, C., Giltaire, S., De Glas, V., de Rouvroit, C.L., and Poumay, Y. Reconstruction of normal and pathological human epidermis on polycarbonate filter. Methods Mol Biol 1195, 191, 2014.
22. Tu, C., Cai, Q., Yang, J., Wan, Y., Bei, J., and Wang, S. The fabrication and characterization of poly(lactic acid) scaffolds for tissue engineering by improved solid-liquid phase separation. Polymers for Advanced Tech 14, 565, 2003.
23. Kumbar, S.G., Nukavarapu, S.P., James, R., Nair, L.S., and Laurencin, C.T. Electrospun poly(lactic acid-co-glycolic acid) scaffolds for skin tissue engineering. Biomaterials 29, 4100, 2008.
24. Cui, W., Zhu, X., Yang, Y., Li, X., and Jin, Y. Evaluation of electrospun fibrous scaffolds of poly(DL-lactide) and poly(ethylene glycol) for skin tissue engineering. Mater Sci Eng C 29, 1869, 2009.
25. Thakoersing, V.S., van Smeden, J., Mulder, A.A., Vreeken, R.J., El Ghalbzouri, A., and Bouwstra, J.A. Increased presence of monounsaturated fatty acids in the stratum corneum of human skin equivalents. J Invest Dermatol 133, 59, 2013.
26. Ghosh, B., Reddy, L.H., Kulkarni, R.V., and Khanam, J. Comparison of skin permeability of drugs in mice and human cadaver skin. Indian J Exp Biol 38, 42, 2000.
27. Shim, J., Seok Kang, H., Park, W.S., Han, S.H., Kim, J., and Chang, I.S. Transdermal delivery of mixnoxidil with block copolymer nanoparticles. J Control Release 97, 477, 2004.
28. Lademann, J., Richter, H., Teichmann, A., Otberg, N., Blume-Peytavi, U., Luengo, J., Weiss, B., Schaefer, U.F., Lehr, C.M., Wepf, R., and Sterry, W. Nanoparticles--an efficient carrier for drug delivery into the hair follicles. Eur J Pharm Biopharm 66, 159, 2007.
29. Otberg, N., Patzelt, A., Rasulev, U., Hagemeister, T., Linscheid, M., Sinkgraven, R., Sterry, W., and Lademann, J. The role of hair follicles in the percutaneous absorption of caffeine. Br J Clin Pharmacol 65, 488, 2008.
30. Netzlaff, F., Kaca, M., Bock, U., Haltner-Ukomadu, E., Meiers, P., Lehr, C.M., and Schaefer, U.F. Permeability of the reconstructed human epidermis model Episkin in comparison to various human skin preparations. Eur J Pharm Biopharm 66, 127, 2007.
31. Gibbs, S. In vitro irritation models and immune reactions. Skin Pharmacol Physiol 22, 103, 2009.
32. Corsini, E., and Galli, C.L. Cytokines and irritant contact dermatitis. Toxicol Lett 102-103, 277, 1998.
33. Matsumura, H., Oka, K., Umekage, K., Akita, H., Kawai, J., Kitazawa, Y., Suda, S., Tsubota, K., Ninomiya, Y., Hirai, H., and et al. Effect of occlusion on human skin. Contact Dermatitis 33, 231, 1995.
34. OECD. Guidelines for the Testing of Chemicals (TG428). *In-vivo* skin irritation:reconstructed human epidermis test method. 2013.
35. Luu-The, V., Duche, D., Ferraris, C., Meunier, J.R., Leclaire, J., and Labrie, F. Expression profiles of phases 1 and 2 metabolizing enzymes in human skin and the reconstructed skin models Episkin and full thickness model from Episkin. J Steroid Biochem Mol Biol 116, 178, 2009.
36. Koeper, L.M., Schulz, A., Ahr, H.J., and Vohr, H.W. In vitro differentiation of skin sensitizers by cell signaling pathways. Toxicology 242, 144, 2007.
37. Ouwehand, K., Spiekstra, S.W., Waaijman, T., Scheper, R.J., de Gruijl, T.D., and Gibbs, S. Technical advance: Langerhans cells derived from a human cell line in a full-thickness skin equivalent undergo allergen-induced maturation and migration. J Leukoc Biol 90, 1027, 2011.
38. Tsai, P.C., Zhang, Z., Michniak Kohn, B.B., and Florek, C. Constructing Human Skin Equivalents on Porcine Acellular Peritoneum Extracellular Matrix for In Vitro Irritation Testing. Tissue Eng Part A 2015.

39. Lee, W., Debasitis, J.C., Lee, V.K., Lee, J.H., Fischer, K., Edminster, K., Park, J.K., and Yoo, S.S. Multi-layered culture of human skin fibroblasts and keratinocytes through three-dimensional freeform fabrication. Biomaterials 30, 1587, 2009.

3. Chapter 3. Optimization of decellularized ECM-based HSEs

3.1. Introduction

Decellularized extracellular matrix (dECM) has been extensively studied to produce highly biomimetic scaffolds that can be utilized in tissue regeneration to treat injuries from various organs (e.g, bone, skin, liver).[1-3] The high biocompatible, low immunogenic and high biomimetic properties allow it to achieve faster healing time, lower wound formation and avoid rejection during grafting. For example, decelluarized human dermal tissue has been used for abdominal wall reconstruction and wound healing.[4] It has shown to decrease wound contraction significantly compared to epithelial grafts in mice and porcine animal model. In another example, the treatment of full-thickness wounds by mesenchymal stem cells seeded-decellularized bovine small intestinal submucosa (SIS) in rodents showed less scarring and exhibited more mature stage of skin appendages formation compared to the non-treated group.[5]

Besides clinical wound healing and organ regeneration applications, decellularized tissues are also widely used as *in-vitro* models for basic research. For example, tissue-derived and cell-derived decellularized ECM was used as *in-vitro* model to study the cell-matrix interactions for stem cell differentiation.[6] Decellularized ECM preserved the critical proteins and structures and could be used to elucidate the comprehensive roles of ECM and its interactions with cells.

In native tissue, ECM is composed of collagens, glycoproteins, proteoglycans, and glycosaminoglycans and the protein components of the ECM vary within different organs. Decellularized ECM, generated from native tissue/organs has its cellular components removed by decellularization treatments. These treatments include

combinations of physical (e.g., agitation, sonication, freeze-thaw), chemical (alkali, acids, organic, detergents) and enzymatic (e.g., protease, nuclease) procedures. Appropriate decellularization process is critical to generate composition, structure and mechanical properties that are similar to native ECM.

The dermal substitutes for HSEs are usually from animal-sourced (e.g., bovine, rat) collagen gel based on the high biocompatibility and the ability to physically encapsulate dermal fibroblasts. However, the collagen gel is relatively simple and less similar to the native ECM compared to decellularized ECM. Decellularized ECM seems to be a more suitable scaffold for constructing HSEs based on the higher complexity and better mimicking of native tissue. Therefore the use of decellularized material to generate *in-vitro* skin tissue engineering provides a promising technique to be used in the production of HSEs.

The optimization of HSEs requires the investigation of cell-cell interactions, cell-matrix interaction and environmental niche. The formatting a mature epidermis relies on a delicate balance between keratinocyte proliferation and differentiation. The homeostasis of epidermal tissue is a complex network that is affected by the communications between keratinocytes and dermal fibroblasts. In organotypic culture of HSEs, the epidermal regeneration is highly affected by fibroblasts and surrounding microenvironment.[7] In this study, critical cell-cell interactions and cell-matrix interactions was studied to optimize epithelial layer of decellularized ECM based HSEs.

3.2. Materials and Methods

3.2.1. Cell culture

Neonatal human dermal fibroblasts (HDF) and neonatal human keratinocytes were purchased from Life Technologies, NY. Spontaneously transformed immortal human keratinocytes (HaCaT) was a gift from Dr. Joachim Kohn (New Jersey Center for Biomaterials). Murine fibroblasts NIH3T3 cells were obtained from ATCC. Dulbecco's Modified Eagle Medium (DMEM), fetal bovine serum (FBS), penicillin, streptomycin, Epilife® media, human keratinocyte growth supplement, phosphate buffer pH 7.4, trypsin neutralizer solution, 0.025% and 0.25% trypsin-ethylenediamine tetraacetic acid (EDTA) were all purchased from Life Technologies. Tissue culture treated T25, T75 flasks and polycarbonate, polyester Transwell inserts were obtained from Corning Inc, NY.

Mono-culturing HDF: Cryopreserved HDF (passage one) with total cell number > $1x10^6$ were obtained from Life Technologies. HDF were cultured with DMEM media containing 10% (v/v) FBS and 100 units/mL penicillin, 100 μg/mL streptomycin and 0.25 μg/mL amphotericin B. Cell culture media was changed every other day and the cells were grown in an incubator (Steri-Cult™, ThermoFisher) at 37°C/5% CO_2. For subculture, the cells were treated with 0.025% trypsin-EDTA under room temperature 3-5 minutes and inhibit trypsin activity by adding FBS contained DMEM culture media and followed by centrifugation (1000 rpm/6 minutes). The remaining pellet was redispersed using DMEM culture media. Passage of not more than five was used in all experiments. The cells were cryopreserved with DMEM culture media with 5% dimethyl sulfoxide (DMSO) and stored in a liquid nitrogen tank.

Mono-culturing HaCaT: HaCaT was cultured with DMEM media containing 10% (v/v) FBS and 100 units/mL penicillin, 100 μg/mL streptomycin and 0.25 μg/mL amphotericin B. Cell culture media were changed every other day. Once the cells reached 80% confluency, the cells were trypsinized with 0.25% trypsin under 37 °C for 5-10 minutes. The trypsin activity was further inhibited by the addition of FBS contained DMEM and followed by centrifugation (1000 rpm/6 minutes). The cell pellets were redispersed in culture media and grown at 37 °C in an incubator with 95% humidity and 5% CO_2.

Mono-culturing primary keratinocytes: Cryopreserved neonatal human keratinocytes (HEKn) (passage one) with cells >$5x10^5$/vial were initiated by seeding cells at a density of 2.5 x $10^3/cm^2$. The cells were grown with Epilife® media containing 0.2% (v/v) bovine pituitary extract, 5 μg/mL insulin, 0.18 μg/mL hydrocortisone, 5 μg/mL bovine transferrin, 0.2 ng/mL epidermal growth factor, 100 units/mL penicillin, 100 μg/mL streptomycin and 0.25 μg/mL amphotericin B. The medium was changed every other day and the cells were split when they reach 80% confluent. To subculture neonatal human keratinocytes, the cells were treated with 0.025% trypsin/0.01% ETDA at room temperature for 5-10 minutes and monitored under a light microscope to see the detachment. When the cells detached from the flasks, trypsin neutralizer solution (0.0125% purified soybean trypsin inhibitor in PBS) was added and the cell suspension was centrifuged at 1000 rpm for 6 minutes. The cell pellets were then redispersed in keratinocyte growth factor containing Epilife® media and seeded into flasks at cell density of 2.5 x $10^3/cm^2$.

Mono-culturing NIH3T3: Murine fibroblasts NIH3T3 were cultured with DMEM media containing 10% (v/v) FBS and 100 units/mL penicillin, 100 μg/mL streptomycin and 0.25 μg/mL amphotericin B. In 1975, Rheinwald and Green develop a technique for growing keratinocytes. These keratinocytes were seeded at clonal densities in present of a feeder layer of random bred Swiss 3T3 cells.[8] The fibroblasts secreted extracellular matrix protein and growth factors that supported attachment and proliferation of keratinocytes. In order to use as feeder layer for culturing primary keratinocytes, NIH3T3 cells were further treated with mitomycin C (Fisher Scientific). Mitomycin C is a potent DNA cross-linker, naturally produced by *Streptomyces caespitosus*. Mitomycin C inhibits DNA synthesis (Figure 3.1) and nuclear division of NIH3T3 and therefore reduces over-proliferation of the fibroblasts in the later co-culture environment.[9] Confluent NIH3T3 cells grown in T75 flasks were added with 200 μL of 500 μg/mL mitomycin C and incubated at 37°C for 2 hours. The flasks were further washed with PBS three times and the cells were collected by trypsinization using 0.025% trypsin-EDTA and neutralized by trypsin neutralizer.

Co-culturing HEKn with NIH3T3: Primary keratinocytes, HEKn were mixed with mitomycin C-treated NIH3T3 cells at a 1:5 ratio. Culture media was prepared by mixing Epilife® culture media with FBS free DMEM media at 2:1 (v/v) ratio. Prior to confluence, the HEKn were passaged by the addition of 0.02% EDTA to the culture flask for 5 minutes at 37°C and followed by gentle aspiration with a pipette. This allowed the selectively detachment of mitomycin C treated NIH3T3 feeder layer. The HEKn were then detached by adding 0.025% tryspin-EDTA to the flask and incubated about 10 minutes under 37°C. The cell suspensions were then mixed with trypsin neutralizer and

centrifuged to inactivate the trypsin activity. The cells were then replaced in a T75 flask containing mitomycin C treated NIH3T3.

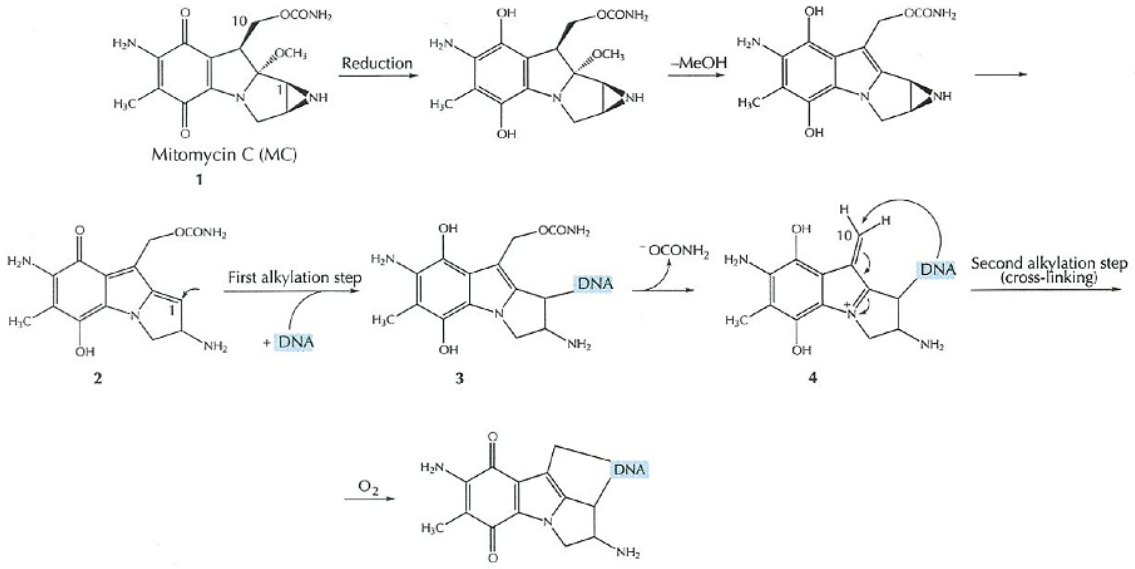

Figure 3.1 The reductive activation cascade of mitomycin C and the covalent cross-linking the strands of DNA duplex.[9]

3.2.2. Optimization of HSEs based on keratinocyte cell type

HDF (1.5 $x10^{4-}5x10^{4}$ /cm^2) were seeded on MesoPP side (type 1 collagen rich surface) of acellular peritoneum matrix (APM, DSM biomedical). The next day, primary neonatal human keratinocytes ($2.5x10^4$/cm^2), neonatal human keratinocytes cultured with NIH3T3 feeder layer ($2.5x10^4$/cm^2) or HaCaT ($5x10^4$ /cm^2) were seeded on MesoBM (basement membrane rich surface) side of APM. The HSEs constructs were further cultured under submerged media for the first two weeks and transferred to air-liquid (A/L) interface at the third and fourth weeks. Samples were fixed with 10% buffered formalin and examined using histology analysis.

3.2.3. Optimization of HSEs based on seeding positions

The effects of cell seeding positions on the APM were investigated. Three different seeding schemes were prepared: (1) Human keratinocytes, HaCaT on MesoBM and HDF on MesoPP, (2) HaCaT on top of HDF and both on MesoBM (3) HaCaT on top of MesoBM and HDF seeded at outer well (Figure 3.2). The impact of different cell-matrix interaction to epithelial development was examined by H&E staining, cross sectional images and the topography was inspected using scanning electron microscopy.

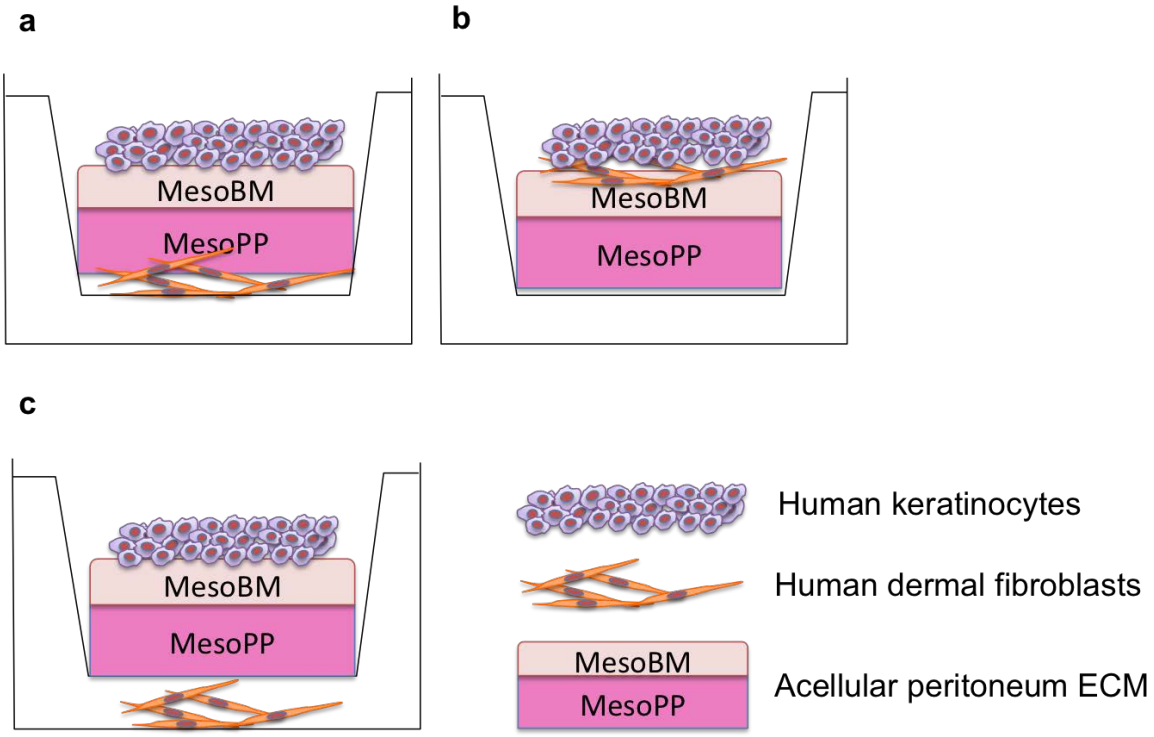

Figure 3.2 Schematic of different cell seeding position during *in-vitro* culture. Human keratinocytes, HaCaT on MesoBM and HDF on MesoPP (a); HaCaT on top of HDF and on MesoBM (b); HaCaT on top of MesoBM and HDF seeded at outer well (c).

3.2.4. Optimization of HSEs based on culture media

Culture media with and without transforming growth factor alpha (TGF-α) was compared to see the effect of culture media composition. For the control media group, the HSEs samples were cultured with DMEM with 10% FBS for one week under submerged conditions, then cultured with differential media. This included a 3:1 (v/v) of DMEM: EpiLife® with bovine pituitary extracts (Life Technologies) with final concentration of 25 μM palmitic acid (Sigma Aldrich), 15 μM linoleic acid (Sigma Aldrich), 25 μM oleic acid (Sigma Aldrich), 7 μM arachidonic acid (Sigma Aldrich), 100 μg/mL ascorbic acid (Sigma Aldrich), 10 μM carnitine (Spectrum), 300 μM clofibrate (Sigma Aldrich), 100 μM bovine serum albumin (Sigma Aldrich), and 2 mM calcium chloride (Sigma Aldrich) and with A/L interface for another two weeks. For the TGF-α group, the HSEs samples were cultured with DMEM, 10% FBS, and TGF-α 2 ng/mL for one week under submerged conditions. The following two weeks were at A/L interface with the same composition of control differentiation media and with addition of TGF-α 2 ng/mL. The samples were fixed at week three with formalin buffer and processed, cross-sectioned and H&E stained.

3.2.5. Optimization of HSEs based on seeding methods

Static pipette method and syringe-filter method was compared by seeding HDF on acellular porcine decellularized matrix (APM). For pipette seeding, APM with MesoPP side facing up was placed in a 24 well plate and fixed with a rubber O-ring. The APM was hydrated with culture media before adding $1x10^4$ HDF in 50 μL DMEM culture media. After incubation in 37°C for 3 hours, 1 mL of DMEM cell culture media was added. For syringe-filter seeding, the APM membrane was sandwiched between silicone

O-rings in a 13 mm diameter filter holder (Swinnex, Millipore). 5 mL of DMEM cell culture media was added to the syringe-filter to wet the APM. Then $1x10^4$ HDF in 5 mL DMEM cell culture media was pushed through the syringe. The HDF seeded APM were then transferred to a 24 well plate at 37°C for 3 hours which was filled with 1 mL of DMEM cell culture media. The cell viability was analyzed at 1, 4, and 7 days post-seeding using AlamarBlue® assay according to the protocol provided by Life Technologies, NY. All samples were n=3.

3.2.6. Analysis of HSEs lipids

Analysis of HSEs lipids was from a method that was previously published.[23] HSEs with $5x10^4$ HDF (seeded on MesoPP side) and $5x10^4$ HaCaT seeded on MesoBM side) were cultured for 3 weeks. After the maturation of HSEs, the epidermal lipid content of constructed HSEs and cadaver human skin were determined by thin layer chromatography. Briefly, the samples were lyophilized and the total lipids were extracted by a serial of chloroform/methanol mixture (2:1, 1:1, 1:2 v/v) at 2-hour intervals. Combined extracts were than dried under nitrogen and redissolved in 100 μL of chloroform/methanol solution (2:1 v/v). The dissolved lipid mixture was separated using a 20x 20 cm glass plate coated with silica gel (Adsorbosil-plus-1; Alltech Associates, IL). The plate were washed with chloroform/methanol solution (2:1 v/v) and activated in a 110 °C oven. Samples were applied 2-3 cm from the bottom of the plate and the chromatograms were air dried, sprayed with 50% sulfuric acid, heated at 220°C and scanned with a photodensitometer.

3.2.7. Evaluation of HSEs barrier properties by electrical resistance

The transcutaneous electrical resistance (TER) of the skin is the measure of the degree of difficulty of passing an electric current through skin tissue. The unit for resistance is expressed in ohms, Ω. The resistance (R), is defined as the ratio of voltage (V) over current (I):

$$R=\frac{V}{I}$$

Matured three weeks APM-HSEs ($5x10^4$ HaCaT and $5x10^4$ HDF) and split-thickness cadaver human posterior torso skin (NY Firefighters, New York NY) were cut and transferred to 0.4 μm polyester Transwell® 12 mm inserts (Corning, Costar, NY) on a polystyrene plate. Dulbecco's Modified Eagle Medium (DMEM) culture media with 10% v/v fetal bovine serum (Thermo Fisher Scientific) was added to the inner and outer compartments. Electrical resistances of the samples were measured by an electric meter (Kelin Tools, MM1000, IL) (Figure 3.3). The negative charge electrode was in contact with donor solution while the positive charge electrode was in the receptor solution. Six replicas per group were performed. Each sample was measured five times and the results were reported as mean $k\Omega/cm^2$ ± standard deviation.

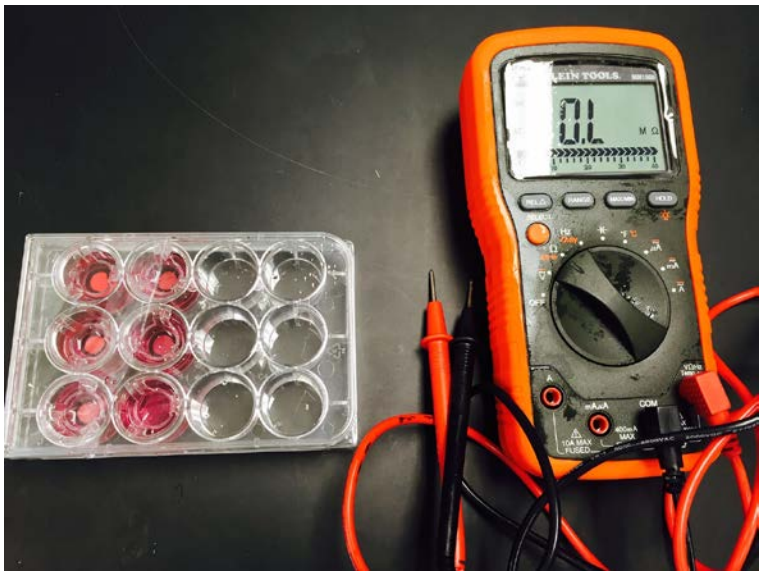

Figure 3.3 Electrical resistance of cultured HSEs measured with an electric meter (Kelin Tools, MM1000, IL).

3.3. Results

3.3.1. Effect of keratinocyte cell type on epidermis development

Primary neonatal primary keratinocytes (HEKn) and spontaneously transformed immortal human keratinocytes (HaCaT) have been widely used in dermatological research. HSEs based on these different types of keratinocytes and in combination with neonatal human dermal fibroblasts were cultured on acellular peritoneal extracellular matrix (APM). The development of epithelial layers on the HSEs was analyzed by examination of cross-sections (embedded in paraffin and sliced with 8 μm thick) and H&E staining.

3.3.1.1. HSEs with HDF and HEKn

HSEs constructed by co-seeding HDF on MesoPP and HEKn on MesoBM and were cultured for three weeks. Histological images at weeks 1, 2, and 3 are shown in

Figure 3.4. The thicknesses of the epidermal layers gradually increased over time and formed approximately 50-80 μm thick at week 3. The epidermal layers on the HSEs were fully stratified and formed a *stratum corneum.* However, the HSEs lacked other epidermal layers such as *stratum basale*, *stratum spinosum* and *stratum granulosum.*

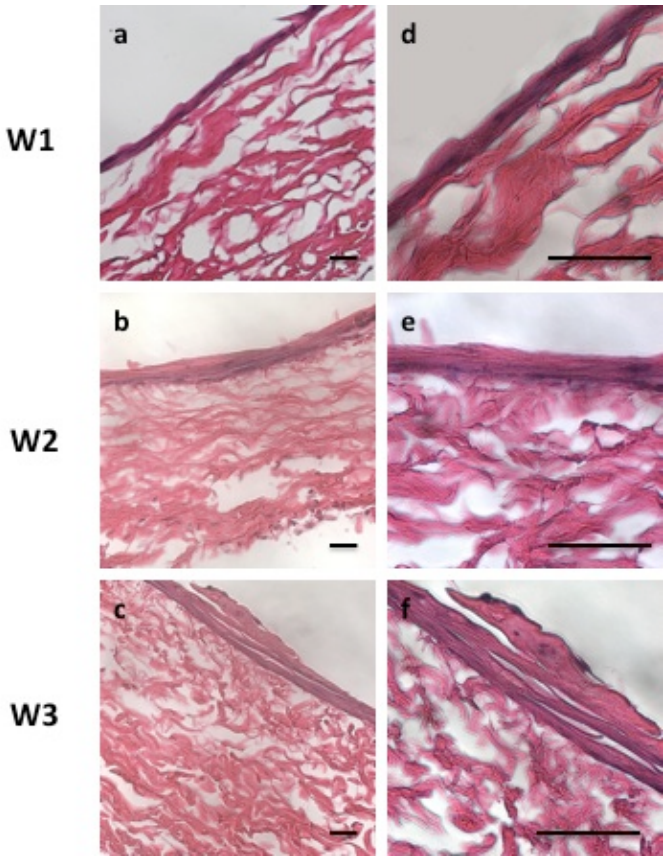

Figure 3.4 Epithelial architecture of organotypic cultured HSEs with HDF and HEKn. Cross-sectional images of APM-HSEs (HDF+HEKn) at week one (W1; a,d), week two (W2; b,e) and week three (W3; c,f). Samples were stained with H&E. Images at magnification of 200x (a,b,c) and 400x (d,e,f) were taken. Scale bar indicates 100 μm.

3.3.1.2. HSEs based on HDF and NIH3T3 co-cultured HEKn

The *in-vitro* serial culture of primary keratinocytes alone is known to be difficult. In 1975, Rheinwald and Green were the first to introduce two-dimensional (2D) feeder-layer co-culture of keratinocytes with postmitotic 3T3 cells.[8] There is a strong

dependence of keratinocytes with mesenchymal interactions, where the diffusible factors provided by the fibroblasts support the proliferation of keratinocytes *in-vitro*.[10]

Figure 3.5 shows differential interference contrast images of mono-cultured HEKn and the comparison of those using mitomycin C treated NIH3T3 as a feeder layer to culture HEKn. The co-culturing HEKn with postmitotic NIH3T3 resulted in promoting HEKn proliferation in colonies on 2D tissue culture flasks (Figure 3.5 b and d).

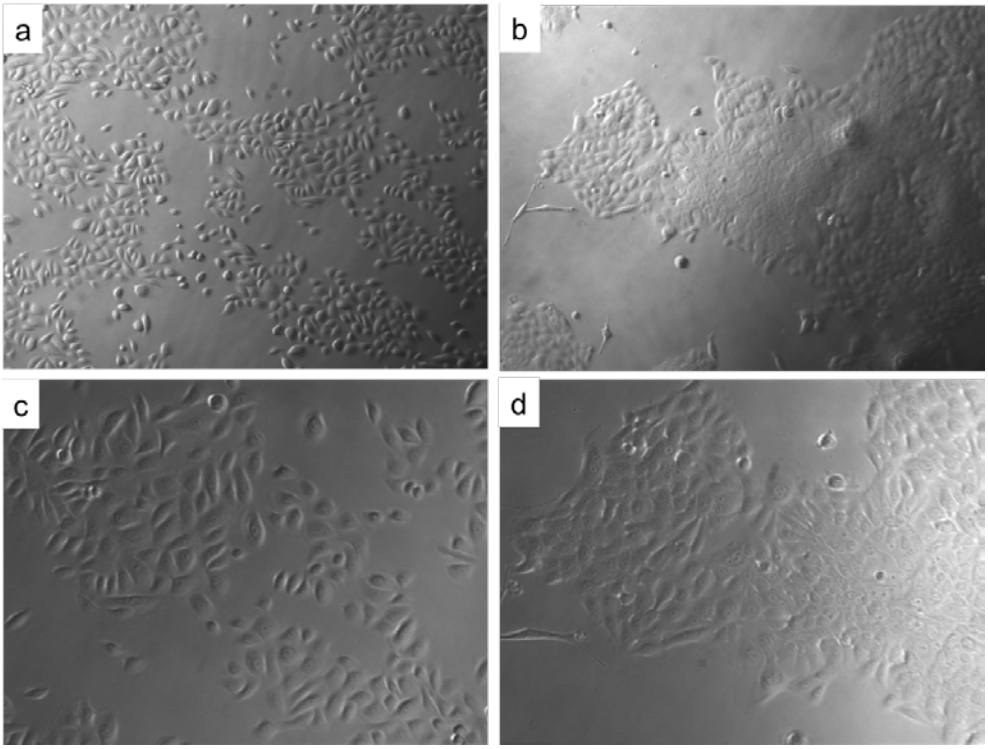

Figure 3.5 Differential interference contrast images of mono-cultured HEKn (a, c) and co-culture of mitomycin C treated NIH3T3 with HEKn (b, d). Images were taken at 100X magnification (a, b) and 200X magnification (c, d).

The HEKn that were co-cultured with postmitotic NIH3T3 were then harvested and seeded ($2.5x10^4/cm^2$) on to HDF populated APM ($5x10^4/cm^2$). Figure 3.6 shows epithelial architecture of APM-HSEs at weeks one, two, three and four. The epidermis thickness gradually increased to around 200 μm at week four. Moreover, the epidermal

thicknesses of postmitotic NIH3T3/HEKn cultured APM-HSEs (Figure 3.6) were found to be thicker than those of using mono-cultured HEKn (Figure 3.4). However, despite the formation of a fully stratified *stratum corneum* layer, the APM-HSEs again lacked *stratum basale*, *stratum spinosum* and *stratum granulosum.*

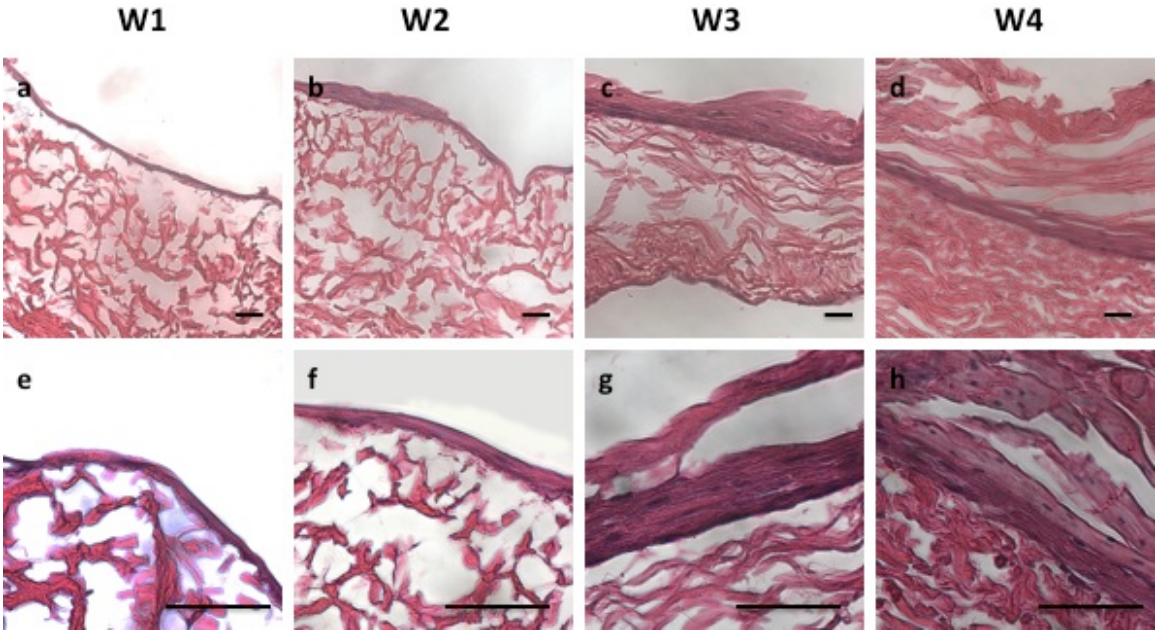

Figure 3.6 Cross-sectional images of APM-HSEs cultured with HDF (on MesoPP side) and postmitotic NIH3T3 cultured HEKn (on MesoBM side). Cross-section images of APM-HSEs and week one (W1;a,e), week two (W2; b,f), week three (W3;c,g) and week four (W4, d,h). Samples were stained with H&E. Scale bar indicates 100 µm.

3.3.1.3. HSEs based on HDF and HaCaT

Spontaneously transformed immortal human keratinocytes, HaCaT are an aneuploid immortal human keratinocyte cell line from adult human skin.[11] They are a clonogenic transformed phenotype *in-vitro* and non-tumorigenic. The HaCaT cells reform an orderly and differentiated epithelial structure when transplanted onto nude mice.

The cellular growth of HaCaT and HDF on APM was first studied by seeding HaCaT-Lag and HDF-Lar on two sides of the APM and control groups were bovine type

1 collagen gel and tissue culture polystyrene (TCPS). HaCaT-Lag and HDF-Lar were LifeAct lentiviral vector transduced cells that express green fluorescent protein (GFP) and red fluorescent protein (RFP) respectively on actin filaments. Figure 3.7 indicates fluorescent images of mono-cultured HaCaT-Lag and HDF-Lar on MesoBM, MesoPP sides of acellular porcine extracellular matrix, collagen gel and TCPS. HaCaT-Lag showed increased GFP expression with the order of MesoPP>MesoBM>TCPS> collagen gel on day 7. The RFP expression of HDF-Lar was similar from day one to day seven. Overall, the fluorescent images indicate the cells were attaching and remained viable on the MesoBM and MesoPP for seven days. This result suggested the excellent compatibility of HaCaT-Lag and HDF-Lar on APM.

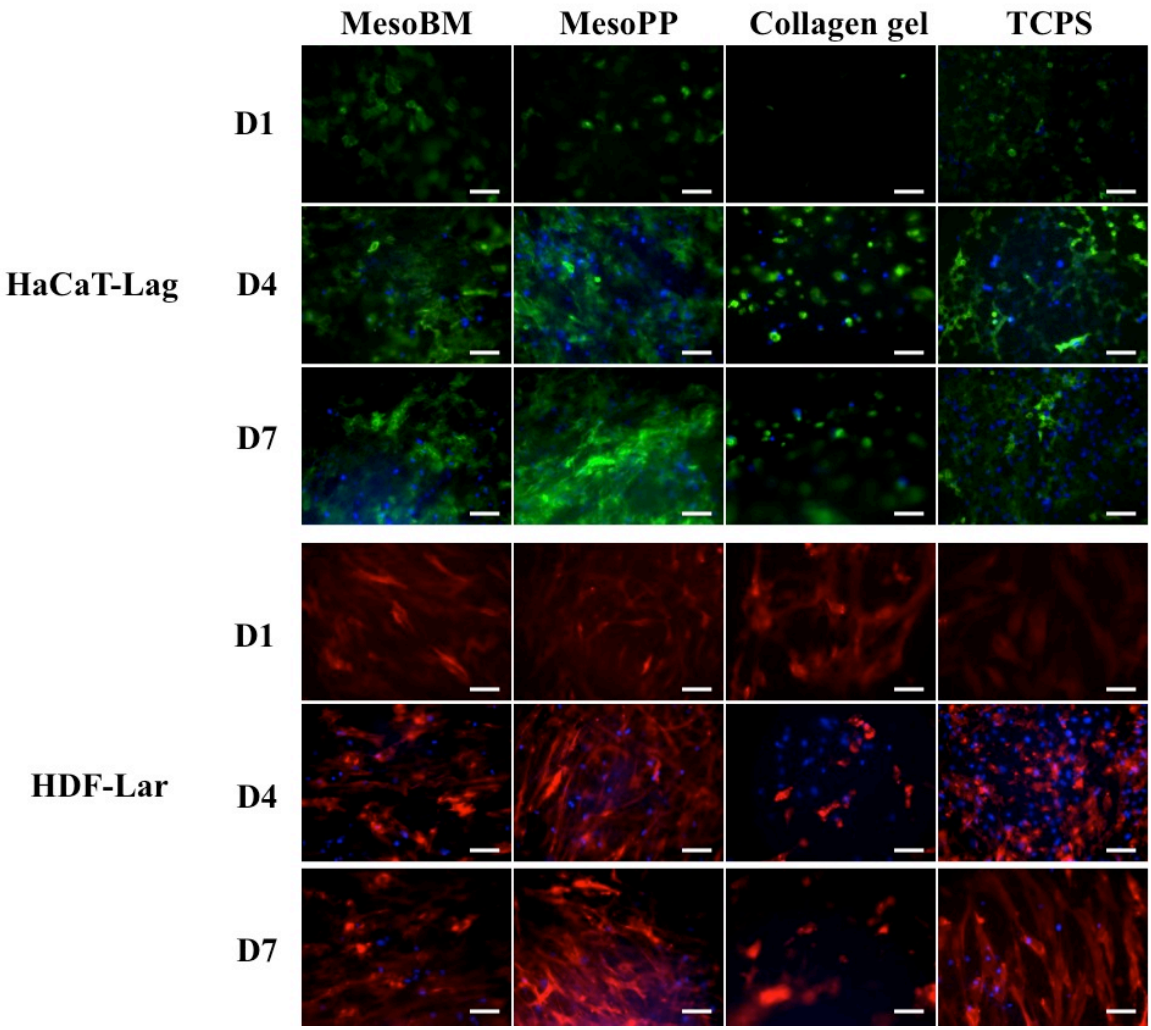

Figure 3.7 Fluorescent images of mono-cultured HaCaT-Lag (express green color) and HDF-Lar (express in red color) on each sides of acellular porcine extracellular matrix (i.e., MesoBM, MesoPP), and those of type I collagen hydrogel and tissue culture polystyrene (TCPS) at day 1, day 4 and 7 (D1, D4, D7, respectively). D4 and D7 images were counterstained with Hoechst nuclei dye (express in blue color). Scale bar indicates 100 μm.

3.3.2. Effect of cell seeding position

Various combinations of fibroblasts and keratinocytes seeding positions were investigated in order to optimize epithelial development of the HSEs. HSEs with co-cultured HDF/HaCaT were used as the model. The epithelial development of three different cell seeding of APM-HSEs: (1) HDF on MesoPP with HaCaT on MesoBM

(Figure 3.8 a,d); both HDF and HaCaT seeded on BM side (Figure 3.8 b,e), and HDF at outer well and HaCaT on MesoBM (Figure 3.8 c,f) were evaluated. The seeding of (1) HaCaT on MesoBM with HDF on MesoPP and (2) both on MesoBM groups provide a better combination for epidermal layer formation. However, the HDF that were seeded on the outer well showed the least formation of an epidermis. This result indicated that the HDF produced critical paracrine effects to support the growth of the HaCaT.

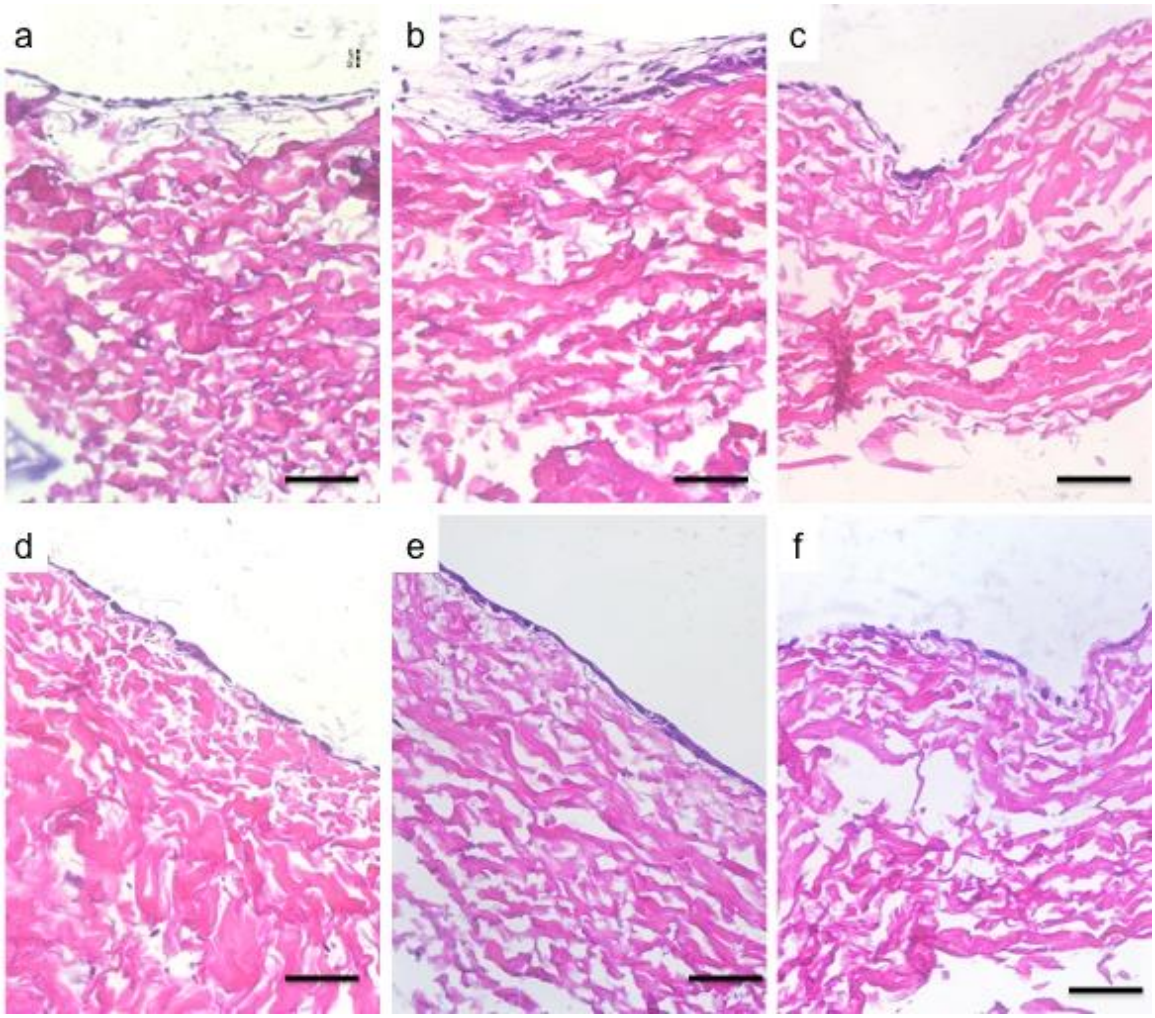

Figure 3.8 Histological analysis of the effect of different seeding positions on epithelial development. APM-HSEs of HDF on MesoPP with HaCaT on MesoBM (a,d); both HDF and HaCaT seeded on BM side (b,e), and HDF at outer well and HaCaT on MesoBM (c,f). Cell seeding density at 1.5 x10^4 HDF and 2.5 x 10^4 HaCaT are shown in a,b and c. Cell seeding density at 3 x10^4 HDF and 2.5 x 10^4 HaCaT are shown in d,e, and f. APM-HSEs were cultured for two weeks. Scale bar indicates 100 μm.

In a second study, epithelial topography of 3 week cultured HSEs with different HDF-Lar /HaCaT-Lag cell seeding positions were analyzed by SEM (Figure 3.9). All three positions: (1) $2.5x10^4$ HaCaT-Lag on MesoBM, (2) $2.5x\ 10^4$ HaCaT-Lag overlaying $5x10^4$ HDF-Lar on MesoBM, and (3) $2.5x10^4$ HaCaT-Lag overlaying $5x10^4$ HDF-Lar on MesoPP exhibited squamous corneocyte-like structures.

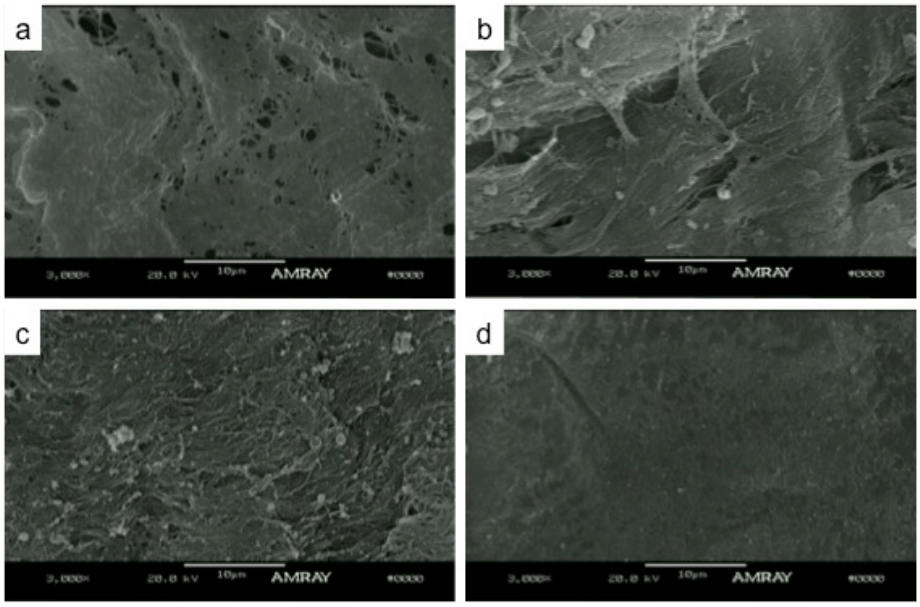

Figure 3.9 Scanning electron microscopy of HSEs epithelial topography based on different cell seeding position. Blank MeosBM (a), $2.5x10^4$ HaCaT-Lag on MesoBM (b), $2.5x\ 10^4$ HaCaT-Lag overlaying $5x10^4$ HDF-Lar on MesoBM (c), and $2.5x10^4$ HaCaT-Lag overlaying $5x10^4$ HDF-Lar on MesoPP (d). Images were taken at week three of culture.

3.3.3. Effect of cell culture composition on epithelial development

Normal epidermal development is not often obtained easily during *in-vitro* culture conditions. Optimizing media composition of *in-vitro* culturing environment is the most simple and direct way to affect the epithelial development of HSEs. Many studies have investigated the effect of small molecules such as calcium[12], vitamins[13, 14] and lipid

supplements on *stratum corneum* architecture and lipid barrier profiles. In addition, protein macromolecules such as epidermal growth factor (EGF), fibroblast growth factors (FGF), and insulin-like growth factor-I (IGF-I) were shown to support the expansion of keratinocytes *in-vitro*.[15] Our preliminary data demonstrated the effect of transforming growth factor alpha (TGF-α) on HaCaT proliferation and differentiation on different matrix based HSEs (Figure 3.10). HDF and HaCaT were co-cultured on three different dermal substrates (i.e., APM, decellularized porcine dermis, bovine type 1 collagen gel). The HSEs were submerged and cultured with DMEM cell culture media for one week and then another two weeks at the A/L interface with either a control lipid differentiation media or the addition of 2 ng/mL TGF-α to the lipid media. For the epithelial development: the epidermal layer on MesoBM, cultured from control media showed flat nuclei, whereas the TGF-α media exhibited nuclei with a round shape (Figure 3.10 a,d). The round shape phenotype of HaCaT was more closely associated with the phenotype from basal layer of human epidermis. The epidermal layer of decellularized porcine dermis, cultured from control media showed rounder shaped nuclei compared to the TGF-α media. The epidermal layer of the TGF-α media cultured group had no nuclei presented (Figure 3.10 b,e).

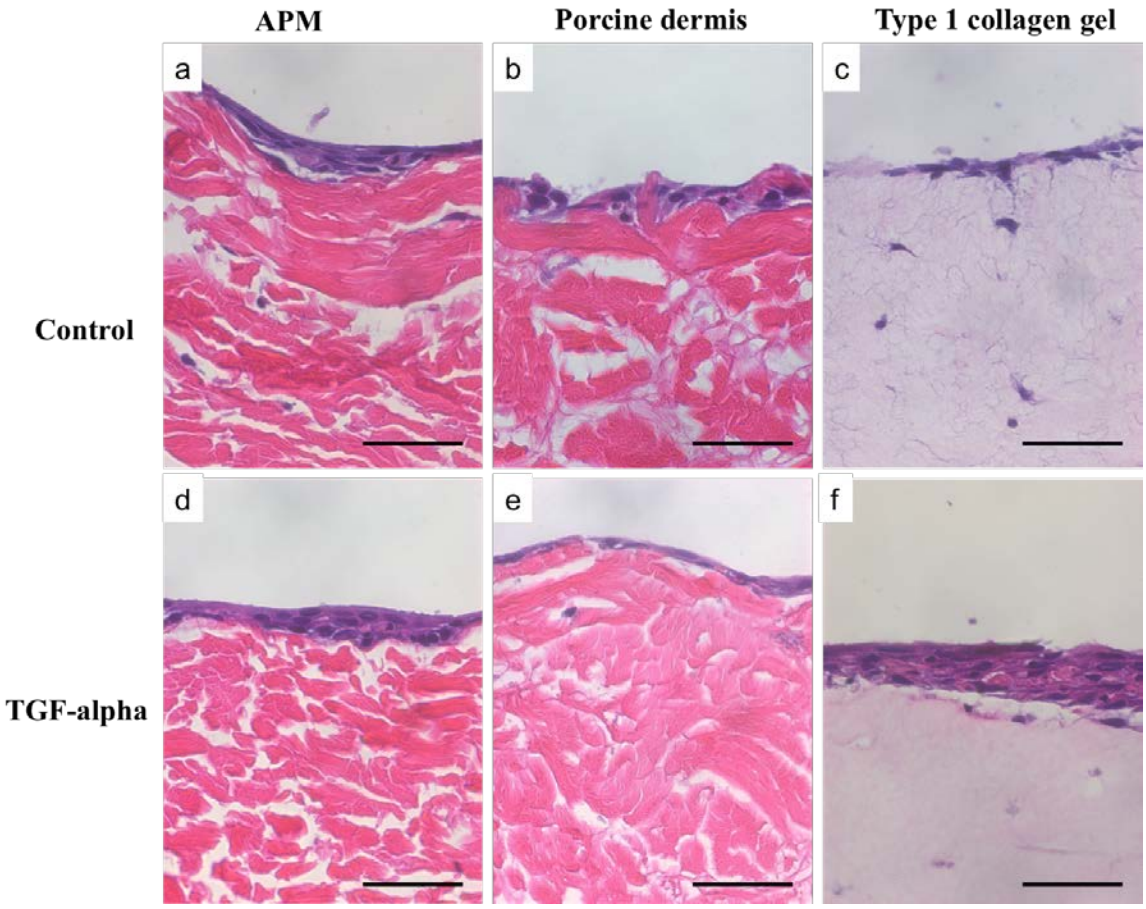

Figure 3.10 Effect of culture media on HSEs epidermal development. HSEs constructed from acellular peritoneum extracellular matrix (APM; MesoBM side) (a), decellularized porcine dermis (b), and type 1 collagen gel (c) cultured with control media. HSEs constructed from APM (MesoBM side) (d), decellularized porcine dermis (e), and type 1 collagen gel (f) cultured with TGF-alpha supplemented media. Scale bar indicates 50 μm.

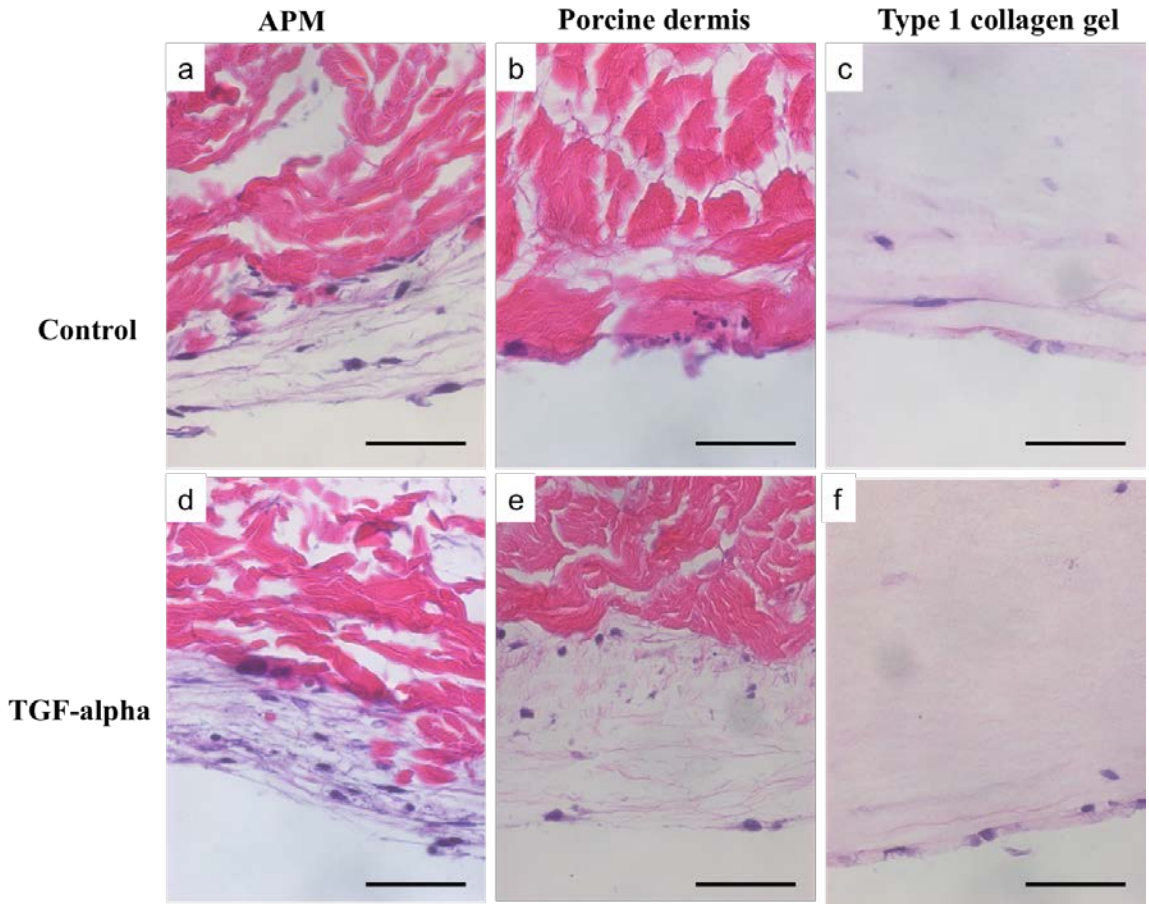

Figure 3.11 Effect of culture media on HSEs fibroblast layer development. HSEs constructed from APM (MesoPP) (a), decellularized porcine dermis (b), and type 1 collagen gel (c) cultured with control media. HSEs constructed from APM (MesoPP) (d), decellularized porcine dermis (e), and type 1 collagen gel (f) cultured with TGF-alpha supplemented media. Scale bar indicates 50 μm.

For the fibroblast layers, multiple layers of fibroblasts were formed on the MesoPP side of APM. The fibroblasts from the TGF-α media treated group formed a slightly denser and stacked layers compared to the control group (Figure 3.11,d). For the porcine dermal HSEs, the fibroblasts layer exhibited increased proliferation compared to the control media group (Figure 3.11,e). However, no significant differences were recorded for the fibroblasts layers and no morphological changes were found with type 1 collagen gel (Figure 3.11, f). Maas-Szabowski et al. reported that the regeneration of

epidermis and normalized stromal interaction of HaCaT is initiated by TGF-α.[16] HaCaT express essential epidermal differentiation markers but are known to have deficiencies in tissue organization. One of the major reasons is the expression and release of autocrine TGF-α that dramatically decreases in HaCaT. Therefore, by supplementing TGF-α in the culture media, one can normalize the differentiation of the HaCaT.

3.3.4. Effect of cell seeding method

Different seeding methods may result in different spreading of cells on the decellularized matrix. Seeding HDF with simple pipette or modified syringe-filter techniques on acellular porcine decellularized matrix was compared. The syringe-filter method showed slightly higher cellular viability compared to the pipette method at day 7 (Figure 3.12). Ideally, the requirements for optimum seeding require minimal cell damage, high uniformity of cell spreading, high seeding efficiency and minimal seeding time. The pipette seeding is a static method, where the cell suspension is dripped onto the matrix surface which allows the cells to settle by gravity and migrate into the scaffold over time. The advantage of the pipette seeding method is the simplicity of the procedure and low mechanical damage. However, the disadvantage is the potential of low homogenous of cell distribution. The syringe-filter method is modified from syringe sterile filtering technique, where the cell suspensions were first drawn up with a syringe. APM scaffolds were mounted in a polypropylene filter holder. The syringe that contained cell suspensions was then attached to the scaffold-mounted filter holder with female Luer lock and the cell suspension was pushed from the plunger. This resulted in the collection of the cells on the scaffold with the media eluted. The advantage of the syringe-filter method is it is a relative active and simple seeding procedure that requires an external

force.[17] In our preliminary data, the syringe-filter method showed slightly higher cell viability than pipette method on day 1 and day 7 (Figure 3.12). Additional experiments such as characterizing penetration depth and uniformity of cells based on syringe-filter seeding method will be helpful for selecting a suitable seeding method.

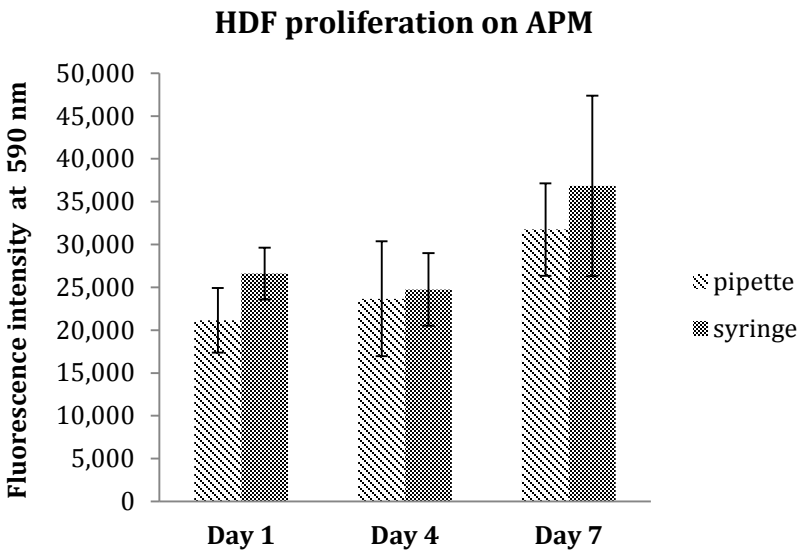

Figure 3.12 Effect of HDF proliferation at days 1, 4, and 7 from pipette or syringe seeding method. Mean fluorescence intensity ± standard deviation is shown. N=3.

3.3.5. HSEs lipid composition

Lipid composition in skin provides critical barrier properties of *stratum corneum*. The *stratum corneum* contains about 40% protein, 40% water and 18-20% of lipids and forms the major barrier in skin for the transport of actives. The lipid composition in human *stratum corneum* is reported to be 10% cholesterol esters, 7.32% triglycerides, 16.12% free fatty acids, 16.43% cholesterol, 40.26% sphingolipids and 3.76% cholesterol sulfate.[18]

The lipid composition of three week cultured APM-HSEs ($5x10^4$ HDF; $5x10^4$ HaCaT) was characterized by thin layer chromatography. The content of phospholipid, cholesterol, total fatty acids and ceramides were compared with cadaver human skin (Table 3.1). APM-HSEs exhibited lower content of phospholipids (93.5 ± 1.9 % dry mass) and cholesterol (6.95 ± 1.9 %) compared with cadaver human skin. In addition, fatty acids and ceramides of HSEs were low under the detection limit. The lipid composition and organization of HSEs play important roles in providing accurate barrier property for skin, thus they are important parameter for the HSEs that are utilized as *in-vitro* drug permeation screening models.

Table 3.1 Lipid compositions of HSEs and cadaver human skin. Values are reported as % dry mass.

Lipid	HSEs	Cadaver human skin
Phospholipids	93.5 ± 1.9	50.9
Cholesterol	6.95 ± 1.9	23.3
Fatty acids	not detected	4.1
Ceramides	not detected	19

3.3.6. Transcutaneous Electrical Resistance (TER) of APM-HSEs

Measuring the transcutaneous electrical resistance (TER) is a way to characterize barrier properties of the APM-HSEs and mammalian skin. According to OECD Test No.430, TER of rat skin can be used to identify the level of corrosiveness of a substance *in-vitro*. Corrosive substances reduced *stratum corneum* integrity and therefore result in reductions of TER bellow the 5kΩ threshold level of rat skin.[19] Three week matured APM-HSEs ($5x10^4$ HaCaT and $5x10^4$ HDF) and split-thickness cadaver human posterior torso skin were cut and transferred to 0.4 μm polyester Transwell® 12 mm inserts on

polystyrene with Dulbecco's Modified Eagle Medium (DMEM) culture media with 10% v/v fetal bovine serum. Electrical resistances of the samples were measured by an electric meter and the data are shown in Table 3.2. The blank Transwell® polyester membrane, blank APM, APM-HSEs and human skin had TER of 22.5 ± 2.3, 28.1± 6.3, 43.8 ± 6.1, and 89.6 ± 10.5 kΩ/cm^2 respectively. The TER of APM-HSEs was slightly lower than human skin, which may be explained by the lower lipid composition of APM-HSEs.

Table 3.2 Transcutaneous electrical resistance of APM, APM-HSEs and cadaver human skin. N=6. Electrical resistance expressed as mean ± standard deviation.

Sample	**Electrical Resistance kΩ/cm^2**
Transwell® polyester membrane	22.5 ± 2.3
Blank acellular porcine ECM (APM)	28.1± 6.3
APM-HSEs	43.8 ± 6.1
Cadaver human skin	89.6 ± 10.5

3.4. Discussion

Decellularized ECM offers a microenvironment that is similar to *in-vivo* conditions. The use of dECM is not only useful for wound healing applications, but also in basic skin research and has potential use in drug development.[20] Basic skin research includes cell-matrix interactions and potential application in drug development includes the use of dECM to construct HSEs for *in-vitro* drug permeability and transport testing.

In order to establish tools for *in-vitro* screening, the development of HSEs requires optimization in many aspects of the organotypic culturing process.[21] The optimization of HSEs involves studying the effect of specific cell types, seeding methods (e.g., static v.s. dynamic), cell seeding positions, cell seeding density, and culture media composition. From our study, we learned that different keratinocyte cell types such as

HEKn, HEKn cultured with mitomycin C treated NIH3T3, and immortalized human keratinocytes (HaCaT) resulted in HSEs with various epithelial morphologies. HEKn resulted in fully stratified epithelium and the HEKn cultured with mitomycin C treated NIH3T3 exhibited thicker *stratum corneum* compared to HEKn alone. However, both of these cell methods resulted in HSE lack of a basal layer. Furthermore, in our study, static and dynamic seeding methods were compared. Seeding methods included simple static pipette seeding or syringe seeding. The syringe seeding method resulted in a slightly higher cell viability of HDF on APM on day 7. This is similar to the findings reported by from Xiao et al. that dynamic seeding followed by static cultivation ensures the efficient use of fibroblasts and greatly improves neodermis formation on porous scaffolds.[22]

Selection of the culture media is one of the most critical parameters in HSE optimization. Based on the complexity of cell type and the nature of keratinocyte homeostatsis, it is essential to provide an environment that is suitable for the cells to grow and differentiate. Our preliminary data showed the effect of adding growth factor TGF-alpha to the media during tissue culture. The structure and thickness of the epithelial layer from HaCaT/HDF based HSEs was improved by the additional of TGF-alpha to the culture media. This could be explained by the reduced expression of TGF-alpha in HaCaT compared to HEKn and by supplementing TGF-alpha, the interactions of HaCaT with stromal cells were being normalized.[16]

In addition to analyzing the biochemical composition of HSEs such as lipid composition and examining the histology of epithelial structure, the function of skin such as the ability to provide barrier properties was evaluated by measuring electrical resistance. Establishing the correct skin barrier is critical for HSEs especially it is planned

to utilize them for assisting *in-vitro* drug permeation profile. The barrier property is mostly contributed from the intact *stratum corneum* layer. However, obtaining a *stratum corneum* in HSEs that has identical barrier properties to that of *in-vivo* human skin have yet to be achieved. Most of the commercially available HSEs still tend to be more permeable than native human skin.

3.5. Conclusions

In summary, our studies produced a tissue engineered skin model with decellularized ECM substrate that is potentially promising. The optimization of the culturing protocol and process was essential for the HSEs to possess similar tissue structure and function that was comparable to those of *in-vivo* skin. With such advanced and more promising HSE models, it may be possible to further optimize them to be predictive biological membranes for the use of *in-vitro* drug screening for topical and transdermal products.

3.6. References

1. Cunniffe, G.M., Vinardell, T., Murphy, J.M., Thompson, E.M., Matsiko, A., O'Brien, F.J., and Kelly, D.J. Porous decellularized tissue engineered hypertrophic cartilage as a scaffold for large bone defect healing. Acta Biomater 23, 82, 2015.
2. Su, Z., Ma, H., Wu, Z., Zeng, H., Li, Z., Wang, Y., Liu, G., Xu, B., Lin, Y., Zhang, P., and Wei, X. Enhancement of skin wound healing with decellularized scaffolds loaded with hyaluronic acid and epidermal growth factor. Mater Sci Eng C Mater Biol Appl 44, 440, 2014.
3. Barakat, O., Abbasi, S., Rodriguez, G., Rios, J., Wood, R.P., Ozaki, C., Holley, L.S., and Gauthier, P.K. Use of decellularized porcine liver for engineering humanized liver organ. J Surg Res 173, e11, 2012.
4. Bondioli, E., Fini, M., Veronesi, F., Giavaresi, G., Tschon, M., Cenacchi, G., Cerasoli, S., Giardino, R., and Melandri, D. Development and evaluation of a decellularized membrane from human dermis. J Tissue Eng Regen Med 8, 325, 2014.
5. Parmaksiz, M., Elcin, A.E., and Elcin, Y.M. Decellularization of bovine small intestinal submucosa and its use for the healing of a critical-sized full-thickness skin defect, alone and in combination with stem cells, in a small rodent model. J Tissue Eng Regen Med 2015.
6. Hoshiba, T., Chen, G., Endo, C., Maruyama, H., Wakui, M., Memoto, E., Kawazoe, N., and Tanaka, M. Decellularized Extracellular Matrix as an In Vitro Model to study the comprehensive roles of the ECM in Stem Cell Differentiation. Stem Cells Int 20162015.
7. Boehnke, K., Mirancea, N., Pavesio, A., Fusenig, N.E., Boukamp, P., and Stark, H.J. Effects of fibroblasts and microenvironment on epidermal regeneration and tissue function in long-term skin equivalents. Eur J Cell Biol 86, 731, 2007.
8. Rheinwald, J.G., and Green, H. Serial cultivation of strains of human epidermal keratinocytes: the formation of keratinizing colonies from single cells. Cell 6, 331, 1975.
9. Tomasz, M. Mitomycin C: small, fast and deadly (but very selective). Chem Biol 2, 575, 1995.
10. El Ghalbzouri, A., Lamme, E., and Ponec, M. Crucial role of fibroblasts in regulating epidermal morphogenesis. Cell Tissue Res 310, 189, 2002.
11. Boukamp, P., Petrussevska, R.T., Breitkreutz, D., Hornung, J., Markham, A., and Fusenig, N.E. Normal keratinization in a spontaneously immortalized aneuploid human keratinocyte cell line. J Cell Biol 106, 761, 1988.
12. Vicanova, J., Boelsma, E., Mommaas, A.M., Kempenaar, J.A., Forslind, B., Pallon, J., Egelrud, T., Koerten, H.K., and Ponec, M. Normalization of epidermal calcium distribution profile in reconstructed human epidermis is related to improvement of terminal differentiation and stratum corneum barrier formation. J Invest Dermatol 111, 97, 1998.
13. Savini, I., Catani, M.V., Rossi, A., Duranti, G., Melino, G., and Avigliano, L. Characterization of keratinocyte differentiation induced by ascorbic acid: protein kinase C involvement and vitamin C homeostasis. J Invest Dermatol 118, 372, 2002.
14. Sorensen, S., Solvsten, H., Politi, Y., and Kragballe, K. Effects of vitamin D3 on keratinocyte proliferation and differentiation in vitro: modulation by ligands for retinoic acid and retinoid X receptors. Skin Pharmacol 10, 144, 1997.
15. Mujaj, S., Manton, K., Upton, Z., and Richards, S. Serum-free primary human fibroblast and keratinocyte coculture. Tissue Eng Part A 16, 1407, 2010.
16. Maas-Szabowski, N., Starker, A., and Fusenig, N.E. Epidermal tissue regeneration and stromal interaction in HaCaT cells is initiated by TGF-alpha. J Cell Sci 116, 2937, 2003.
17. Tan, L., Ren, Y., and Kuijer, R. A 1-min method for homogenous cell seeding in porous scaffolds. J Biomater Appl 26, 877, 2012.
18. Lee, S.J., Kim, D.W., Jun, J.B., Chung, S.L., and Kim, J.C. Lipid composition of the stratum corneum of the sole in patients with leprosy. Int J Lepr Other Mycobact Dis 62, 574, 1994.
19. OECD. Test No. 430: In Vitro Skin Corrosion: Transcutaneous Electrical Resistance Test Method (TER). 2013.

20. Zhang, Z., and Michniak-Kohn, B.B. Tissue engineered human skin equivalents. Pharmaceutics 4, 26, 2012.
21. Black, A.F., Bouez, C., Perrier, E., Schlotmann, K., Chapuis, F., and Damour, O. Optimization and characterization of an engineered human skin equivalent. Tissue Eng 11, 723, 2005.
22. Xiao, Y.L., Riesle, J., and Van Blitterswijk, C.A. Static and dynamic fibroblast seeding and cultivation in porous PEO/PBT scaffolds. J Mater Sci Mater Med 10, 773, 1999.
23. Batheja, P., Song , Y., Wertz, P., and Michniak-Kohn, B.B. Effects of Growth Conditions on the Barrier of a Human Skin Equivalent. Pharm Rearch 26, 1689, 2009.

4. Chapter 4. *In-vitro* irritation testing based on APM-HSEs

4.1. Introduction

Safety and irritation testing is crucial during the development of topically applied drugs and cosmetic formulations. Traditional screening for skin irritation involves the *in-vivo* Draize skin test on albino rabbits and patch test on human volunteers.[1, 2] These assays are based on scoring erythema and edema reactions after the application of formulations on skin. However, the use of these *in-vivo* models is often associated with problems such as high costs, subjective scoring, questionable reproducibility, ethical concerns, and limited availability.[3-5] The European Union (EU) has banned the sales of any cosmetic ingredients and products that have been tested on animals (EU Regulation 1223/2009) as of 2009, and completely banned animal testing for cosmetic products as of 2013. The U.S. Food and Drug Administration (FDA) also advocates the refinement, reduction and replacement of animal tests within the limits of scientific ability. Alternative *in-vitro* testing methods have been developed to replace animal studies, including quantitative structure-activity relationship (QSAR), computational approaches, monolayer cell cultures, and three-dimensional (3D) skin models.[6, 7] Among the above approaches, 3D human skin equivalents (HSEs) models are promising for *in-vitro* testing, based on the potential to reflect cell differentiation, polarization, and cell-matrix interactions of skin. Therefore, HSEs have been used to determine drug irritation[8,9], corrosivity[10], permeation[11, 12], and genotoxicity[13] of topically applied formulations.

HSEs can be classified into three major categories: (a) epidermal models, (b) dermal models, and (c) full-thickness skin models. The epidermal models contain multiple layers (i.e., *stratum corneum, stratum granular, stratum spinosum, stratum*

basale) of primary human keratinocytes or immortalized cell lines (e.g., HaCaT[14], NIKS[15]) on a thin supporting porous membrane such as polycarbonate and cellulose acetate filters.[16, 17] The dermal models feature fibroblasts embedded in extracellular matrix (ECM) such as type I collagen hydrogel, hyaluronic acid or on the surface of de-epidermized dermis (DED).[18, 19] The full-thickness models have stratified keratinocytes over fibroblasts-populated matrices.[20] Recent literature focuses on two major advances in full-thickness models: (1) higher complexity models that incorporate multiple cell types such as addition of dendritic cells, melanocytes, endothelial cells and stem cells have been reported[21-25]; (2) Decellularized tissues (such as allodermis[26]) that can be used for constructing full-thickness HSEs models. Decellularized tissues are extensively studied in skin grafting applications based on the fact that they retain high similarity in composition and structure to native ECM and could support the proliferation and differentiation of skin cells *in-vivo*.[27,28] Despite the advance in various HSEs models, there were little efforts in validating full-thickness models for *in-vitro* irritation screening. Currently, only four reconstructed human epidermis models (Episkin™, EpiDerm™, SkinEthic™, LabCyte EPI-MODEL) have been adopted by Organisation for Economic Co-operation and Development (OECD) to provide alternative *in-vitro* methods for classifying irritated chemicals.[29] All of these models are epidermis models that are based on keratinocyte cells and do not contain other cell populations in dermis layer, e.g., fibroblasts. Full-thickness HSEs that contain both keratinocytes and fibroblasts may better predict the irritation response since their physiology is more relevant to native skin than that for epidermal models.

The aim of this study is to construct full-thickness HSEs on porcine acellular peritoneum matrix (APM) and investigate the function of APM-HSEs as *in-vitro* irritation screening tool. The peritoneum lines the abdominal cavity and has a basement membrane supporting a uniform layer of mesothelial cells. The APM was produced by DSM Biomedical's proprietary OPTRIX™ decellularization process, which removed cellular components while maintaining ECM composition (i.e., collagen I, collagen IV, laminin, fibronectin) and growth factors (i.e., VEGF, FGF, TGF-β).[30] Due to the nature of the peritoneum, the APM is a polar scaffold with a compact basement membrane side (abbreviated as the MesoBM side) and an opposing side with open fibrous architecture that faced the pre-peritoneal space (abbreviated as the MesoPP side) (Figure 4.1.). The cellular response of human skin cells on the two sides of the APM was investigated. The structure of the constructed APM-HSEs was characterized by histology and immunohistochemistry analyses. Then, the function of the APM-HSEs was studied to assess whether they can predict irritancy ranking for several selected chemicals. To the best of our knowledge, this is the first time that an APM has been used to construct a 3D full-thickness skin model and for such model to be tested for *in-vitro* skin irritation.

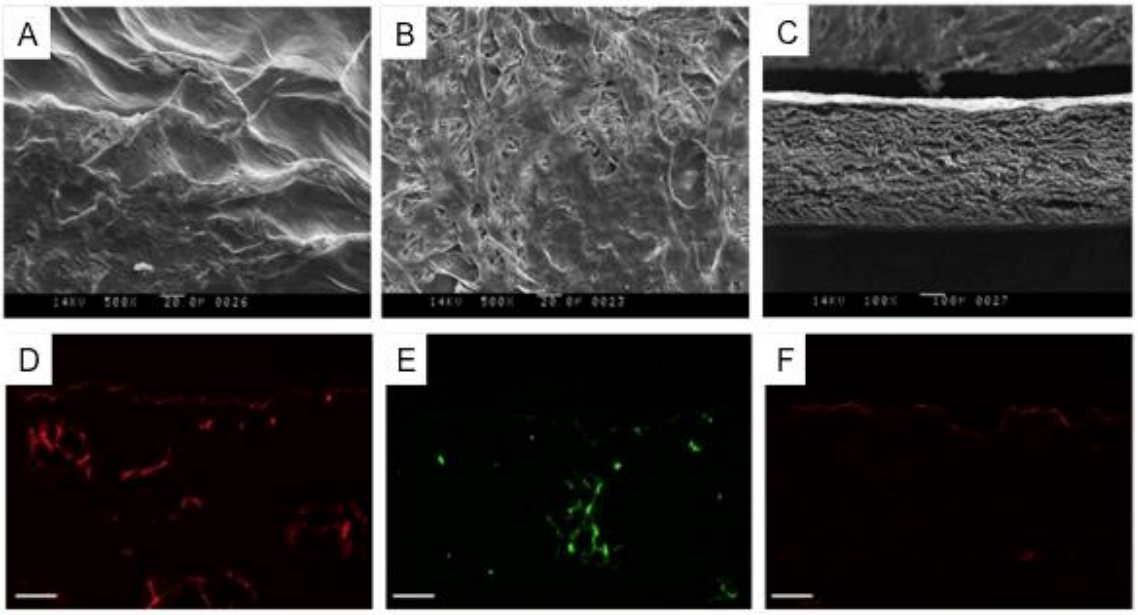

Figure 4.1 Scanning electron microscope images of acellular peritoneum matrix (APM). Shown in (A) MesoBM side, (B) MesoPP side and (C) cross-sectional images. Immnofluorescent staining of APM that retain extracellular matrix proteins: (D) collagen IV, (E) laminin and (F) fibronectin within the cross-sectioned APM. Scale bars = 100 μm.[30]

4.2. Materials and Methods

4.2.1. Acellular peritoneum matrix

The APM was produced from porcine parietal peritoneum using DSM Biomedical's OPTRIX™ processing method. Tissue was harvested from market weight pigs. The peritoneum was dissected from the adjacent pre-peritoneal fat prior to the decellularization process. The OPTRIX™ process consists of a series of agitated washes including an organic solvent, a detergent, salts, an enzyme, and interposed rinses. The processed tissue was freeze-dried and ethylene oxide sterilized in gas permeable packaging. Experimental samples were equivalent to Meso BioMatrix® and Meso Wound Matrix™, which are commercially available.

4.2.2. Mechanical Properties

Mechanical properties were characterized using a mechanical testing instrument (Sintech 5D MTS). APM and cadaver human skin (NY Firefighters skin bank) specimens were cut into rectangular shape measuring 1 cm x 6 cm. Hydrated APM specimens were prepared by soaking in phosphate buffer saline (PBS; Life technologies) for at least one hour. The cadaver skin samples were thawed in PBS and the epithelial side was dapped with Kimwipes to remove excess fluid before testing. Thicknesses of samples were measured with a micrometer immediately before testing (thickness ~ 150-260 μm for APM; 420-550 μm for skin). Samples were mounted between the two grips of Sintech 5D MTS instrument and the distance of grip-to-grip was measured without use of an extensometer. Test speed was set at 10 mm/min.

Stress-strain curve of the samples were obtained. According to Hooke's Law, the stress is directly proportional to the strain in tension:

$$\frac{F}{A} = E\left(\frac{L - Lo}{Lo}\right)$$

where stress, is the applied force, *F*, per unit area of cross section, *A*, and strain is the increase in length from L_0 (original length) to *L* (the length under a given tensile stress) to the relative L_0:

$$\text{Strain} = \frac{\Delta L}{L0} = \frac{L - L0}{L0}$$

The proportionality constant is the Young's modulus, *E*, which measures the hardness and stiffness of the samples. Young's modulus was determined based on calculating the slope of linear portion of the stress-strain curve. The analyses were performed in triplicate.

4.2.3. Cell culture

Neonatal human dermal fibroblasts (HDF) were purchased from Life Technologies. Early passages with passage number no more than 5 were used. Spontaneously immortalized human keratinocyte (HaCaT[14]; passage 20-30), green fluorescent protein (GFP)-expressing HaCaT and red fluorescent protein (RFP)-expressing HDF were generous gifts from the New Jersey Center for Biomaterials. GFP-HaCaT and RFP-HDF were transduced with LifeAct lentiviral vectors[31]; the transduced cells express GFP and RFP on actin filaments of HaCaT and HDF, respectively. All cells were cultured in Dulbecco's modified Eagle's medium (DMEM) with 10% fetal bovine serum (FBS; Life Technologies) and 100 units/mL of penicillin (Life Technologies), 100 μg/mL of streptomycin (Life Technologies) and 0.25 μg/mL of amphotericin B (Life Technologies) at 37°C/ 5% CO_2.

4.2.4. Cellular attachment and growth of skin cells on collagen hydrogel and APM

Collagen hydrogel was prepared by diluting 8 mL of bovine type I collagen solution (6 mg/mL, Nutragen®, Advanced Biomatrix) with 1 mL chilled 10X PBS, 1mL of DMEM medium, and adjusted to pH=7 with 0.1N NaOH. The collagen solution (500 μL) was added to a 48-well tissue culture polystyrene (TCPS) plate and incubated at 37°C overnight before cell seeding. The APM specimens were cut into 12 mm diameter disks and conditioned in the 48-well TCPS plate. Monoculture of HDF or HaCaT ($5x10^4/cm^2$) was seeded onto the type I collagen gel, basement membrane side (MesoBM) of the APM, the opposite side (MesoPP) of the APM, and TCPS wells, respectively.

After 5 hours and 24 hours incubation at 37°C, cells were washed with PBS three times, and then 500 μL of cell culture medium containing 10% (v/v) AlamarBlue® reagent (Life Technologies) was added to each well and incubated for another 3 hours. The fluorescence intensity of the supernatant (λex=560 nm, λem =590 nm) was measured via a plate reader (Tecan Infinite). Attachment % was determined by normalizing the fluorescence intensity (FI) with that from TCPS group. Nine replicates were used in each group for the attachment experiment. To assess cellular metabolic activity at different time points, same seeding parameters and AlamarBlue® assay as described above were used on day 1, 4, 7, 11, and 14. Six replicates were prepared for each time point. The AlamarBlue® results indicate total cellular metabolic activity at different time points.

The skin cells on APM were visualized by fluorescence imaging. GFP-HaCaT and RFP-HDF ($5x10^4/cm^2$) were seeded onto MesoBM side and MesoPP side of APM, respectively. Images were taken using a fluorescence microscope (Zeiss) after four days post-seeding.

4.2.5. Construction of HSEs based on APM

Disks of APM (diameter = 12 mm) were placed in 12-well Transwell® insert plates (polycarbonate 0.45 μm pore size; Corning). At the start of the experiment, 0-$5x10^4$ $/cm^2$ of HDF were seeded to the MesoPP side of the APM. The following day, the ECM specimens were inverted and $5x10^3$ - $5x10^5$ $/cm^2$ of HaCaT were seeded on the MesoBM side of the APM. The HSEs were submerged in culture medium at 37°C/5% CO_2 with medium changes every other day. After 1 week, the constructs were fed with differential medium merely from outer well and cultured at air liquid interface. The differentiation medium contained 3:1 (v/v) of DMEM: EpiLife® with bovine pituitary

extracts (Life Technologies) and final concentration of 25 μM palmitic acid (Sigma Aldrich), 15 μM linoleic acid (Sigma Aldrich), 25 μM oleic acid (Sigma Aldrich), 7 μM arachidonic acid (Sigma Aldrich), 100 μg/mL ascorbic acid (Sigma Aldrich), 10 μM carnitine (Spectrum), 300 μM clofibrate (Sigma Aldrich), 100 μM bovine serum albumin (Sigma Aldrich), and 2 mM calcium chloride (Sigma Aldrich). The relative humidity of incubator was reduced to 75% to stimulate keratinocyte differentiation. The medium was changed every two days and the constructs were cultured for another 2 weeks before harvest. Schematic of the HSEs construction is shown in Figure 4.2.

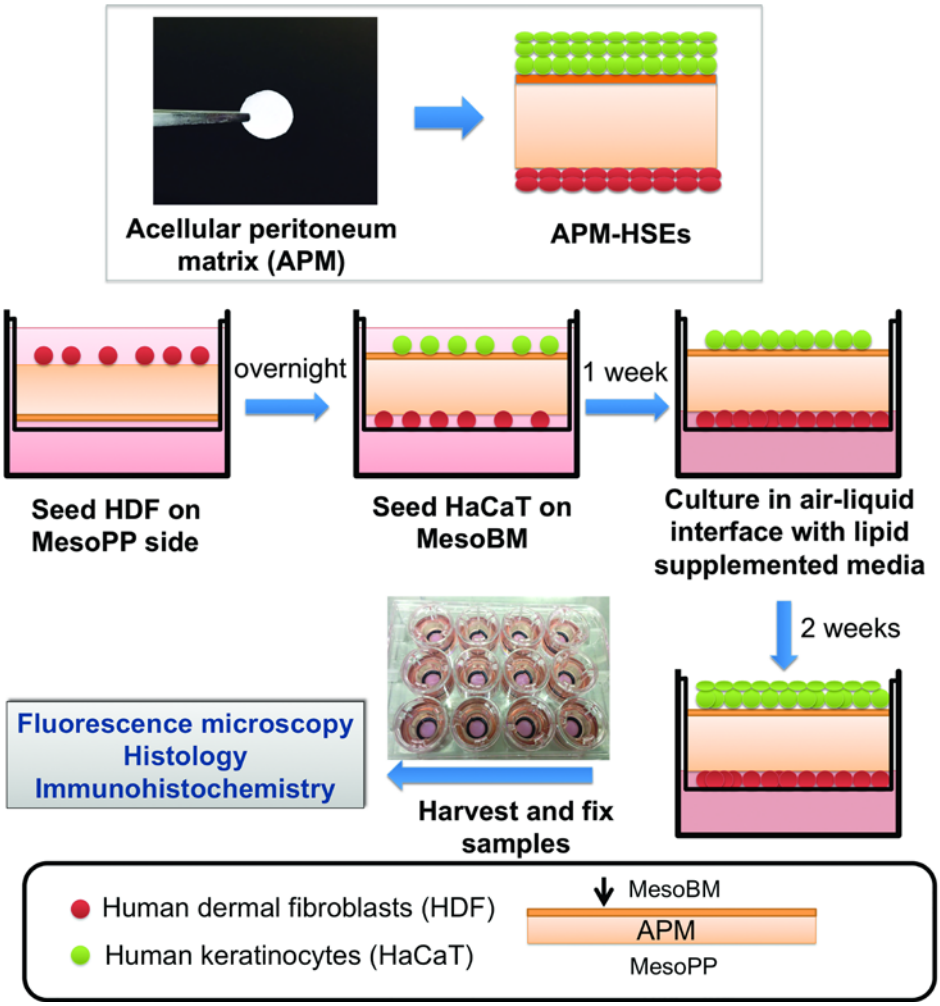

Figure 4.2 Schematic representation of co-culturing HDF and human HaCaT on APM to construct APM-HSEs. Arrow indicates the basement membrane side of the APM

(MesoBM); the opposite side, which faced the pre-peritoneal space, has open fibrous architecture (MesoPP).

4.2.6. H&E staining and immunohistochemical staining

Human cadaver skins (NY Firefighters skin bank; Male/left posterior leg) and APM-HSEs were fixed with 10% buffered formalin (Sigma Aldrich) at room temperature overnight, dehydrated with ethanol and xylene following routine procedures, and embedded in paraffin blocks. The samples were cut into 8 μm thick, deparaffinized with xylene, rehydrated in a gradient of ethanol solutions and stained for standard haematoxylin & eosin (H&E) or immunohistochemical analyses. For immunohistochemical staining, sectioned samples were treated with 0.3% hydrogen peroxide for 10 minutes to block the endogenous peroxide activity. Then the samples were heat treated in 10 mM citrate buffer (Sigma Aldrich), pH 6.0 at 95-100 °C for 30 minutes for antigen retrieval and with protein block reagent (Abcam, mouse specific horseradish peroxidase/3’3’-diaminobenzidine tetrahydrochloride (HRP/DAB) detection kit) overnight at 4 °C. On the following day, the samples were incubated with 1:1500 anti-involucrin (mouse monoclonal primary antibody; Abcam) and 1:50 anti-keratin 15 (Abcam) at room temperature for one hour. Then staining procedure was followed according to the manufacture protocol of mouse specific HRP/DAB detection kit, and haematoxylin counterstaining was performed to label the nuclei.

4.2.7. *In-vitro* skin irritation testing

Polyethylene glycol 400 (PEG 400; EMD), isopropanol (RICCA), 1-bromohexane (Sigma), heptanol (Fisher), and sodium dodecyl sulfate (Sigma) were used as the test

groups (see Table 1); PBS (Life Technologies) was used as control. Freshly prepared APM-HSEs (after 3 weeks' culture; $5x10^4/cm^2$ HaCaT and $5x10^4/cm^2$ HDF) were used in the *in-vitro* irritation validation testing. The medium was removed from the wells and then 25 μL of chemicals were added to the epidermis side of HSEs. The use of 25 μL was enough to uniformly cover the epidermal surface of our APM-HSEs (approximately 0.8 cm^2, i.e., 31.3 $\mu L/cm^2$) while avoiding an infinite dose. This was also based on OECD guideline TG439 that suggested applying the test articles 26-83 $\mu L/cm^2$. All the groups were incubated at 37°C for 60 minutes and followed by washing with PBS for three times. The HSEs were then fed with serum free DMEM medium and incubated at 37°C/5% CO_2 for another 42 hours before viability assay and cytokine secretion detection was performed.

Viability assay (n=6): Cellular viability of APM-HSEs after exposure to chemical groups was evaluated via AlamarBlue® assay. After washing with PBS three times, DMEM containing 10% (v/v) AlamarBlue® reagent was added to both the inner insert (0.5 mL) and outer well (0.5 mL) to be in contact with both MesoBM and MesoPP side of HSEs. After incubated at 37°C for 3 hours, the contacted solutions from the inner insert and outer well were mixed and fluorescence intensity (λex=560 nm, λem =590 nm) of the mixture was measured. Cellular viability of APM-HSEs was normalized to that of the PBS treated group (control).

Cytokine detection (n=4): The levels of extracellular cytokines from chemical treated APM-HSEs were determined by combined solution from inner and outer well. Secretion of IL-1α in medium was detected by ELISA (BioLegend), and secretion of IL-

1ra, IL-6, IL-8, and GM-CSF was detected by Bio-Plex multiplex system (Bio-Rad Laboratories).

4.2.8. Statistical Analysis

Results were expressed as mean ± standard deviation (S.D.). Differences between various chemical treatments and control group were analyzed by ANOVA with post hoc Dunnett's test. Statistical significance analyses of $p < 0.05$ and $p<0.01$ were performed. The cutoff point to differentiate irritant from non-irritant was based on Receiver Operating Characteristic analysis through Prism Software (GraphPad, CA).

4.3. Results

4.3.1. Mechanical Properties

Mechanical properties of dry and hydrated APM specimens and cadaver human skin were evaluated by tensile testing (Figure 4.3.). Dry APM specimens were stiff, and they exhibited a high modulus of 268 ± 27.9 MPa. Hydrated APM specimens showed two slopes in the stress-strain curves, with an initial modulus of 3.5 ± 0.12 MPa, and secondary modulus of 57 ± 1.63 MPa. This two-slope feature in stress-strain curves is a typical characteristic of human skin. Excised human skin specimens showed an initial modulus of 2.9 ± 1.2 MPa, and a secondary modulus of 36 ± 12 MPa.

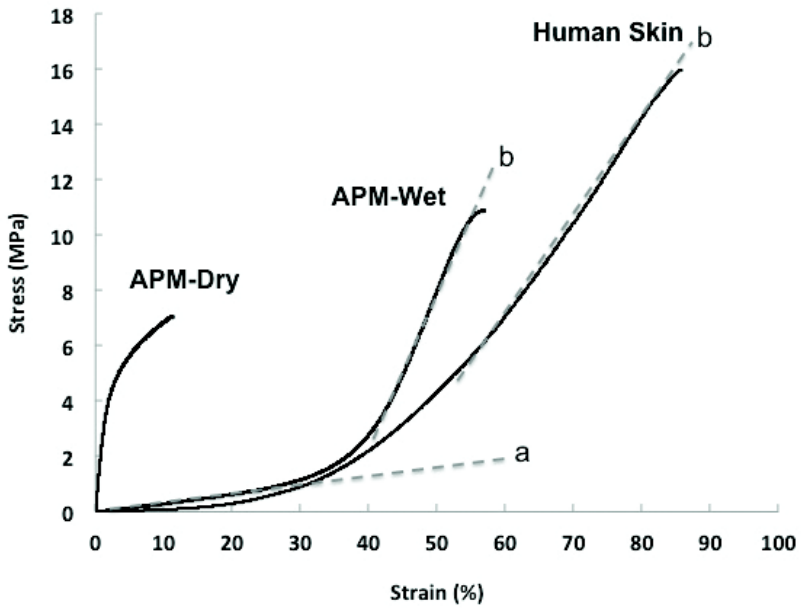

Figure 4.3 Stress-strain curves of APM specimens at dry (APM-Dry), hydrated (APM-Wet) conditions and cadaver human skin. All the tests were performed at room temperature. a=initial slope; b= secondary slope.

4.3.2. APM supports fibroblasts and keratinocytes attachment and growth

Cell adhesion provides essential cues for cells to maintain a normalization of tissue architecture and homeostasis *in-vitro* and *in-vivo*.[32] In this study, we investigated whether APM can support skin cell adhesion and subsequent proliferation, and compared the cellular adhesion and proliferation on the basement membrane and pre-peritoneal sides of APM. Moreover, we compared the APM with bovine type I collagen gel, which is a matrix that is widely used as a dermal substrate in many commercialized HSEs for *in-vivo* skin grafting (e.g., Apligraf®, Orcel™) and *in-vitro* use (i.e., EpiDerm-FT™).[33-35]

Human skin cells, HDF and HaCaT were seeded on the surface of bovine collagen gel and each side of the APM; TCPS was used as control. At 5h and 24h time points, AlamarBlue® assay was performed to assess the cellular attachment % of human skin cells. For cell attachment at 24 h time point, the proliferation of HaCaT and HDF was not taken into account, due to the reported lag time for both HaCaT (24-48 hours[36]) and HDF (24 hours[37]). Our results showed that APM had significantly higher cell attachment compared to type I collagen gel with both type of cells (Figure 4.4.a and 4.4.b), and there was no significant difference of attachment between the basement membrane (MesoBM) side and type I collagen rich side (MesoPP) of APM.

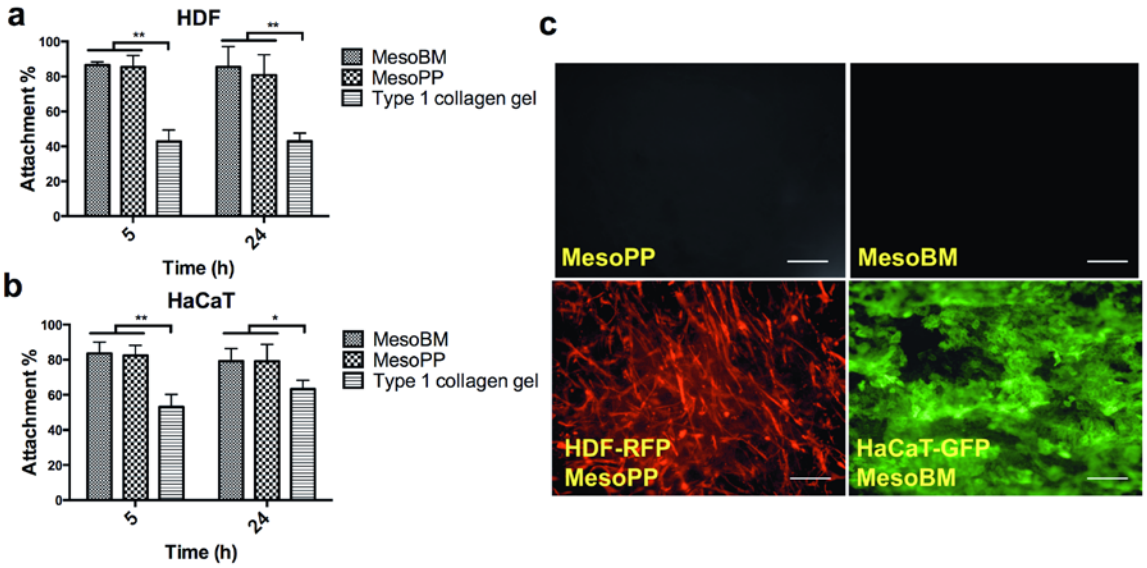

Figure 4.4 Cellular attachment at 5h and 24h time point of (a) human dermal fibroblasts (HDF) and (b) HaCaT, on type I collagen gel and APM (MesoBM: basement membrane side; MesoPP: the pre-peritoneal side). Statistically significant * $p < 0.05$; ** $p < 0.01$ (ANOVA, post hoc Dunnett's test); N=9. Values were normalized with tissue culture plate (100% attachment). Fluorescent microscopy images showing (c) blank MesoPP, blank MesoBM, RFP-expressing HDF on MesoPP, and GFP- expressing HaCaT on MesoBM. Scale bar = 200 μm.

To visualize the skin cells on APM, GFP-expressing HaCaT and RFP-expressing HDF were seeded to the MesoBM side and MesoPP side of the APM, respectively. The seeding of cells in this pattern was to mimic *in-vivo* skin tissues where keratinocytes proliferate and differentiate over a basement membrane structure while the fibroblasts are resident in a type I collagen rich environment. Figure 4.4.c shows the image of cells four days post seeding. The fibroblasts on MesoPP side showed a typical spindle, elongated shape of fibroblast morphology and the keratinocytes on MesoBM side presented their normal morphology in cobblestone-like and mosaic shape.

To determine the metabolic activity of the cells on matrices, HDF and HaCaT were mono-cultured on each side of the APM for 14 days. The metabolic activity of the cells on APM was compared to that of the cells on type I collagen gel and TCPS (Figure 4.5.). For HDF, Figure 4.5.a shows the metabolic activity on APM was similar to that on TCPS, and significantly higher than that on type I collagen gel throughout 14 days of culture. For HaCaT (Figure 4.5.b), interestingly, on type I collagen gel, the metabolic activity-began to increase on day 7. The metabolic activity of HaCaT on APM was higher than that on TCPS (day 11 and day 14), and that metabolic activity of HaCaT on TCPS was higher than that on type I collagen gel. Overall, APM promoted the attachment and viability of HDF and HaCaT *in-vitro* as compared to collagen gel.

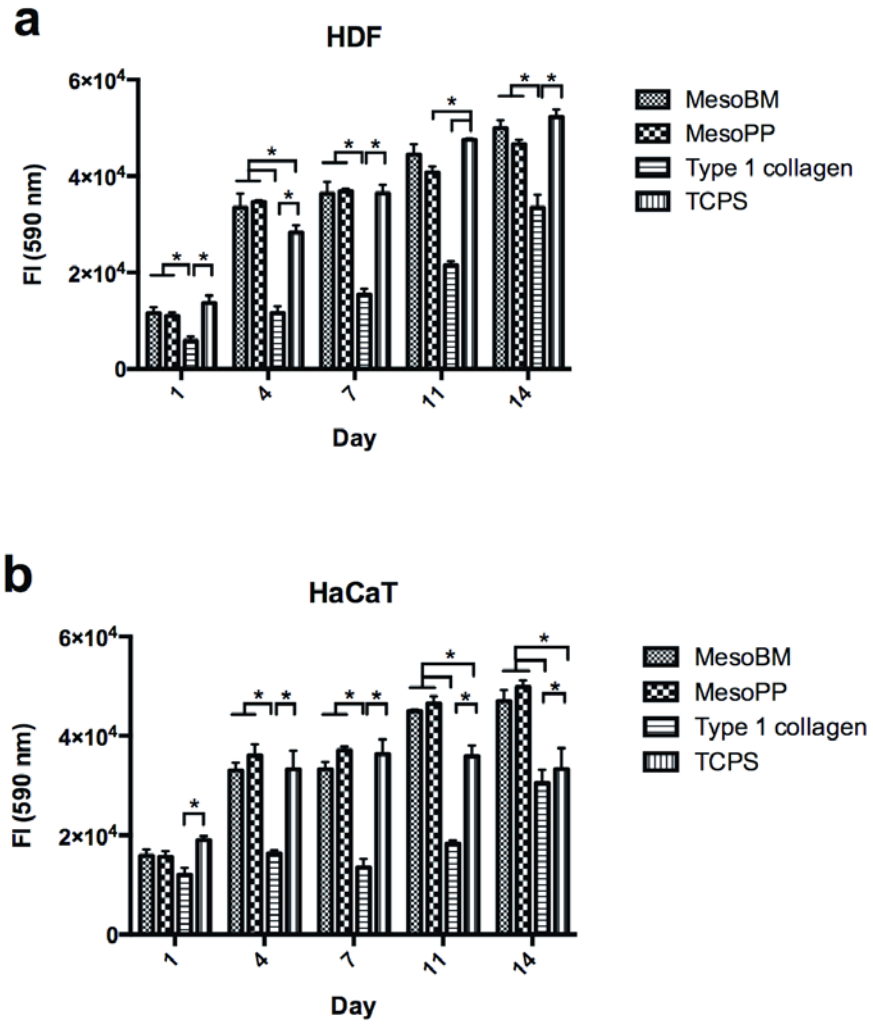

Figure 4.5 Metabolic activity of (a) HDF and (b) HaCaT on APM (MesoBM, MesoPP), type I collagen gel and TCPS. AlamarBlue® assay was performed on day 1, 4, 7, 11, and 14. * Indicates statistically difference $p<0.05$ (ANOVA, post hoc Dunnett's test); N=6.67

4.3.3. Development of APM-HSEs with multiple cell layers

Acellular Peritoneum Matrix HSEs were constructed by seeding HDF on the MesoPP side and followed by seeding HaCaT on the MesoBM side of APM to simulate the cellular distribution of *in-vivo* environment. The co-cultured constructs were then submerged in culture medium for one week and transferred to an air-liquid interface for another two weeks to induce keratinocyte differentiation.[38] The APM-HSEs were then harvested on day 21 and fixed for histology analysis. Histological H&E analysis of cross-

sections showed that HaCaT and HDF were able to grow into multiple layers on MesoBM side and MesoPP side of APM, respectively (Figure 4.6.a). Migration of the cells to inner layers of ECM was not observed. In HaCaT layers, flattening of nuclei and formation of *stratum spinosum*-like structures were observed, demonstrating differentiation of the HaCaT. The epithelial thickness and structure formation from HaCaT were highly influenced by the seeding density of HDF *in-vitro* (Figure 5.6.b). Increased HDF seeding density to $5x10^4/cm^2$ on APM resulted in the formation of thickest and most organized epidermis (Figure 4.6.b, 4.6.d), while increasing the seeding density of HaCaT did not improve the thickness nor organization of epidermal or HDF layer (Figure 4.6.c, e). Overall, our H&E images indicated that APM supported the growth of HDF, proliferation and differentiation of HaCaT to form a partially differentiated full thickness HSEs, and the thickness of epidermal layers was affected by the seeding density of HDF.

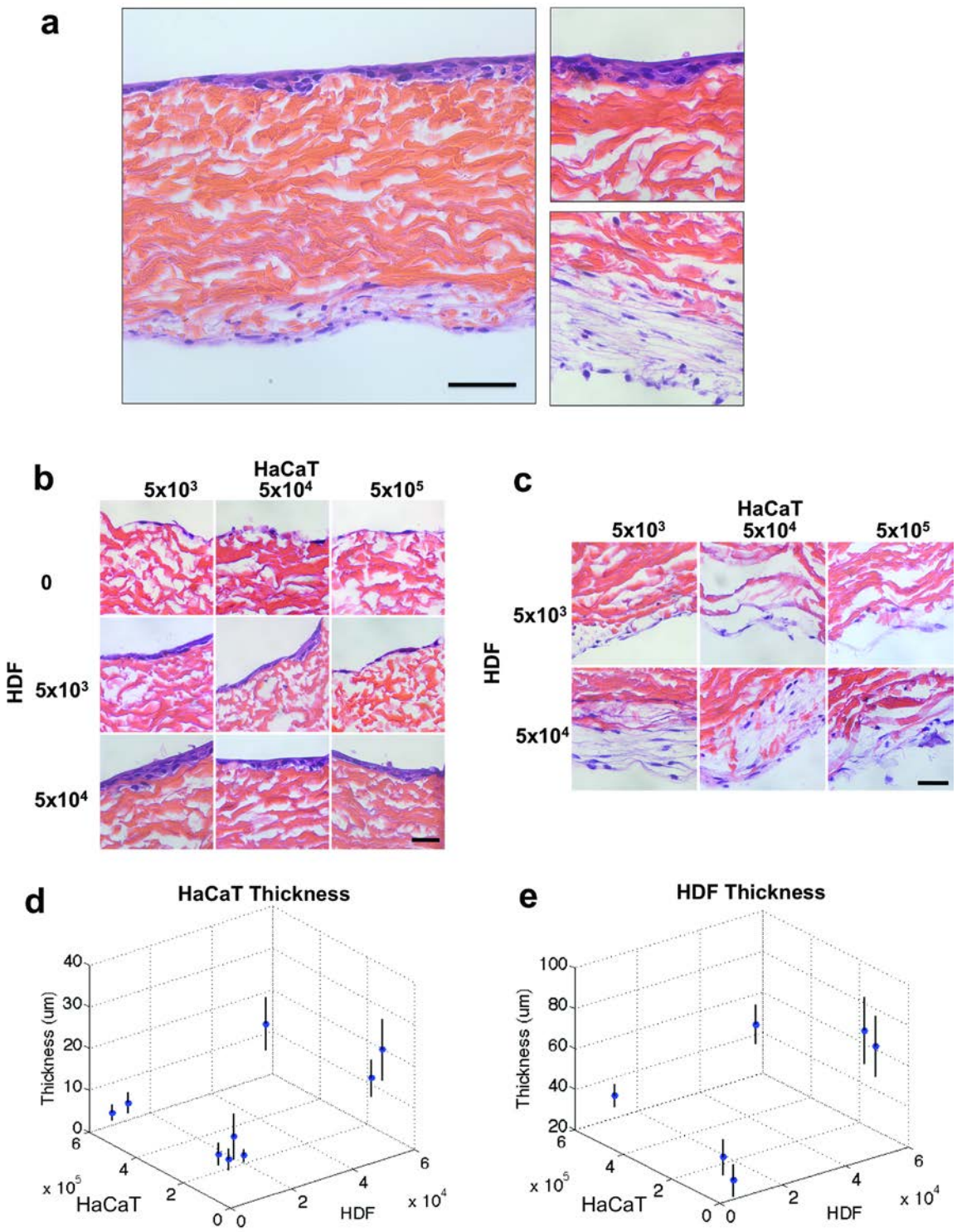

Figure 4.6 Histological H&E analysis and cell layer thickness of constructed APM-HSEs at day 21. (a) Cross-section of APM-HSEs, (b) epithelial structure of APM-HSEs with different HDF/HaCaT seeding density, (c) HDF layers of APM-HSEs with different HDF/HaCaT seeding density, (d) HaCaT thickness of HSEs, (e) HDF thickness of HSEs.

Scale bars indicate 50 μm. Image analyses of HaCaT and HDF thickness were quantified by Image J and plotted by MATLAB software.

4.3.4. Keratinocyte proliferation and differentiation markers

The expression of keratinocyte proliferation and differentiation on APM-HSEs were further examined by performing immunohistochemistry staining of keratin 15 and involucrin markers, respectively (Figure 4.7.). Cadaver human skin specimens were used as reference material. Keratin 15 is a keratinocyte proliferation marker and is found to mark putative stem and progenitor cells located in *stratum basale*.[39] Involucrin, a keratinocyte differentiation marker, is a cornified envelope protein marker that is highly expressed in supra *stratum granulosum* layer of epidermis in native human skin.[40] Immunohistochemistry staining of cadaver human skin specimens indicated well-stratified viable epidermis layers, i.e., basal layer expressing keratin 15 (Figure 4.7.a) and supra *stratum granulosum* layers expressing involucrin (Figure 4.7.c). For APM-HSEs specimens, there was very low level of keratin 15 detected (Figure 4.7.b), and the expression pattern of keratin 15 was irregular compared to cadaver human skin (staining on basal layer is evident) (Figure 4.7.a). The expression of involucrin was evident in the outermost layer of APM-HSEs, which was similar to human skin (Figure 4.7.c and 4.7.d). While in normal native skin, proliferation and differentiation of keratinocytes are well balanced and hence the *stratum corneum* is formed; our immnohistochemistry images suggested the epidermal layers of the APM-HSEs contained differentiated and viable cell layers but had no *stratum corneum* and were less organized than native human skin.

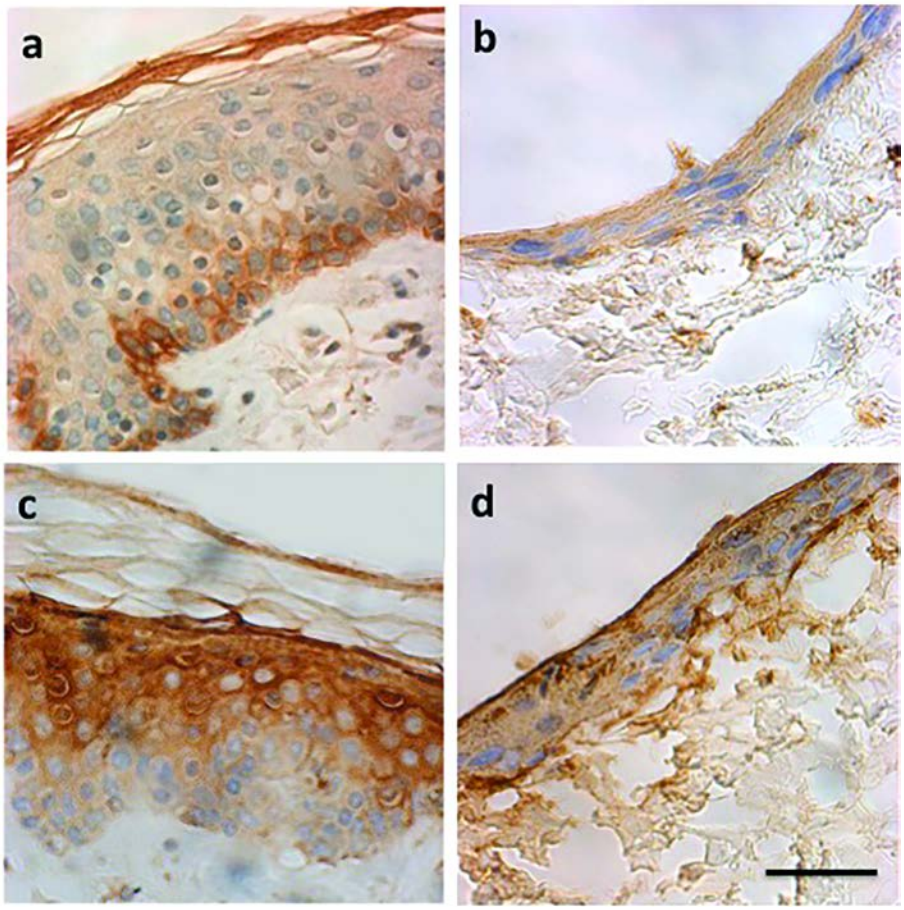

Figure 4.7 Immunohistochemistry labeling of keratinocyte proliferation marker, keratin 15 (a-b), and differentiation marker, involucrin (c-d) of human cadaver skin (a), (c) and APM-HSEs (b), (d), respectively. Protein markers were stained with horseradish peroxidase/3'3'-diaminobenzidine tetrahydrochloride (HRP/DAB) to produce brown color, and cell nuclei were stained with haematoxylin as shown in blue. Scale bar indicates 50 μm.

4.3.5. *In-vitro* irritation testing on APM-HSEs

To examine the potential of APM-HSEs models for irritancy screening, six proficiency chemicals (Table 4.1.) were selected based on OECD T439 guidelines for *in-vitro* skin irritation.[29] The choice of irritants and their concentrations is based on either OECD TG439 guidelines (i.e., PBS, 1-bromohexane and heptanol), or published concentrations from literature[41] (i.e., 20% SDS, polyethylene glycol 400). The selected

chemicals were applied to the freshly prepared APM-HSEs (at week 3 time point of HaCaT/HDF co-culture) for 60 min at 37°C, and end point analyses were performed 42 hours post treatment. End point analyses included cellular viability and quantification of the extracellular release of five cytokines into the medium (Figure 4.9.). APM-HSEs treated with PBS were considered as control group based on the OECD T439 guidelines.

Table 4.1 Selected chemicals used in *in-vitro* irritation testing.

Chemical	**Classified**	***In-vivo* score[a]**
Phosphate buffer saline (PBS)	Non irritant	0
Polyethylene glycol 400 (PEG 400)	Non irritant	0
Isopropanol (70% v/v)	Non irritant	0.3
1-bromohexane	Irritant	2.7
Potassium hydroxide (5% v/v)	Irritant	3
Heptanal	Irritant	3.4
Sodium dodecyl sulfate (20% w/v)	Irritant	4

[a] Known *in-vivo* score from albino rabbit Draize test (OECD T404).

Viability data showed that APM-HSEs responded to irritant ranking in a consistent manner. Cellular viability decreased with increasing ranking of irritation of the chemicals (Figure 4.9.a). When comparing the viability to PBS control group without any chemicals (set as 100%), the cellular viabilities of treated group can be used to discriminate between non-irritants and irritants (Table 4.2). The cutoff point to differentiate irritant from non-irritant was 71.7% viability based on Receiver Operating Characteristic analysis (Figure 4.8. and Table 4.3.). In order to establish cutoff value for viability data, statistic method as the Receiver Operating Characteristic curve (ROC) was used. The curve is created by plotting true positive rate (sensitivity) against the false positive rate (1 − Specificity) at various threshold settings. The cutoff value which corresponds to the point nearest to upper left of ROC graph indicates highest sensitivity

and specificity. We analyzed our viability data through Prism Software (GraphPad, CA USA) based on the response of chemical treated-HSE to known classification of chemicals. According to the Table 4.3, threshold at 71.7% achieve sensitivity of 0.8974 and specificity of 1, and it was suggested to be the optimum cutoff value in this assay. Moreover, the larger Area Under the ROC Curve (AUC) suggests the higher degree of accuracy of the test. Our ROC curve shows AUC near 1 (AUC=0.95), which indicates high accuracy of the assay.

All chemicals excepting heptanol and SDS (these two groups resulted in viability < 5%) were further analyzed for cytokine secretions to confirm ranking order of the irritants.

Table 4.2 Classification of non-irritating (NI) and irritating (I) chemicals in the APM-HSEs based on viability (cutoff at 71.7%).

No.	Chemical	Entry	Viability %	Judg-ment	Mean	SD	Judg-ment	*In-Vivo* Class
1	PEG 400	1	106.6	NI	111.9	11.6	NI	NI
		2	123.4	NI				
		3	115.3	NI				
		4	119.8	NI				
		5	113.8	NI				
		6	92.3	NI				
2	Isopropanol; 70% (v/v)	1	86.9	NI	80.9	3.84	NI	NI
		2	78.6	NI				
		3	83.5	NI				
		4	81.5	NI				
		5	78.2	NI				
		6	76.7	NI				
3	1-bromohexane	1	66.7	I	62.4	22.58	I	I
		2	83.6	NI				
		3	93.7	NI				
		4	41	I				
		5	42.1	I				
		6	47.2	I				
4	Heptanol	1	4.2	I	4.5	0.69	I	I
		2	3.6	I				
		3	3.9	I				
		4	5	I				
		5	5.3	I				
		6	5.1	I				
5	SDS (20% w/v)	1	3.3	I	3.9	0.62	I	I
		2	3.3	I				
		3	3.3	I				
		4	4.3	I				
		5	4.5	I				
		6	4.5	I				

Table 4.3 Sensitivity and specificity report of APM-HSEs irritation testing.

Threshold value %<	Sensitivity	95% CI	Specificity	95% CI
3.45	0.1579	0.03383 to 0.3958	1	0.7354 to 1.000
3.75	0.2105	0.06052 to 0.4557	1	0.7354 to 1.000
4.05	0.2632	0.09147 to 0.5120	1	0.7354 to 1.000
4.25	0.3158	0.1258 to 0.5655	1	0.7354 to 1.000
4.4	0.3684	0.1629 to 0.6164	1	0.7354 to 1.000
4.75	0.5263	0.2886 to 0.7555	1	0.7354 to 1.000
5.05	0.5789	0.3350 to 0.7975	1	0.7354 to 1.000
5.2	0.6316	0.3836 to 0.8371	1	0.7354 to 1.000
23.15	0.6842	0.4345 to 0.8742	1	0.7354 to 1.000
41.5	0.7368	0.4880 to 0.9085	1	0.7354 to 1.000
44.6	0.7895	0.5443 to 0.9395	1	0.7354 to 1.000
56.95	0.8421	0.6042 to 0.9662	1	0.7354 to 1.000
71.7	0.8947	0.6686 to 0.9870	1	0.7354 to 1.000
77.45	0.8947	0.6686 to 0.9870	0.9167	0.6152 to 0.9979
78.4	0.8947	0.6686 to 0.9870	0.8333	0.5159 to 0.9791
80.05	0.8947	0.6686 to 0.9870	0.75	0.4281 to 0.9451
82.5	0.8947	0.6686 to 0.9870	0.6667	0.3489 to 0.9008
83.55	0.8947	0.6686 to 0.9870	0.5833	0.2767 to 0.8483
85.25	0.9474	0.7397 to 0.9987	0.5833	0.2767 to 0.8483
89.6	0.9474	0.7397 to 0.9987	0.5	0.2109 to 0.7891
93	0.9474	0.7397 to 0.9987	0.4167	0.1517 to 0.7233
100.2	1	0.8235 to 1.000	0.4167	0.1517 to 0.7233
110.2	1	0.8235 to 1.000	0.3333	0.09925 to 0.6511
114.6	1	0.8235 to 1.000	0.25	0.05486 to 0.5719
117.6	1	0.8235 to 1.000	0.1667	0.02086 to 0.4841
121.6	1	0.8235 to 1.000	0.08333	0.002108 to 0.3848

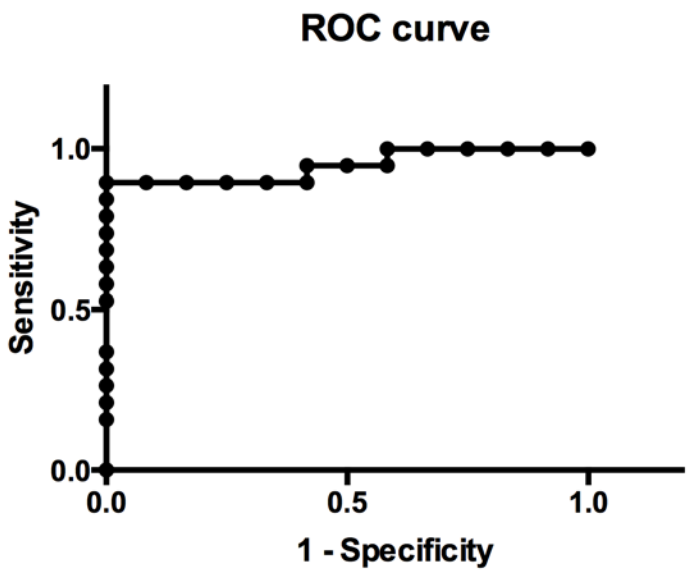

Figure 4.8 Receiver Operating Characteristic (ROC) curve of APM-HSEs viability data.

During skin inflammatory process *in-vivo*, pro-inflammatory cytokines including IL-1α, IL-6, IL-8 and GM-CSF are secreted together by keratinocytes, fibroblasts, Langerhans, monocytes and T cells. Upon irritant stimuli, keratinocytes secrete IL-1α, a primary cytokine that initiate inflammatory cascade. The activation of IL-1α stimulates further production of secondary pro-inflammatory cytokines (e.g., IL-8, IL-6, GM-CSF) by surrounding epidermal and dermal cells[42]. In our study, both primary and secondary pro-inflammatory cytokines were detected. The concentrations of secreted IL-1α were detected in isopropanol (12.37 ± 3 pg/mL) and 1-bromohexane (49.5 ± 16.7 pg/mL) treatments, and it was under detection limit for PBS and PEG 400 treatments (Figure 4.9.b). IL-1ra, a natural antagonist of IL-1α that prevents damages of exceeded IL-1α significant increased from 1-bromohexane treatment compared with PBS and PEG 400 groups (Figure 4.9.c). IL-6 and IL-8 are secondary pro-inflammatory cytokines and chemotactic for neutrophils. Secretion of secondary cytokines IL-6 and IL-8 followed a

similar trend as mentioned above. Importantly, increase in the *in-vivo* irritation scores resulted in significantly increased cytokine productions (Figure 4.9.d and 4.9.e). Also the secretion of GM-CSF, a cytokine that enhances effector function of monocytes and neutrophils was significantly increased for those treated with 1-bromohexane (Figure 4.9.f).

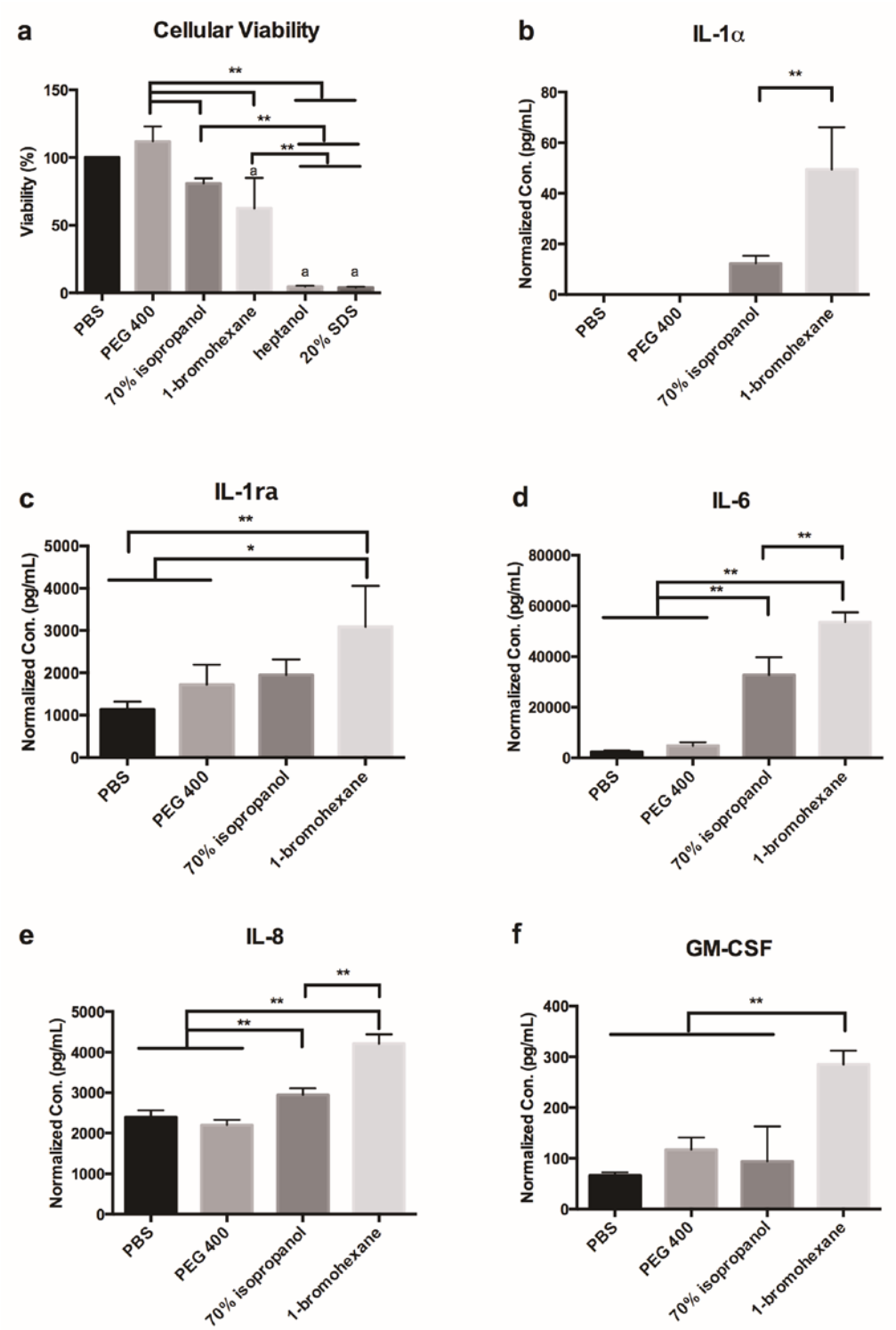

Figure 4.9 Cellular viability (a) and release of inflammatory biomarkers from APM-HSEs 42 hours post treatment (b-f). Cytokine concentrations (con.) of IL-1α (b), IL-1ra (c), IL-6 (d), IL-8 (e), and GM-CSF (f) that were secreted to the medium were normalized by their mean viability. Data is expressed as mean ± S.D.; N=6 for viability and N=4 for inflammatory biomarkers. Statically significant * ($p<0.05$); statically

significant ** ($p<0.01$); “a” indicates significant ($p<0.01$) compared with PBS group (ANOVA post hoc Dunnett’s test).

4.4. Discussion

Predictive *in-vitro* assays that can identify skin irritation are in demand to reduce and replace the use of animal testing. Ideal 3D skin models for *in-vitro* assays should possess (a) high accuracy, sensitivity, specificity, (b) represent native skin composition and physiology, (c) resemble native skin barrier properties, (d) be highly available, (e) provide high-throughput screening, (f) be consistent in batch-to-batch culture, and (g) have long shelf life. However, the ideal 3D skin models that fulfilled the above criteria are still yet to be developed.

Over the past decade, type I collagen hydrogel has been the dominant material used to construct full-thickness HSEs, based on the high biocompatibility and the nature of collagen representing ECM properties. However, the extraction process of collagen utilizes harsh treatments of acid and proteolytic solutions, which alter its molecular structures by cleaving terminal telopeptides. This results in decreased tropocollagen self-assembled fibrils and partially denatures the collagen.[43] The collagen gels lack the mature collagen fiber hierarchical structure and biological diversity of ECM proteins present in decellularized tissues. The partially denatured collagen affects mechanical properties of the constructed HSEs and results in variable surface area, shape and thickness of HSEs models. The extent of contraction is also affected by collagen concentration, number of fibroblasts seeded in the matrix and HSEs culture time. On the other hand, decellularization processes remove cells and antigenic compounds, while preserving the

native ECM structure, tissue strength, and distribution of cell attachment proteins and growth factors.

The feasibility of using APM as a substrate to develop full-thickness skin tissue was evaluated. The hydrated APM specimens exhibited non-linear tensile properties that represent mechanical properties of human skin: both the hydrated APM and excised skin specimens showed a two-slope stress strain feature. The modulus values of hydrated APM (initial slope= 3.5 ± 0.12 MPa; secondary slope= 57 ± 1.63 MPa, Figure 4.3) were similar to those of excised human skin (initial slope= 2.9 ± 1.2 MPa, secondary slope= 36 ± 12 MPa). This phenomenon is due to the degree of alignment from the collagen and elastic fibers.[44] In comparison, the modulus of collagen gels has been reported in the range of 1.5-24.3 kPa.[45] The intact mature ECM structure of APM enables development of APM-HSEs with relatively controlled dimensions and excellent handling properties. The APM supported the attachment and growth of HDF and HaCaT, significantly better than the type I collagen gel. This could be explained by mechanical cues that result from the increased modulus of APM versus collagen gels.

Further, we attempted to construct a full-thickness HSE based on co-culturing human skin cells on the decellularized ECM. Primary keratinocytes, although easy to stratify into *stratum corneum* structures, have limited life span, rapidly die after induced differentiation and are difficult to expand into large quantity. HaCaT, a spontaneously immortalized human keratinocyte cell line was used in this study, as it exhibits basal cell properties, is highly available and easier to expand compared to primary keratinocytes, which might be more suitable for *in-vitro* assays. Immortalized cell lines have shown utility in the construction of HSEs, for example, normal immortal keratinocytes (NIKS)

mutated from BC-1 EP strain of normal human neonatal foreskin provide indefinitely culture, near diploid karyotype in monoculture and established fully stratified epidermis and less batch-to-batch variability in HSEs.[15] However, for commercialization, there will be licensing issues associated with the use of HaCaT.

In our study, although excellent support of attachment and proliferation of fibroblasts and HaCaT on APM was observed, the 3D co-culture of HDF and HaCaT resulted in HSEs with partially differentiated epidermis layer (Figure 4.6 a) This partially differentiation may be due to the natural difference of HaCaT from primary keratinocytes, where deficiency in epithelial-stromal interactions and decreased secretion of paracrine IL-1α were found in the HaCaT.[46] Ideally, *stratum corneum* should be present to provide proper barrier to reflect the permeation of irritation compounds to viable epidermal and dermal layers. However, commercially marketed skin models with fully stratified *stratum corneum* still face the challenge of exhibiting inferior barrier properties compared with those of human skin.[47, 48] Despite the differences of HaCaT from primary keratinocytes, supplementing addition growth factors such as transforming growth factor (TGF-α), keratinocyte growth factor (KGF) and granulocyte macrophage colony-stimulating factor (GM-CSF) during *in-vitro* culture can rescue the normal differentiation.[46] Interestingly, we found increasing seeding density of HDF improved the thickness and organized morphology of HSEs epidermis layer *in-vitro* (Figure 4.6 b). This finding is in agreement with several studies that suggested paracrine effect from stromal cells could also affect epidermal homeostasis.[20, 46] Therefore, by further optimizing *in-vitro* culture conditions, we may obtain fully stratified epidermis from HaCaT.

Skin irritation is a complex process that involves penetration of chemical through skin layers, disruption of skin barrier and induction of pro-inflammatory cytokine cascades through keratinocytes, fibroblasts, Langerhan's cells and T-cells. Ideally, full-thickness HSEs should be applied to study skin irritation as they resemble skin more than epidermal models due to their higher complexity in cell types and skin strata. However, all the current OECD approved HSE models for irritation tests are epidermis models[29]. Few reports have used full-thickness models that contain keratinocytes on fibroblasts-populated collagen matrices to predict the secretion of secondary pro-inflammatory cytokines (e.g., IL-6, IL-10) that are not detected in epidermal model.[49, 50] Mallampati et al. used a full-thickness model, EpiDerm-FT™(MatTek) to study the toxic effect and structural activity relationship from saturated aliphatic hydrocarbons. Endpoint evaluations such as cellular viability and pro-inflammatory cytokines (IL-1α, IL-6, IL-8) demonstrated that it is possible to rank the toxicity effect of various hydrocarbon chain length and the *in-vitro* results were correlated with *in-vivo* data.[49] Similar, in another study, Black et al. has demonstrated the use of EpiDerm-FT™ to identify the molecular mechanism of skin inflammatory caused by sulfur mustard.[51] It should be noted that EpiDerm-FT™ is based on collagen hydrogels. The contraction of collagen gel by the skin cells often results in unpredictable variations in specimen thickness and surface area. Collagen gels are fragile with undesirable mechanical strength and are often difficult to handle. Decellularized tissues, such as acellular peritoneum matrix (APM), are attractive biomaterials to construct full-thickness HSEs for *in-vitro* testing, as they highly retain the 3D structure, mechanical properties and biochemical composition of ECM.[30]

In our study, APM-HSEs containing both the viable epidermis and dermis components were used for skin irritation test. Three non-irritants (i.e., PBS, PEG 400, isopropanol) and three irritants (i.e., 1-bromohexane, hepanol, SDS) were applied on the epithelial surface of APM-HSEs model and used to evaluate the *in-vitro* prediction of irritancy through viability and cytokine secretion. In OECD TG439 guideline, the viability cutoff point is 50%. The guideline is established for reconstructed human epidermis models; therefore the viability is simply based on viable keratinocytes. In our study using APM-HSEs, our cutoff point is 71.7 %. This is due to the feature of our APM-HSEs model, comprising not only viable keratinocytes, but also fibroblasts, which will also contribute to the overall viability. In addition, the test compounds would have to diffuse through APM-HSEs to reach the underneath fibroblast. While viability itself can distinguish irritants from non-irritants, primary and secondary cytokine production can further differentiate the irritation potency of various compounds. However, to evaluate the true predictive power of APM-HSEs in skin irritation testing, accuracy, sensitivity and specificity of the test needs to be validated with an expanded panel, with variants from concentrations and types of chemicals and topical formulations.

Table 4.4 Comparison of accuracy, sensitivity, and specificity of APM-HSEs with commercialized epidermal HSE models in irritation tests.

Test Model	Accuracy %	Sensitivity %	Specificity %	Ref.
EpiDerm™	80.6	86	76	41
Episkin™	81.3	85	78.6	52
SkinEthic™	85	90	80	53
LabCyte	79	78	80	54
APM-HSEs (cutoff at 71.7%)	93	89	100	

Accuracy % = [(number of true positive + number of true negative)/ total population] x 100
Sensitivity % = [number of true positive/ (number of true positive + false negative)] x 100

Specificity % = [number true negative/ (number of false positive + true negative)] x 100

4.5. Conclusions

In this study, we demonstrated that APM supported attachment and proliferation of fibroblasts and HaCaT. The APM was used as a substrate to aid the development of advanced full-thickness skin models with multiple cell types co-cultured on a single skin model. The constructed APM-HSEs resulted in a partially differentiated epidermis. Further, the cultured APM-HSEs models functioned as an *in-vitro* irritation screening tool for topically applied compounds. The APM-HSEs were able to classify topically applied non-irritants from irritants and differentiated their irritation rankings through the viability and levels of multiple cytokines secreted from the epidermal and dermal cells. In conclusion, we have demonstrated the use of APM to support the development of HSEs. We envision APM-HSEs to be valuable tools for *in-vitro* screening of topically applied drugs in the future.

4.6. References

1. Draize, J.H., Woodard, G., and Calvery, H.O. Methods for the study of irritation and toxicity of substance applied topically to the skin and mucous membranes. J Pharmacol ExpTher 82, 377, 1944.
2. Ngo, M.A., and Maibach, H.I. Dermatotoxicology: historical perspective and advances. Toxicol Appl Pharmacol 243, 225, 2010.
3. Phillips, L., 2nd, Steinberg, M., Maibach, H.I., and Akers, W.A. A comparison of rabbit and human skin response to certain irritants. Toxicol Appl Pharmacol 21, 369, 1972.
4. Vinardell, M.P., and Mitjans, M. Alternative methods for eye and skin irritation tests: an overview. J Pharm Sci 97, 46, 2008.
5. Robinson, M.K., McFadden, J.P., and Basketter, D.A. Validity and ethics of the human 4-h patch test as an alternative method to assess acute skin irritation potential. Contact Dermatitis 45, 1, 2001.
6. Golla, S., Madihally, S., Robinson, R.L., Jr., and Gasem, K.A. Quantitative structure-property relationships modeling of skin irritation. Toxicol In Vitro 23, 176, 2009.
7. Notman, R., and Anwar, J. Breaching the skin barrier--insights from molecular simulation of model membranes. Adv Drug Deliv Rev 65, 237, 2013.

8. Zhang, Z., and Michniak-Kohn, B.B. Tissue engineered human skin equivalents. Pharmaceutics 4, 26, 2012.
9. Brohem, C.A., Cardeal, L.B., Tiago, M., Soengas, M.S., Barros, S.B., and Maria-Engler, S.S. Artificial skin in perspective: concepts and applications. Pigment Cell Melanoma Res 24, 35, 2011.
10. Hoffmann, J., Heisler, E., Karpinski, S., Losse, J., Thomas, D., Siefken, W., Ahr, H.J., Vohr, H.W., and Fuchs, H.W. Epidermal-skin-test 1,000 (EST-1,000)--a new reconstructed epidermis for in vitro skin corrosivity testing. Toxicol In Vitro 19, 925, 2005.
11. Netzlaff, F., Lehr, C.M., Wertz, P.W., and Schaefer, U.F. The human epidermis models EpiSkin, SkinEthic and EpiDerm: an evaluation of morphology and their suitability for testing phototoxicity, irritancy, corrosivity, and substance transport. Eur J Pharm Biopharm 60, 167, 2005.
12. Ackermann, K., Lombardi Borgia, S.L., Korting, H.C., Mewes, K.R., and Schafer-Korting, M. The Phenion full-thickness skin model for percutaneous absorption testing. Skin Pharmacol Physiol 23, 105, 2010.
13. Flamand, N., Marrot, L., Belaidi, J.P., Bourouf, L., Dourille, E., Feltes, M., and Meunier, J.R. Development of genotoxicity test procedures with Episkin, a reconstructed human skin model: towards new tools for in vitro risk assessment of dermally applied compounds. Mutat Res 606, 39, 2006.
14. Boukamp, P., Petrussevska, R.T., Breitkreutz, D., Hornung, J., Markham, A., and Fusenig, N.E. Normal keratinization in a spontaneously immortalized aneuploid human keratinocyte cell line. J Cell Biol 106, 761, 1988.
15. Allen-Hoffmann, B.L., Schlosser, S.J., Ivarie, C.A., Sattler, C.A., Meisner, L.F., and O'Connor, S.L. Normal growth and differentiation in a spontaneously immortalized near-diploid human keratinocyte cell line, NIKS. J Invest Dermatol 114, 444, 2000.
16. Rosdy, M., and Clauss, L.C. Terminal epidermal differentiation of human keratinocytes grown in chemically defined medium on inert filter substrates at the air-liquid interface. J Invest Dermatol 95, 409, 1990.
17. Poumay, Y., Dupont, F., Marcoux, S., Leclercq-Smekens, M., Herin, M., and Coquette, A. A simple reconstructed human epidermis: preparation of the culture model and utilization in in vitro studies. Arch Dermatol Res 296, 203, 2004.
18. Kubo, K., and Kuroyanagi, Y. Characterization of a cultured dermal substitute composed of a spongy matrix of hyaluronic acid and collagen combined with fibroblasts. J Artif Organs 6, 138, 2003.
19. Lee, D.Y., Ahn, H.T., and Cho, K.H. A new skin equivalent model: dermal substrate that combines de-epidermized dermis with fibroblast-populated collagen matrix. J Dermatol Sci 23, 132, 2000.
20. Schoop, V.M., Mirancea, N., and Fusenig, N.E. Epidermal organization and differentiation of HaCaT keratinocytes in organotypic coculture with human dermal fibroblasts. J Invest Dermatol 112, 343, 1999.
21. Guo, Z., C. Higgins, B. Gillette, and Chistiano, A. Building a microphysiological skin model from induced pluripotent stem cells. Stem Cell Res & Ther 4, S2, 2013.
22. Chau, D.Y., Johnson, C., MacNeil, S., Haycock, J.W., and Ghaemmaghami, A.M. The development of a 3D immunocompetent model of human skin. Biofabrication 5, 035011, 2013.
23. Shamis, Y., Hewitt, K.J., Carlson, M.W., Margvelashvilli, M., Dong, S., Kuo, C.K., Daheron, L., Egles, C., and Garlick, J.A. Fibroblasts derived from human embryonic stem cells direct development and repair of 3D human skin equivalents. Stem Cell Res Ther 2, 10, 2011.
24. Tonello, C., Zavan, B., Cortivo, R., Brun, P., Panfilo, S., and Abatangelo, G. In vitro reconstruction of human dermal equivalent enriched with endothelial cells. Biomaterials 24, 1205, 2003.

25. Duval, C., Chagnoleau, C., Pouradier, F., Sextius, P., Condom, E., and Bernerd, F. Human skin model containing melanocytes: essential role of keratinocyte growth factor for constitutive pigmentation-functional response to alpha-melanocyte stimulating hormone and forskolin. Tissue Eng Part C Methods 18, 947, 2012.
26. Herson, M.R., Mathor, M.B., Altran, S., Capelozzi, V.L., and Ferreira, M.C. In vitro construction of a potential skin substitute through direct human keratinocyte plating onto decellularized glycerol-preserved allodermis. Artif Organs 25, 901, 2001.
27. Bannasch, H., Stark, G.B., Knam, F., Horch, R.E., and Fohn, M. Decellularized dermis in combination with cultivated keratinocytes in a short- and long-term animal experimental investigation. J Eur Acad Dermatol Venereol 22, 41, 2008.
28. Bannasch, H., Unterberg, T., Fohn, M., Weyand, B., Horch, R.E., and Stark, G.B. Cultured keratinocytes in fibrin with decellularised dermis close porcine full-thickness wounds in a single step. Burns 34, 1015, 2008.
29. OECD. Organisation for Economic Co-operation and Development (OECD)-TG 439 In vitro Skin Irritation: Reconstructed Human Epidermis Test Method. Guidelines for the Testing of Chemicals 2013.
30. Hoganson, D.M., Owens, G.E., O'Doherty, E.M., Bowley, C.M., Goldman, S.M., Harilal, D.O., Neville, C.M., Kronengold, R.T., and Vacanti, J.P. Preserved extracellular matrix components and retained biological activity in decellularized porcine mesothelium. Biomaterials 31, 6934, 2010.
31. Shpaisman, N., Sheihet, L., Bushman, J., Winters, J., and Kohn, J. One-step synthesis of biodegradable curcumin-derived hydrogels as potential soft tissue fillers after breast cancer surgery. Biomacromolecules 13, 2279, 2012.
32. Kim, S.H., Turnbull, J., and Guimond, S. Extracellular matrix and cell signalling: the dynamic cooperation of integrin, proteoglycan and growth factor receptor. J Endocrinol 209, 139, 2011.
33. Eaglstein, W.H., and Falanga, V. Tissue engineering and the development of Apligraf, a human skin equivalent. Clin Ther 19, 894, 1997.
34. Shevchenko, R.V., James, S.L., and James, S.E. A review of tissue-engineered skin bioconstructs available for skin reconstruction. J R Soc Interface 7, 229, 2010.
35. Groeber, F., Holeiter, M., Hampel, M., Hinderer, S., and Schenke-Layland, K. Skin tissue engineering--*in-vivo* and in vitro applications. Adv Drug Deliv Rev 63, 352, 2011.
36. Szabo, I., Wetzel, M.A., and Rogers, T.J. Cell-Density-Regulated Chemotactic Responsiveness of Keratinocytes In Vitro. J Invest Dermatol 117, 1083, 2001.
37. Chen, J., Shi, Z.P., Dong, J., Liao, T.T., Wang, Y.P., Sun, X.P., Yan, Z.J., Qian, X.Q., Cui, Y.G., Xue, Z.G., Fan, G., and Liu, J.Y. Evaluation of x-inactivation status and cytogenetic stability of human dermal fibroblasts after long-term culture. Int J Cell Biol 2010, 289653, 2010.
38. Prunieras, M., Regnier, M., and Woodley, D. Methods for cultivation of keratinocytes with an air-liquid interface. J Invest Dermatol 81, 28s, 1983.
39. Porter, R.M., Lunny, D.P., Ogden, P.H., Morley, S.M., McLean, W.H., Evans, A., Harrison, D.L., Rugg, E.L., and Lane, E.B. K15 expression implies lateral differentiation within stratified epithelial basal cells. Lab Invest 80, 1701, 2000.
40. Murphy, G.F., Flynn, T.C., Rice, R.H., and Pinkus, G.S. Involucrin expression in normal and neoplastic human skin: a marker for keratinocyte differentiation. J Invest Dermatol 82, 453, 1984.
41. Kandárová, H., Hayden, P., Klausner, M., Kubilus, J., Kearney, P., and Sheasgreen, J. In vitro skin irritation testing: Improving the sensitivity of the EpiDerm skin irritation test protocol. Altern Lab Anim 37, 671, 2009.
42. Lee, H.Y., Stieger, M., Yawalkar, N., and Kakeda, M. Cytokines and chemokines in irritant contact dermatitis. Mediators Inflamm 2013, 916497, 2013.
43. Rubin, A.L., Pfahl, D., Speakman, P.T., Davison, P.F., and Schmitt, F.O. Tropocollagen: significance of protease-induced alterations. Science 139, 37, 1963.

44. Ni Annaidh, A., Bruyere, K., Destrade, M., Gilchrist, M.D., and Ottenio, M. Characterization of the anisotropic mechanical properties of excised human skin. J Mech Behav Biomed Mater 5, 139, 2012.
45. Roeder, B.A., Kokini, K., Sturgis, J.E., Robinson, J.P., and Voytik-Harbin, S.L. Tensile Mechanical Properties of Three-Dimensional Type I Collagen Extracellular Matrices With Varied Microstructure. J Biomech Eng 124, 214, 2002.
46. Maas-Szabowski, N., Starker, A., and Fusenig, N.E. Epidermal tissue regeneration and stromal interaction in HaCaT cells is initiated by TGF-alpha. J Cell Sci 116, 2937, 2003.
47. Schäfer-Korting, M., Bock, U., Diembeck, W., Düsing, H., Gamer, A., Haltner-Ukomadu, E., Hoffmann, C., Kaca, M., Kamp, H., Kersen, S., Kietzmann, M., Korting, H., Krächter, H., Lehr, C., Liebsch, M., Mehling, A., C., M.-G., Netzlaff, F., Niedorf, F., Rübbelke, M., Schäfer, U., Schmidt, E., Schreiber, S., Spielmann, H., Vuia, A., and Weimer, M. The use of reconstructed human epidermis for skin absorption testing: Results of the validation study. Altern Lab Anim 36, 161, 2008.
48. Schmook, F., Meingassner, J., and Billich, A. Comparison of human skin or epidermis models with human and animal skin in *in-vitro* percutaneous absorption. Int J Pharm 215, 51, 2001.
49. Mallampati, R., Patlolla, R.R., Agarwal, S., Babu, R.J., Hayden, P., Klausner, M., and Singh, M.S. Evaluation of EpiDerm full thickness-300 (EFT-300) as an in vitro model for skin irritation: studies on aliphatic hydrocarbons. Toxicol In Vitro 24, 669, 2010.
50. Welss, T., Basketter, D.A., and Schroder, K.R. In vitro skin irritation: facts and future. State of the art review of mechanisms and models. Toxicol In Vitro 18, 231, 2004.
51. Black, A.T., Hayden, P.J., Casillas, R.P., Heck, D.E., Gerecke, D.R., Sinko, P.J., Laskin, D.L., and Laskin, J.D. Expression of proliferative and inflammatory markers in a full-thickness human skin equivalent following exposure to the model sulfur mustard vesicant, 2-chloroethyl ethyl sulfide. Toxicol Appl Pharmacol 249, 178, 2010.
52. Cotovio, J., *et al*. The in vitro acute skin irritation of chemicals: otimisation of the EPSKIN prediction model within the framework of the ECVAM validation process. Altern Lab Anim 33, 329, 2005.
53. Ale´pe´ea, N., *et al*. A catch-up validation study on reconstructed human epidermis (SkinEthic RHE) for full replacement of the Draize skin irritation test. Toxicol In Vitro 24, 257, 2010.
54. Katoh, M., et al. Assessment of human epidermal model LabCtye Epi-model for in vitro skin irritation testing according to European Cetre for the Validation of Alternative Methods (ECVAM)-validated protocol. J Toxicol Sci 34, 327, 2009.

5. Chapter 5. Skin tissue engineering based on electrospun polymeric scaffolds

5.1. Introduction

Biodegradable synthetic and natural polymers are attractive biomaterials for developing scaffolds for skin tissue engineering. Biodegradable synthetic polymers such as polycaprolactone[1], polylactic acid[2], and poly(L-lactide)-poly(ethylene glycol)[3] have been utilized in skin tissue engineering. The use of synthetic polymers gives advantages such as high lot-to-lot uniformity, lower cost and is a stable source for raw materials. Scaffolds made from synthetic polymers can be tailored to desired shape, pore size, stiffness and composition to induce cells to grow into specific tissues.[4, 5] However, the major challenges of using scaffolds fabricated from purely synthetic polymers is the lack of cell recognition and lower rate of cell attachment and proliferation.[6]

Natural polymers, including collagen, chitosan, gelatin and hyaluronic acid have been extensively used as dermal substrates in skin tissue engineering.[7-9] These natural polymers are often used as a hydrogel or lyophilized sponge form. Natural polymers are abundant in dermal extracellular matrix (ECM) therefore providing high biocompatibility and promoting cellular recognition. However, disadvantages of using natural polymers are such as high lot-to-lot variability, less tunable biodegradability, and poor mechanical and physical properties.

A new generation of biodegradable polymers based on natural amino acid L-tyrosine, poly(desaminotyrosyl-tyrosine alkyl ester carbonate) were first introduced by Ertel and Kohn[10] and may be potential polymers for skin tissue engineering. The synthesis of this new generation of polymers begin with forming desaminotyrosyl-L-tyrosine alkyl ester (DTR) from reacting L-tyrosine alkyl ester with desaminotyrosine

(DAT) by carbodiimide-mediated reactions, shown in Figure 5.1.[11] When the alkyl group is present as an ethyl group, the monomer, desaminotyrosyl-L-tyrosine ethyl ester (DTE) is formed. The DTE monomers are then chemically reacted with carboxylic acid pendant through indirect synthetic route and generated poly(desaminotyrosyl-tyrosine ethyl ester carbonate) [poly(DTE carbonate), Figure 5.2]. By varying the pendant R group, a family of tyrosine-derived polymers with different physicochemical properties, crystallinity, degradation rates and cell-matrix interactions can be synthesized.

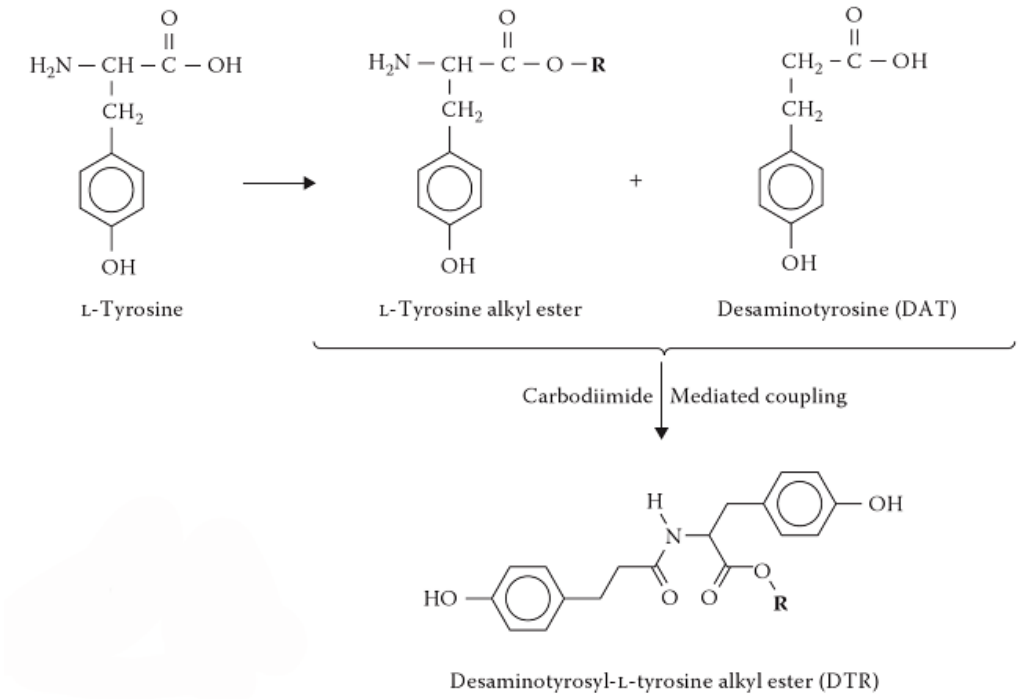

Figure 5.1 Synthetic scheme for the preparation of biodegradable monomer desaminotyrosyl-L tyrosine alkyl ester (DTR) from tyrosine derivatives.

Poly(DTE carbonate) exhibits an average molecular weight of 201 kDa, polydispersity index (Mw/Mn) of 1.8, glass transition temperature around 97°C, and decomposition temperature at 290°C. These polymers have three potentially hydrolysable bonds, which are amide, carbonate and ester bonds. A major advantage of the poly(DTE

carbonate) comes from the absence of acidic metabolites, often produced from other polyester biomaterials [e.g., poly(lactic acid), poly(glycolic acid)] in systemic or local reactions.[12] The hydrolysis of the carbonate groups only yields two alcohol and carbon dioxide. Therefore, poly(DTE carbonate) generates metabolites with little side effects and are desirable biomaterials.

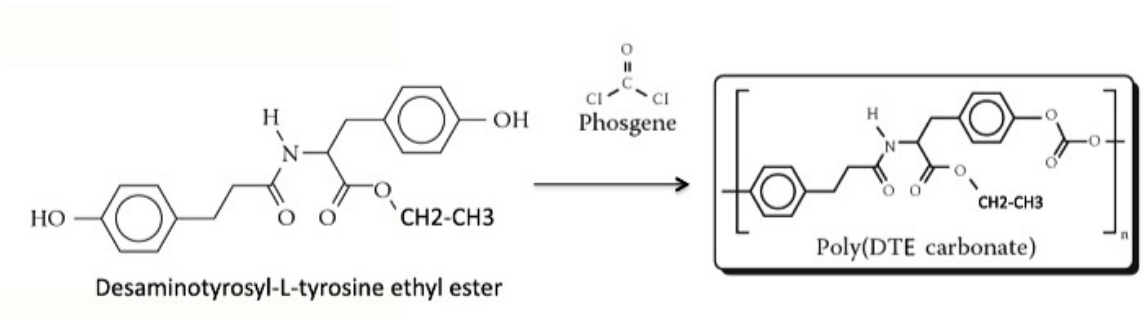

Figure 5.2 Synthesis of poly(desaminotyrosyl-tyrosine ethyl ester carbonate), [poly(DTE carbonate)] from desaminotyrosyl-L tyrosine ethyl ester (DTE) monomers.

Electrospinning is a simple, inexpensive and efficient technique to fabricate micro-to-nanostructure fiber mats. This technique uses a high voltage power supply source that injects polarity to a polymer solution or a polymer melt that is being forced through a needle by a syringe pump (Figure 5.3.). The electrostatic repulsion of the polymer solution overcomes its surface tension and the polymer droplet develops into a cone shape at the edge of needle, recognized as the “Taylor cone” (Figure 5.3.-c).

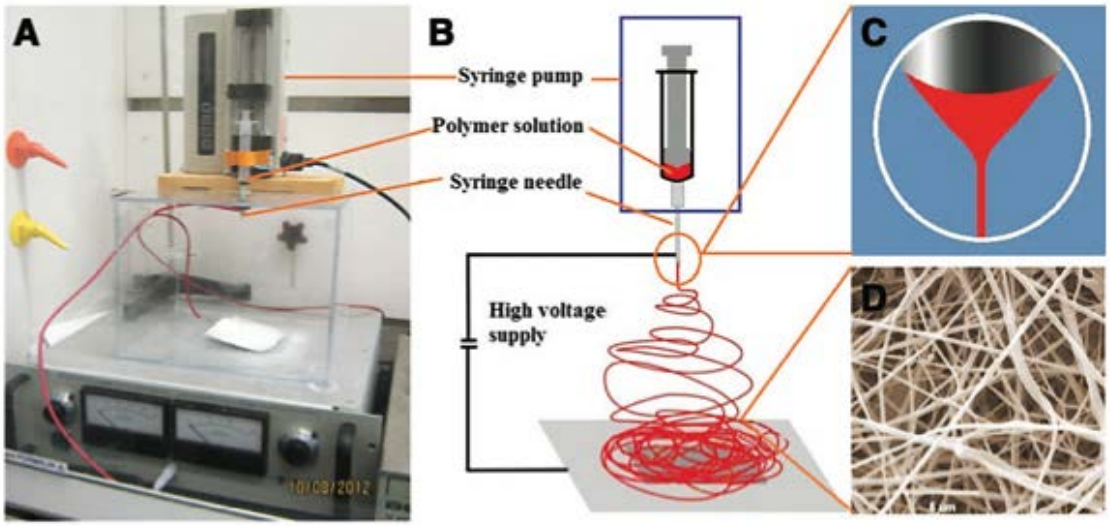

Figure 5.3 Electrospinning process showing (A) electrospinning equipment; (B) a schematic showcasing nanofibers production with a high voltage supply, syringe pump and needle; (C) formation of Taylor cone; (D) SEM morphology of electrospun PCL. Images are reproduced from ref[13].

The formed fiber jets are then collected to a ground collector with opposite charge. The collector can be either a static collector or a rotating mandrel to generate fiber mats with randomly orientated or aligned fibers. The morphology of the resulted electrospun fiber mats mimics the structure of an extracellular matrix. The high surface area to volume ratio of the fiber mats also promotes for better cell growth.[14, 15] In addition, the high porosity also allows the exchange of gases and nutrients to support the long-term growth of cultured tissue. Examples of electrospun fiber mats from various synthetic, natural and blends for skin tissue engineering are indicated in Table 5.1.

Table 5.1 An overview of electrospun polymer fibers for skin tissue engineering applications.

Polymer	Solvent	Fiber diameter	Cell	Ref.
Synthetic				
polycaprolactone	melt	6.8 μm	Human dermal fibroblasts	1
polylactic acid	chloroform/acetone	427 nm	3T3 mouse fibroblasts	2
poly(L-lactide)-poly(ethylene glycol)	chloroform	764-822 nm	Mouse embryo fibroblasts	3
polystyrene	THF	10 μm	Human keratinocyte, fibroblasts, endothelial cells	16
Natural				
Collagen	HFP	100 -1200 nm	Human keratinocytes	17
	HFP	396 μm	Human keratinocytes, Human fibroblasts	18
Chitosan	TFA/DCM	120-200 nm		19
Chitin	HFP	163 nm, 8.3 μm	Human keratinocyte	20
Synthetic + natural blends				
Chitosan-polycaprolactone	DMF/chloroform	423-575 nm	L929 human muscle	5
Collagen-polycaprolactone	HFP	160 μm	Human keratinocytes, Human fibroblasts	4
	HFP	0.2-2.5 μm	Human keratinocytes, Human fibroblasts	6

THF=tetrahydrofuran; HFP=hexafluoroisopropanol; TFA=trifluoroacetic acid; DCM=dichloromethane; DMF=dimethyl formamide

Poly(DTE carbonate) scaffolds made from melt compression were reported to have high tissue compatibility, slow *in-vivo* degradation rate, reduction in swelling, reduction in acid generation, and been utilized in bone regeneration.[21, 22] Although

extensive studies reported its application in bone regeneration, not much effort has been put towards skin tissue engineering. Many of the advantages of poly(DTE carbonate) such as high tissue compatibility and proper mechanical properties, seem to be beneficial to bone as well as to skin tissue. However, no study has fabricated poly(DTE carbonate) into fiber mats and generate reconstructed human skin tissues. Therefore, the aim of this study was to investigate the use of synthetic polymer, poly(DTE carbonate) and electrospin into fiber mats to construct human skin equivalents (HSEs). The polymeric fiber mat based-HSEs can be further applied for *in-vitro* testing (e.g., high-throughput drug screening, lab-on-a-chip).

5.2. Materials and Methods

5.2.1. Materials

Tyrosine-based pseudo-peptide polymer, poly(DTE carbonate) was synthesized and obtained from New Jersey Center for Biomaterials. Retinoic acid (98% crystalline; Alfa Aesar), low molecular weight chitosan (20-300 cps; 75-85% deacetlyated; Sigma Aldrich); glacial acetic acid (Fisher Scientific); Transwell® Permeable supports, 0.4 μm polycarbonate membrane 12 mm insert (Costar, Corning); 37% paraformaldehyde (Sigma Aldrich); Triton-X 100 (Fisher Scientific), tetrahydrofuran (Fisher Scientific), dimethylformamide (Fisher Scientific). HPLC grade water, acetonitrile, and ethanol were purchased from BDH chemicals.

5.2.2. Electrospinning poly(DTE carbonate) polymer

Poly(DTE carbonate) solutions (18% w/v) were prepared by dissolving 635 mg of poly(DTE carbonate) polymer in 3 mL of tetrahydrofuran (THF) and 0.52 mL of dimethylformamide (DMF) in a scintillation vial. Retinoic acid- poly(DTE carbonate) solutions were prepared by mixing 0.05%, 0.5% and 5% (w/w) retinoic acid with 635 mg of poly(DTE carbonate) polymer in 3 mL of THF and 0.52 mL of DMF in a scintillation vial. Chitosan- poly(DTE carbonate) solutions were prepared mixing stock 18% (w/v) poly(DTE carbonate) solutions in 90% acetic acid with 2% (w/v) chitosan in 90% acetic acid. The poly(DTE carbonate):chitosan solutions were mixed at 100%/0%, 75%/25%, 50%/50%, 25%/75%, 0%/100% (v/v) ratios.

The vials were covered with aluminum foil and shaken at 50 rpm at room temperature overnight. The poly(DTE carbonate) solution was then transferred to a 10 mL syringe that was attached to a 23 Gauge needle. The distance of the needle and collecting rotating mandrel was set to be 12.5 cm. The flow rate of the needle pump was set at 1 ml/hr and the electric current was set at 15 kV. The electrospun fibers were collected onto an aluminum foil placed on the rotating mandrel (Reynolds Wrap, heavy duty). The mandrel was able to move horizontally to assist an even distribution of the collected electrospun fibers. The films were transfer to a sterile patch and left in a vacuum chamber for 2 days to allow the organic solvents to completely evaporate. The samples were further storaged at 4°C until experiment use.

5.2.3. Scanning electron microscopy

Microarchitecture of the fiber mats were characterized by scanning electron microscopy. The samples were cut into small pieces and mounted on aluminum studs

with adhesive tapes. The samples were further sputter coated with gold/palladium (30 milli Amps for 120 sections) in a vacuum chamber (SCD004) filled with argon gas at a pressure of 0.05 mbar. The coating of the samples with gold/palladium resulted in electric conductivity of the samples. Scanning electron microscopic images were taken by a scanning electron microscope (SEM, Amray 1830I, acceleration potential of 20 kV) with low and high magnifications.

Fiber and pore size diameters were measured with ImageJ software. 30 measurements of random locations from images were performed and expressed in mean ± standard deviation.

5.2.4. Tensile strength

Mechanical properties were characterized using a mechanical testing instrument (Sintech 5D MTS). Fiber mat specimens were cut into rectangular shapes measuring 1 cm x 6 cm. Thicknesses of samples were measured with a digital micrometer (Mitutoyo IP65) immediately before testing. Samples in dry state were mounted between the two grips of Sintech 5D MTS instrument and the distance of grip-to-grip was measured without use of an extensometer. Test speed was set at 10 mm/min.

Stress-strain curve of the samples were obtained. According to Hooke's Law, the stress is directly proportional to the strain in tension:

$$\frac{F}{A} = E(\frac{L - L_0}{L_0})$$

where stress, is the applied force, F, per unit area of cross section, A, and strain is the increase in length from L_0 (original length) to L (the length under a given tensile stress) to the relative L_0:

$$\text{Strain} = \frac{\Delta L}{L_0} = \frac{L - L_0}{L_0}$$

The proportionality constant is the Young's modulus, *E*, which measures the hardness and stiffness of the samples. Young's modulus was determined based on calculating the slope of linear portion of the stress-strain curve. The analyses were performed in triplicates.

5.2.5. Contact angle

The contact angle of the air-liquid interface describes the surface wettability of the fiber mats. A drop of pure deionized water was placed on the surface of fiber mat. The balance between adhesive forces of the water and fiber mat and the cohesive force within the water determines the contact angle, θ. Contact angle can be expressed according to Young's Equation (Figure 5.4.):

$$\gamma^{sv} = \gamma^{sl} + \gamma^{lv} \cos\theta$$

where θ is the contact angle, γ^{sl} is the solid/liquid interfacial free energy, γ^{sv} is the solid surface free energy and γ^{lv} is the liquid surface free energy. When the solid surface has higher surface energy than the surface tension of the droplet, the contact angle is 0°. When the solid surface has relatively high surface energy, but lower than the liquid's surface tension, the resulting contact angle is between 0° and 90°. When the surface energy is lower than the surface tension of droplet, the wettability is poor, and resulting contact angle is >90°.

The droplets on different fiber mats were imaged with a camera and the contact angles were measured by ImageJ.

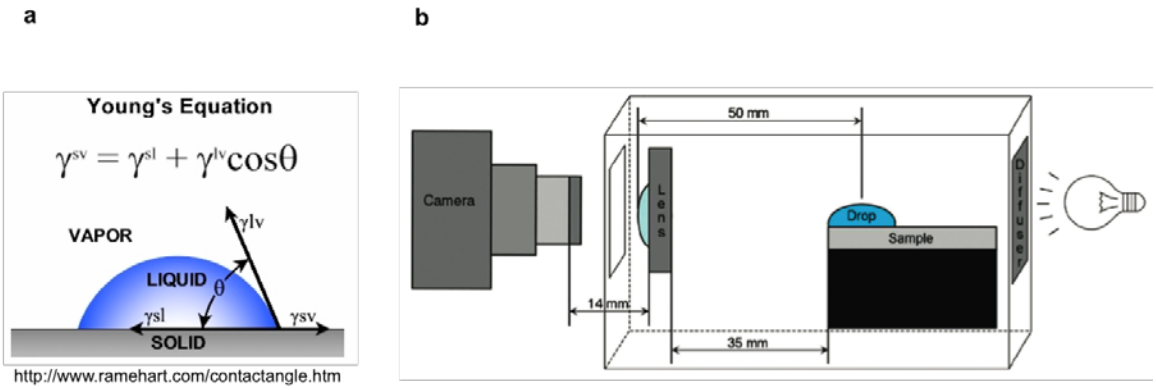

Figure 5.4 Contact angle expressed from Young's Equation (a) and an illustration of a typical experiment set up by using a goniometer (b).

5.2.6. *In-vitro* drug release and HPLC assay

Retinoic acid loaded poly(DTE carbonate) fiber mats were cut into 25 cm^2 squares. The *in-vitro* drug release experiment was performed by transferring the fiber mat into a scintillation vial and filled with 5 mL of PBS that contained 30% ethanol. The samples were further placed on a shaker and incubated in 37°C. 1 mL of the aliquot per samples was collected to an amber vial and fresh media with equal volume was placed back at predetermined time points of 0.5, 1, 1.5, 2.5, 3, 3.5, 4, 6, 8, and 24 hrs. For the control group, total drug content was extracted by adding the 25 cm^2 fiber mat in 2.5 mL of acetonitrile. The samples were filtered with 0.45 μm polyethersulfone syringe filter and drug content was analyzed by high performance liquid chromatography (HPLC; Agilent, 1100 series).

HPLC assay was performed by using reverse phase carbon-18 column (15 cm x 4.6 mm; 5 μm). The standard retinoic acid solutions were prepared in several concentrations in acetonitrile. The mobile phase consisted of 15% of 0.01% trifluroacetic acid (TFA) in water and 85% of acetonitrile. The column temperature was set at 40°C, injection volume at 20 μL and ultra violet detection wavelength at 342 nm. The retinoic acid eluted around 8 minutes. Data was plotted by cumulated amount of release v.s. time and % of release v.s. time. The release profiles were further fitted to zero order, first order, and Higuchi models.

5.2.7. Cell culture

Cryopreserved neonatal human dermal fibroblasts (HDF) (passage one with total cell number > $1x10^6$) were obtained from Life Technologies, NY. HDF were culture with Dulbecco's Modified Eagle Medium (DMEM) media containing 10% (v/v) fetal bovine serum (FBS) and 100 units/mL penicillin, 100 μg/mL streptomycin and 0.25 μg/mL amphotericin B. Cell culture media was changed every other day and the cells were grown in incubators at 37 °C/5% CO_2. For subculture, the cells were treated with 0.025% trypsin-EDTA at room temperature for 3-5 minutes and inhibited trypsin activity by adding FBS contained in DMEM culture media and then centrifuged (1000 rpm/6 min). The remaining pellet was redispersed with DMEM. Passage of no more than five was used in all experiments. The cells were cryopreserved in FBS contained DMEM culture media with 5% dimethyl sulfoxide (DMSO) and storaged in a liquid nitrogen tank.

HaCaT were cultured with DMEM media containing 10% (v/v) FBS and 100 units/mL penicillin, 100 μg/mL streptomycin and 0.25 μg/mL amphotericin B. Cell

culture media was changed every other day. Once the cells have reached 80% confluent, they were trypsinized with 0.25% trypsin under 37°C for 5-10 minutes. The trypsin activity was further inhibited by adding FBS contained DMEM culture media and followed with centrifugation (1000 rpm/6 min). The cell pellets were redispersed in culture media and grown in 37°C incubator with 95% humidity and 5% CO_2.

5.2.8. Cell attachment, proliferation and imaging

Visualization of cell attachment and proliferation on fiber mats were performed by seeding HDF or HaCaT at $5x10^3$ cells/cm^2 or $5x10^4$ cells/cm^2 densities on fiber mats. At day 1, 4 and 7, samples were fixed with 3.7% paraformaldehyde in PBS for 10 minutes at room temperature. Then the samples were washed with PBS and treated with 0.1% Triton-X 100 in PBS for 3 minutes. The samples were washed again with PBS and stained with fluorescent phallotoxins actin stain, Alexa Fluor® 488 (Life Technologies, NY) and nuclei dye, Hoechst 33258 (AnaSpec Inc, CA) at room temperature for 20 minutes. The samples were further imaged with either epifluorescent microscope (Zeiss) or confocal microscope.

Cell proliferation on fiber mats was quantified by measuring metabolic activity by AlamarBlue® assay. The poly(DTE carbonate) fiber mats were cut into round disk with diameter of 12mm. HDF and HaCaT with cell densities of $5x10^4$ cells/cm^2 were seeded on fiber mat, type 1 collagen gel and TCPS contained in a 48 well plate. The quantification of proliferation by AlamarBlue® assay is via the cells reducing metabolic activities, reducing the blue/non-fluorescent AlamarBlue® dye, resazurin, into a pink/fluorescent product, resorufin. The intensity of the fluorescence is proportional to

the number of living cells at a certain cell density range. AlamarBlue® assays were performed at day 1, 4, 7, 11, 14, 18 and 21 to measure the cellular metabolic activity. Briefly, 500 µL of DMEM with 10% of AlamarBlue® reagent were added to the cells and incubated at 37°C for 3 hours. Fluorescence intensity (FI) was then measured at excitation 560 nm/emission 590 nm. Each experimental group was done in triplicates and two independent experiments were performed. After the measurements, the cells were washed with PBS for three times and culture back to the incubators with FBS contained DMEM culture media.

5.2.9. Constructing polymeric fiber mat based-HSEs

The preparation of poly(DTE carbonate)-HSEs is shown in Figure 5.5. Poly(DTE carbonate) fiber mats were cut into 12 mm diameter circle disks with biopsy punches. The fiber mats were then placed on Transwell® inserts (polycarbonate; 0.4 µm) in a 12-well plate. Human dermal fibroblasts were seeded to the fiber mats at $5x10^4$ cells/cm^2 density. The following day, the HDF seeded fiber mats were flipped over and HaCaT with density of $5x10^4$ cells/cm^2 were seeded to the opposite site. The HSEs were immerged in DMEM media containing 10% (v/v) FBS and 100 units/mL penicillin, 100 µg/mL streptomycin and 0.25 µg/mL amphotericin B at 37°C/5%CO_2/95% relative humidity for 7 days. Then the HSEs were fed with differentiation media, which contained 3:1 (v/v) of DMEM: EpiLife® with bovine pituitary extracts (Life Technologies) and final concentrations of 25 µM palmitic acid (Sigma Aldrich), 15 µM linoleic acid (Sigma Aldrich), 25 µM oleic acid (Sigma Aldrich), 7 µM arachidonic acid (Sigma Aldrich), 100 µg/mL ascorbic acid (Sigma Aldrich), 10 µM carnitine (Spectrum),

300 μM clofibrate (Sigma Aldrich), 100 μM bovine serum albumin (Sigma Aldrich), and 2 mM calcium chloride (Sigma Aldrich). The relative humidity of incubator was reduced to 75% to stimulate keratinocyte differentiation. The medium was changed every two days and the constructs were cultured for another 14 days before harvest.

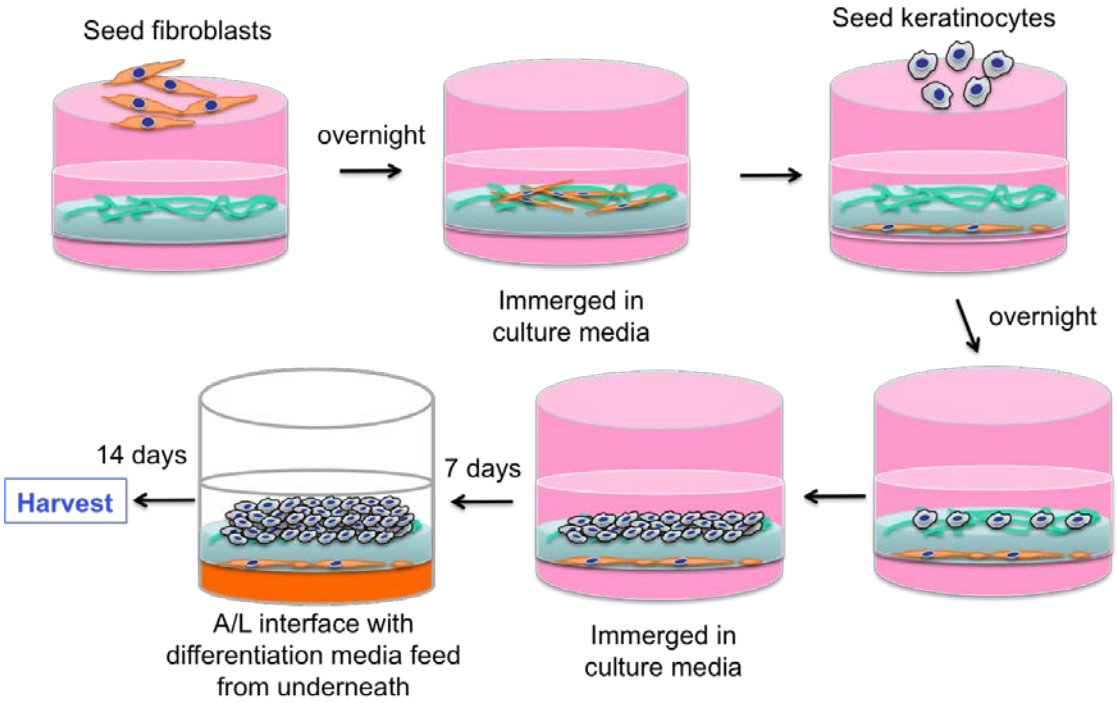

Figure 5.5 Schematic representation of the preparation of poly(DTE carbonate)-HSEs.

5.2.10. Histology and immunohistochemistry

Cryopreserved human cadaver skins (African American/male) were obtained from skin bank (NY Firefighters, New York NY) and were used as controls. The skins were harvested by dermatome and thicknesses were around 500-1500 μm. The skins were stored at -80°C until further use.

Human cadaver skins and poly(DTE carbonate)-HSEs were fixed with 10% buffered formalin (Sigma Aldrich) at room temperature overnight, dehydrated with a gradient of ethanol (50%, 70%, 80%, 100%) and xylene following routine procedures, and embedded into paraffin blocks. The samples were cut into 8 μm thick, deparaffinized with xylene, rehydrated in a gradient of ethanol and stained for standard haematoxylin & eosin (H&E) or immunohistochemical staining. For immunohistochemical staining, sectioned samples were treated with 0.3% hydrogen peroxide for 10 minutes to block the endogenous peroxide activity. Then the samples were heat treated in 10 mM citrate buffer (Sigma Aldrich), pH 6.0 at 95-100 °C for 30 minutes for antigen retrieval and treated with protein block reagent (Abcam, mouse specific horseradish peroxidase/3'3'-diaminobenzidine tetrahydrochloride (HRP/DAB) detection kit) overnight at 4°C. On the following day, the samples were incubated with 1:1500 diluted mouse monoclonal primary antibody anti-involucrin (Abcam) and 1:50 anti-keratin 15 (Abcam) at room temperature for an hour. Then staining procedure was followed according to the manufacture protocol of mouse specific HRP/DAB detection kit, and haematoxylin counterstaining was performed to label the nuclei.

5.3. Results and Discussion

5.3.1. Characterization of poly(DTE carbonate) scaffolds

Fiber diameter, pore size, scaffold thickness

Poly(DTE carbonate) solutions, 18% (w/v) were able to electrospun into fiber porous mats that appeared as a flexible thin sheet. The physical appearance of the fiber mat was a homogenous white colored sheet. The average thickness of fiber mats was 47.0

± 10.0 μm. Scanning electron microscopy showed the formation of non-woven fibers structures from the mats (Figure 5.6.). The fiber diameter and pore size were shown to be 2.4 ± 1.0 μm and 37.0 ± 16.9 μm respectively (Table 5.2.).

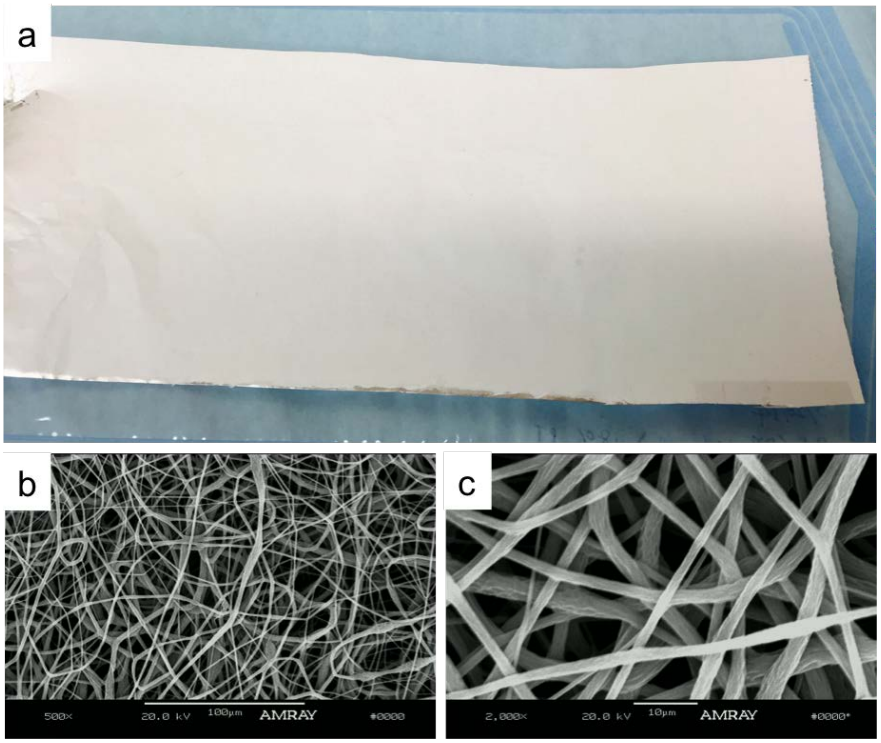

Figure 5.6 Physical appearance of poly(DTE carbonate) fiber mat (a) and non-woven fibrous structures under scanning electron microscopy, (b) (c).

Table 5.2 Physical characteristics of electrospun 18% poly(DTE carbonate) fiber mats

Fiber diameter (μm)	2.4 ± 1.0
Pore size (μm)	37.0 ± 16.9
Scaffold thickness (μm)	47.0 ± 10.0

Mechanical properties

Stress-strain curve of 18% poly(DTE carbonate) fiber mats in dry state is shown in Figure 5.7. The fiber mat exhibits Young's modulus of 48.4 ± 9.1 MPa, ultimate tensile strength of 1.8 ± 0.8 MPa and strain at break at 8 ± 6.3 % (Table 5.3).

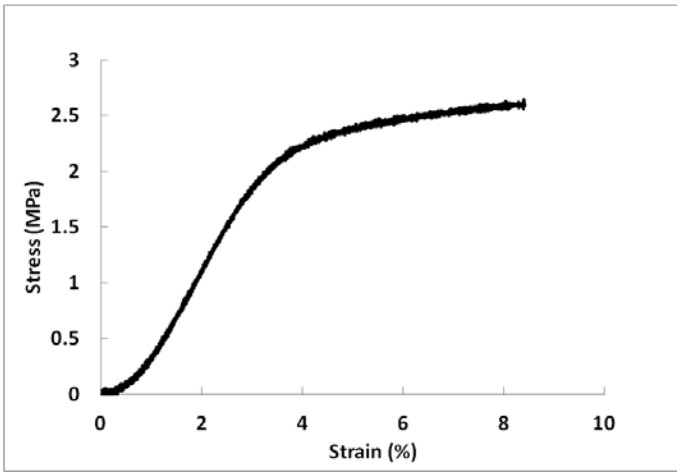

Figure 5.7 Stress-strain curve and mechanical properties of 18% poly(DTE carbonate) fiber mats in dry state. N=3.

Table 5.3 Mechanical properties of 18% poly(DTE carbonate) mats in dry state

Modulus (MPa)	48.4 ± 9.1
Tensile strength (MPa)	1.8 ± 0.8
Strain at break (%)	8 ± 6.3

5.3.2. Cellular attachment on poly(DTE carbonate) scaffolds

Adhesion of epithelial cells to extracellular matrix is critical for cell survival. The adhesion-dependent survival of epithelial cells is mediated by extracellular signal regulated kinase (ERK) family of mitogen-activated protein kinases (MAP kinases).[23] The activation of ERK by integrin-mediated signals activates the transcription genes that promote cell survival. Failure for adequate cell adhesion leads to apoptosis known as "anoikis". The cellular adhesion of skin cells, HDF and HaCaT were investigated by seeding HDF and HaCaT with cell density of $5x10^4$ cells/cm^2 on poly(DTE carbonate) fiber mat, bovine type 1 collagen gel and TCPS. The attachment % was calculated based on TCPS as 100% attachment. The results of HDF and HaCaT attachment at 24 hours are

shown in Figure 5.8. For HDF, the attachment was significantly higher on poly(DTE carbonate) fiber mat than on type 1 collagen gel. However, for HaCaT, the attachment on poly(DTE carbonate) fiber mat were similar to those of type 1 collagen gel. Both type of cells have attachment larger than 75% on poly(DTE carbonate), indicated the excellent adhesion of skin cells on the poly(DTE carbonate) fiber mat.

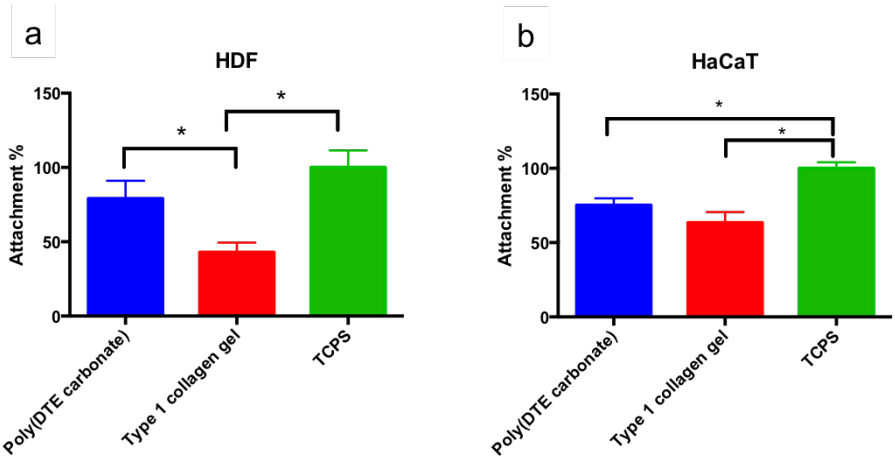

Figure 5.8 Cellular attachment of HDF (a) and HaCaT (b) on poly(DTE carbonate) fiber mat, type 1 collagen gel and TCPS after 24 hours. * Indicated statistically significant difference ($p<0.05$; ANOVA/post -hoc Dunnette).

5.3.3. Cell proliferation on poly(DTE carbonate) scaffolds

Cellular proliferation of HDF and HaCaT were evaluated by seeding monolayer of cells on the surface of poly(DTE carbonate) mats (Figure 5.9.). The cell numbers from each group were interpolated based on the linear relationship between metabolic activities and known cell numbers determined by AlamarBlue® assay. Type 1 collagen gel and TCPS were used as control groups. For HDF, the cell numbers on poly(DTE carbonate) mats were similar to those on TCPS and significantly higher than type 1 collagen gel over 21 days. For HaCaT, the increased of cell numbers on poly(DTE carbonate) mats were similar as TCPS from day 1 to day 7 but significantly increased

after day 11 for poly(DTE carbonate) mats. The HaCaT had higher cell numbers on poly(DTE carbonate) mats than type 1 collagen gel over 21 days. Poly(DTE carbonate) mats exhibit excellent cell attachment and proliferation for both HDF and HaCaT, indicating biocompatibility with skin cells.

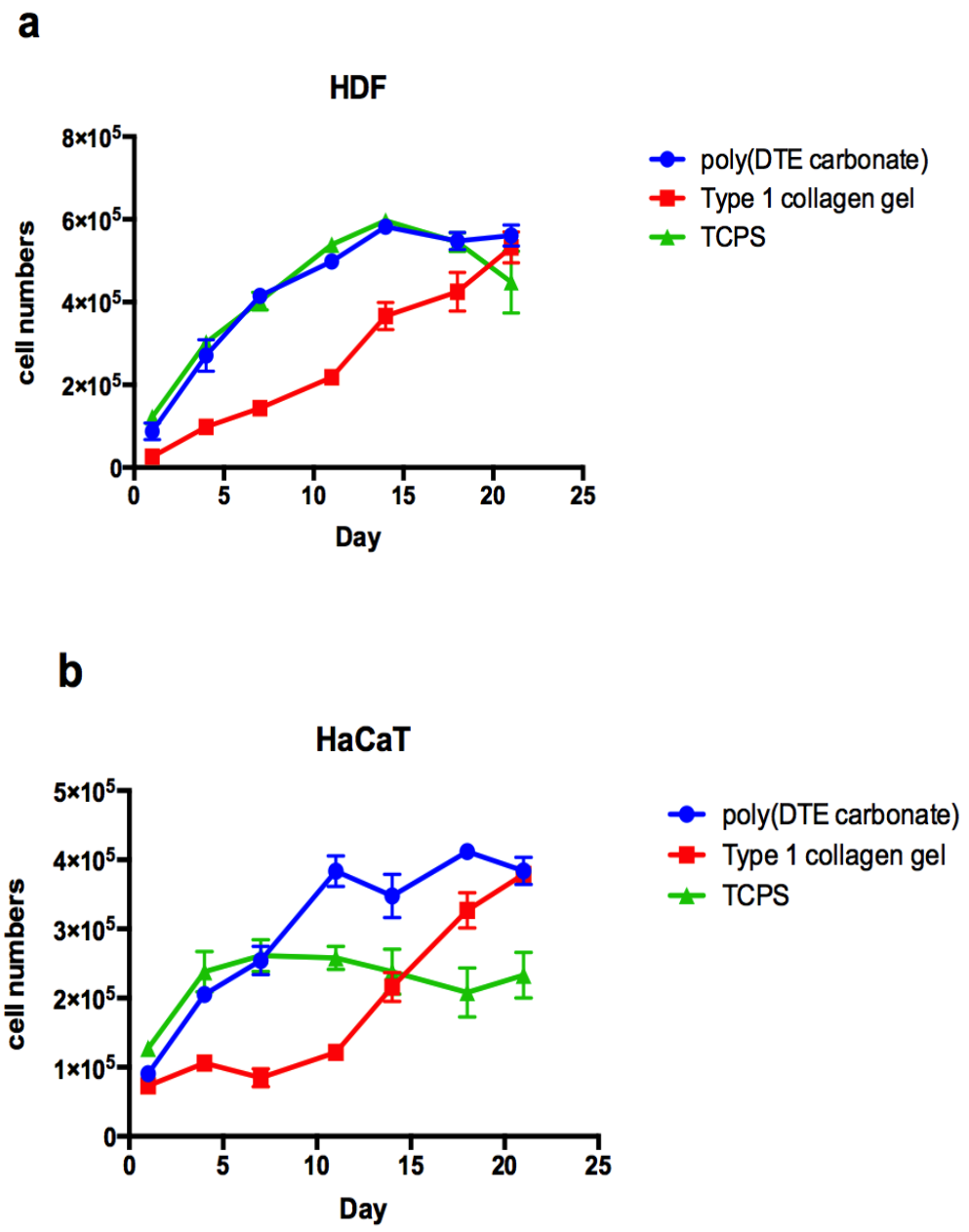

Figure 5.9 Cell viability of HDF (a) and HaCaT (b) on poly(DTE carbonate) mat, type 1 collagen gel and tissue culture polystyrene (TCPS) over 21 days.

The morphology of proliferated HDF and HaCaT on poly(DTE carbonate) mats were further examined by confocal microscopy (Figure 5.10. and Figure 5.11.). Both types of cells showed homogenously spread on the fiber mats and proliferated from day 1 to day 7. HDF exhibited signature spindle shape morphology with random orientation at day 1 and were packed alignment at an angle at day 7 (Figure 5.10).

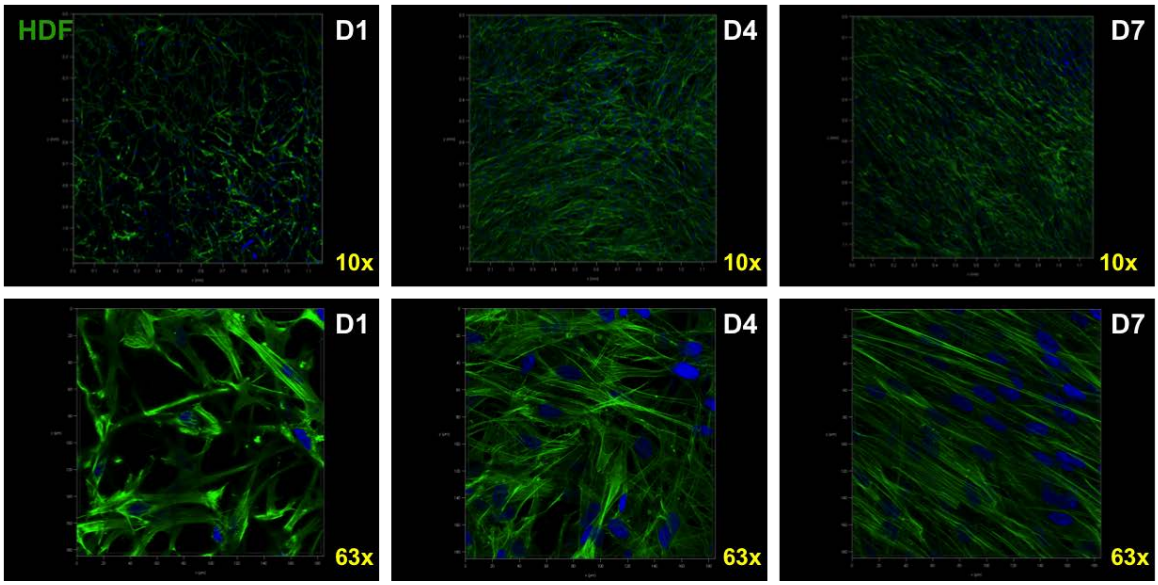

Figure 5.10 Three dimensional confocal images of HDF on poly(DTE carbonate) scaffold at day 1, 4 and 7 (D1, D4, D7). Samples were stained with F-actin (Green; Alexa Fluor 488) and nuclei dye (Blue; Hoechst). Images were taken at 10x and 63x magnifications.

Similarly, HaCaT exhibited homogenous spreading and proliferated from day 1 to day 4. The morphology of HaCaT was in its typical polygonal and cobblestone shape. On day 7, early differentiation with the loss of nuclei, increased in cell size and desquamation of the HaCaT were detected (Figure 5.11).[24]

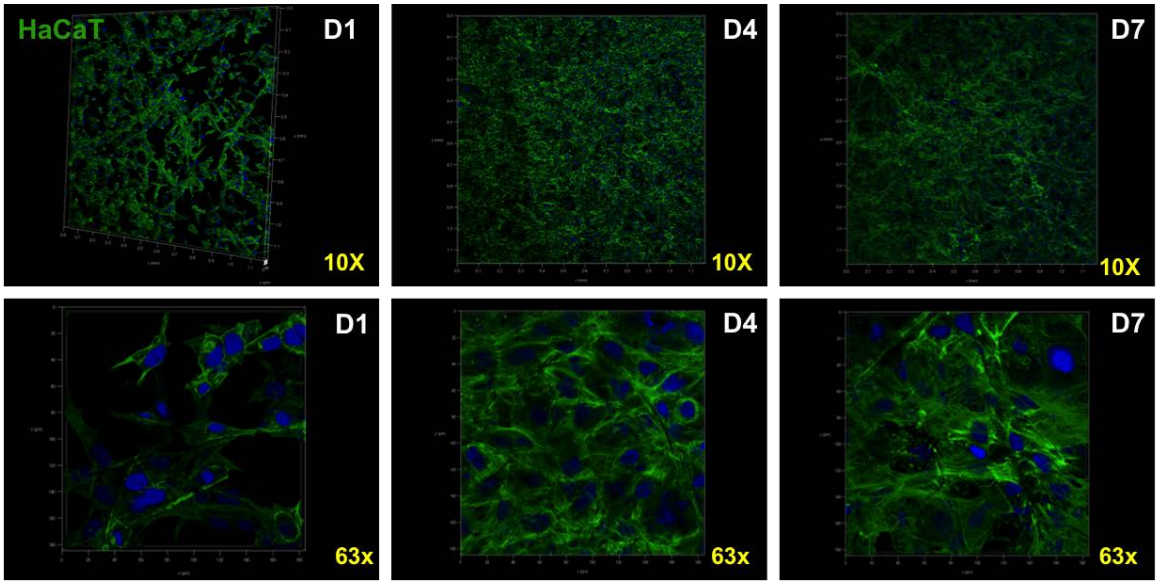

Figure 5.11 Three dimensional confocal images of HaCaT on poly(DTE carbonate) scaffold at day 1, 4 and 7 (D1, D4, D7). Samples were stained with F-actin (Green; Alexa Fluor 488) and nuclei dye (Blue; Hoechst). Images were taken at 10x and 63x magnifications.

5.3.4. Retinoic acid loaded poly(DTE carbonate) scaffolds

All-trans retinoic acid (RA), is a natural metabolite of retinol (Vitamin A) which is converted in human body by enzymes. Retinol is metabolized to retinal through dehydrogenase activity and retinal is further metabolized into retinoic acid by retinal dehydrogenase (Figure 5.12.). Retinoic acid and retinoid families (i.e., analogs of vitamin A) are important regulators of skin cell proliferation and differentiation. All-trans retinoic acid activates ligand-dependent transcription factors, retinoic acid receptors (i.e., RARα, β, γ), which lead to regulation of epithelial cell growth and differentiation.[25] One of the objective of this study was to investigate whether incorporating RA to the poly(DTE carbonate) scaffolds were able to regulate HaCaT differentiation of HSEs.

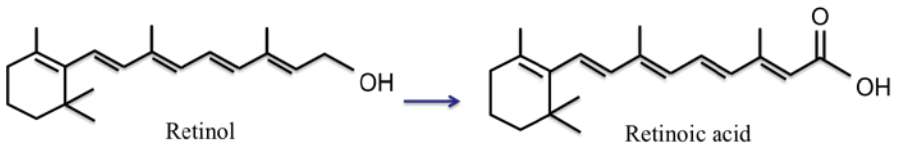

Figure 5.12 Retinoic acid is a natural derivative of retinol. Retinol is converted to retinoic acid by retinol dehydrogenase and retinal dehydrogenase.

Retinoic acid is a small molecule (M.W. = 300 g/mol), weak acid with pka=4.2 and exhibits highly lipophilic properties (logP=6.3). Retinoic acid was mixed with poly(DTE carbonate) in THF/DMF solvent at 0.05%, 0.5%, and 5% (w/w) concentrations and the RA-polymer solutions were electrospun into fiber mats. The physical appearance of RA loaded electrospun poly(DTE carbonate) fiber mats are shown in Figure 5.13. As the weight percentage of RA loading increased, a more yellow color of the film was observed.

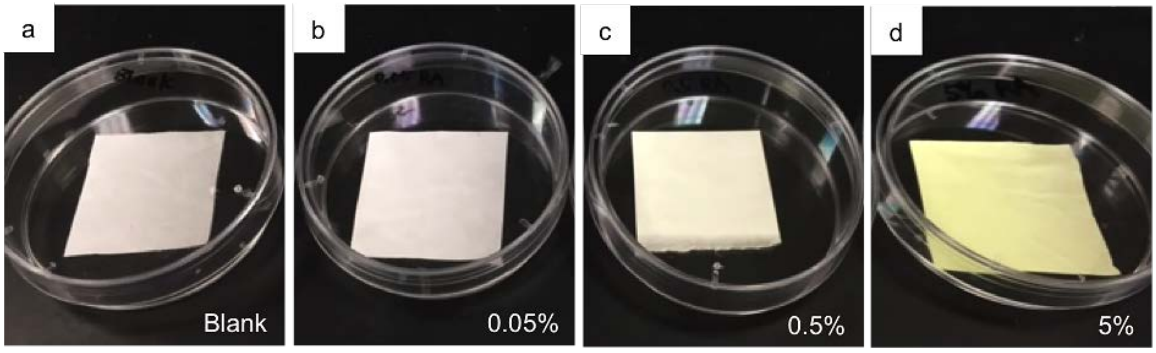

Figure 5.13 Physical appearance of 25 cm^2 blank and retinoic acid loaded poly(DTE carbonate) fiber mats. Retinoic acid/poly(DTE carbonate) was loaded at concentration of 0.05% (w/w) (b), 0.5% (w/w) (c) and 5% (w/w) (d).

The electron scanning microscopy showed the mats were composed with several non-woven layers of fibers and without presence of beading (Figure 5.14). The average fiber diameters for 0.05%, 0.5% and 5% RA loaded films were 2 ± 0.4, 1.8 ± 0.6, and 1.8

± 0.5 μm, respectively. The average pore size of the 0.05%, 0.5% and 5% RA loaded films were 18 ± 9.3, 20 ± 8.6 and 23 ± 8.7 μm, respectively (Table 5.4). The average thicknesses of the 0.05%, 0.5% and 5% RA loaded films were 77 ± 7.2, 78 ± 10.4 and 77 ± 3.6 μm, respectively (Table 5.4). Overall, the fiber diameter, pore size and film thickness were similar to the blank poly(DTE carbonate) fiber mat and the additional loading of the RA did not have an effect on these parameters.

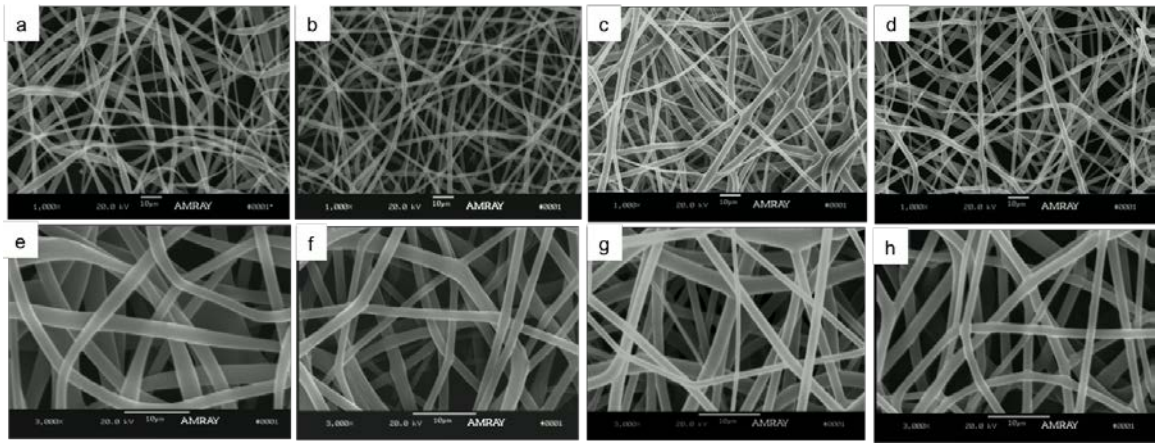

Figure 5.14 Scanning electron microscopic images of blank and retinoic acid loaded poly(DTE carbonate) fiber mats. Retinoic acid was loaded at concentration of 0.05% (w/w) (b, f), 0.5% (w/w) (c, g) and 5% (w/w) (d, h). (a), (b), (c) and (d) were imaged at 1,000x magnification and (e), (f), (g), (h) 3,000x magnification.

Table 5.4 Physical characteristics of RA-loaded poly(DTE carbonate) fiber mats

Poly(DTE carbonate) fiber mats	Fiber diameter (μm)	Pore size (μm)	Scaffold thickness (μm)
Blank mat	2 ± 0.6	18 ± 8.6	65 ± 8.6
0.05% RA-mat	2 ± 0.4	18 ± 9.3	77 ± 7.2
0.5% RA-mat	1.8 ± 0.6	20 ± 8.6	78 ± 10.4
5% RA-mat	1.8 ± 0.5	23 ± 8.7	77 ± 3.6

The release profile of RA from RA loaded poly(DTE carbonate) fiber mats were shown in Figure 5.15. The drug release experiments were done by cutting the films into

25 cm^2 and transferred to a scintillation vial with media at 37°C with a shaker. Since RA has low solubility in PBS, 30% of ethanol was added to ensure sink conditions were established. At predetermined time points, 1 mL of sample was collected and an equal volume of fresh media was added. The samples were further filtered and drug concentrations were analyzed by high performance liquid chromatography (HPLC) assay.

For fiber mats with 0.5% and 5% RA loading, the drug release kinetic exhibited controlled release and 100% of the drug was released at 8 hours. The kinetics of drug release was mathematically determined by fitting the generated profile using Microsoft Excel. Data fitting into zero order, first order and Higuchi model were assessed. The drug release data fitting indicated the Higuchi model (R^2 of 0.5% film= 0.96, 5% film=0.97) and zero order (R^2 of 0.5% film= 0.94, 5% film=0.93) can best describe the release kinetics with correlation coefficient (R^2) closest to 1.

Higuchi model best described the drug release from a porous matrix system where matrix swelling and dissolution are negligible. [26] The RA was released as a diffusion process with a dependence of the square root of time. The fit of the RA release profile to zero order model suggested the RA release from poly(DTE carbonate) fiber mats was at constant rate and was independent of RA concentrations at time points.

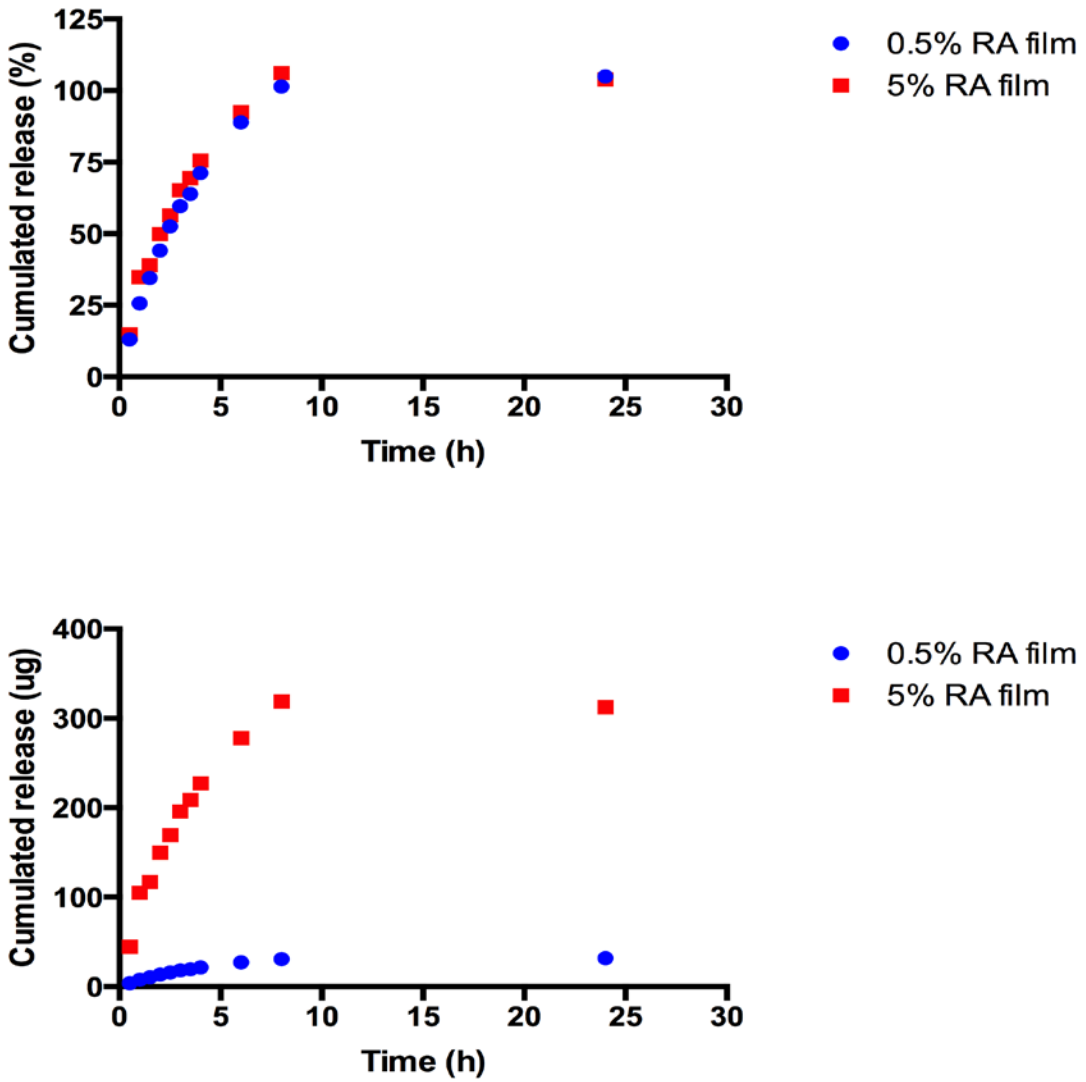

Figure 5.15 Drug release of retinoic acid from electrospun RA loaded poly(DTE carbonate) fiber mats during 24 hours.

5.3.5. Cell proliferation on RA-poly(DTE carbonate) scaffolds

In order to investigate the cell-matrix interaction between skin cells and RA-poly(DTE carbonate) scaffolds, human keratinocyte cell line, $5x10^3/cm^2$ HaCaT were seeded onto the RA-poly(DTE carbonate) scaffolds and images were taken at day 1 and day 4 post-seeding (Figure 5.16). The cells attached and proliferated on blank scaffolds

and control group TCPS. The morphology of HaCaT was round in shape compared to TCPS group. Decreased cell density of HaCaT was found with increased RA concentration. HaCaT proliferated and began to differentiate on TCPS at day 4 whereas the cell density decreased in the RA-poly(DTE carbonate) scaffolds. Incorporating RA reduced the cell attachment and proliferation of HaCaT. A possible explanation of this result could be the effect of surface charge from the fiber mats influencing cell attachment behavior. [27] Lee et al. suggested that positively charges on polyethylene surface grafted with amine groups improved Chinese hamster ovary cell attachment.[28] In another study, Bush et al.[29] suggested the influence of keratinocyte attachment by different functional groups. The authors found that fibronectin with NH_2 and CH_3 terminated surface correlated with increased human keratinocyte attachment whereas fibronectin with COOH and OH terminated surface had lower adhesion compared to TCPS. Since retinoic acid exhibits carboxylic acid functional group, it may explain for the decrease of keratinocyte attachment.

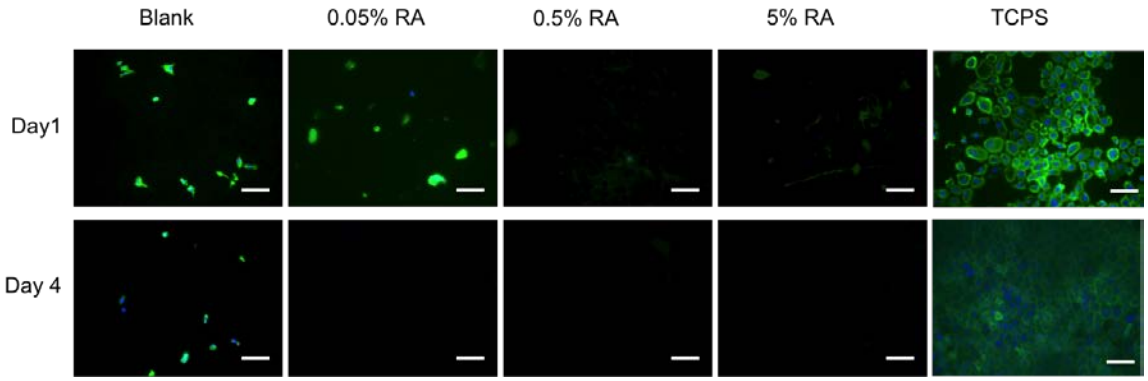

Figure 5.16 Human keratinocyte cell line, $5x10^3/cm^2$ HaCaT on RA-poly(DTE carbonate) and blank poly(DTE carbonate) scaffolds. Samples were fixed with 3.7% formaldehyde and HaCaT were stained with F-actin (Green; Alexa Fluor 488) and nuclei (Blue; Hoechst) markers. Fluorescence images were taken at 200X magnifications by epifluorescence microscope. Bar indicates 100 μm.

5.3.6. Characterization of chitosan-poly(DTE carbonate) scaffolds

Chitosan, a β-(1-4) linked D-glucosamine and N-acetyl-D-glucosamine is a natural polysaccharide derived from chitin. Chitosan has been widely used as a biomaterial based on its nontoxic, biocompatible, biodegradable properties. In the natural ECM, glycosaminoglycans have important roles in intertwining with the fibrous structure of the collagen fibers to obtain mechanical stability as well as interacting with cell behavior. Therefore, it may be promising to incorporate chitosan with poly(DTE carbonate) to create more biomimetic scaffolds for skin cells.

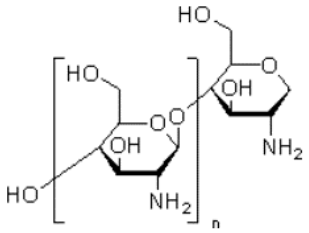

Figure 5.17 The molecular structure of chitosan, β-(1-4) linked D-glucosamine.

Since both chitosan and poly(DTE carbonate) are soluble in acid, two polymers were mixed into acetic acid (90%, v/v) solutions and electrospun into fiber mats. Figure 5.18. shows the scanning electron microscopy of chitosan- poly(DTE carbonate) scaffolds that were mixed at different polymer ratios. Fiber mats with 50%, 75% and 100% poly(DTE carbonate) were able to form into scaffolds with fibers while below 50% poly(DTE carbonate), fibers were not able to form. Moreover, beading morphology was observed at 25% poly(DTE carbonate)/75% chitosan (Figure 5.18 g,h) and 100% chitosan mat (Figure 5.18 i,j). The formation of the beads can be driven by several factors, including surface tension, viscoelastic properties and net charge density.[30] In this case,

the decreased of polymer concentration and viscosity may be accounted for the formation of beading. The lower concentration and viscosity of the polymer solutions, the more likely for the beadings to be formed.[31]

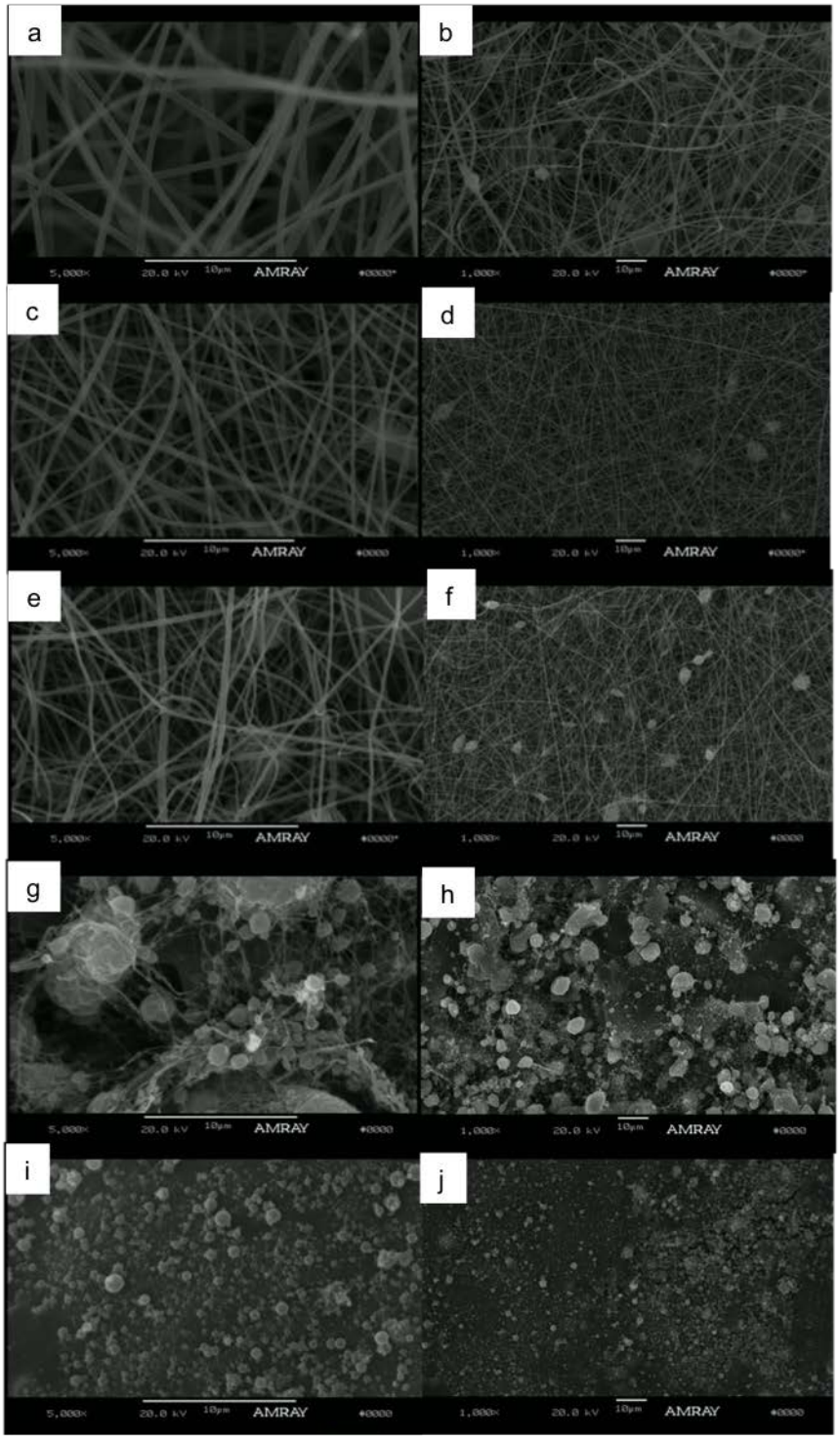

Figure 5.18 Electrospun chitosan-poly(DTE carbonate) fiber mats from using acetic acid as solvent. 100% poly(DTE carbonate) (a, b); 75% poly(DTE carbonate) + 25% chitosan (c,d); 50% poly(DTE carbonate) + 50% chitosan (e,f); 25% poly(DTE carbonate) + 75% chitosan (g,h); 100% chitosan (i,j). Images (a) (c) (e) (g) (i) were taken at 5,000X where (b) (d) (f) (h) (j) were taken at 1,000 X magnification.

Hydrophobicity of the electrospun chitosan-poly(DTE carbonate) fiber mats were further characterized by contact angle (Figure 5.19). The contact angle measured the angle between solid-liquid interactions at interface and indicated the wettability of the mat. The higher the angle indicated the more hydrophobic of the mat. The contact angle showed the highest for 75% poly(DTE carbonate) + 25% chitosan (θ=110°) and lowest for 25% poly(DTE carbonate) + 75% chitosan (θ=25°).

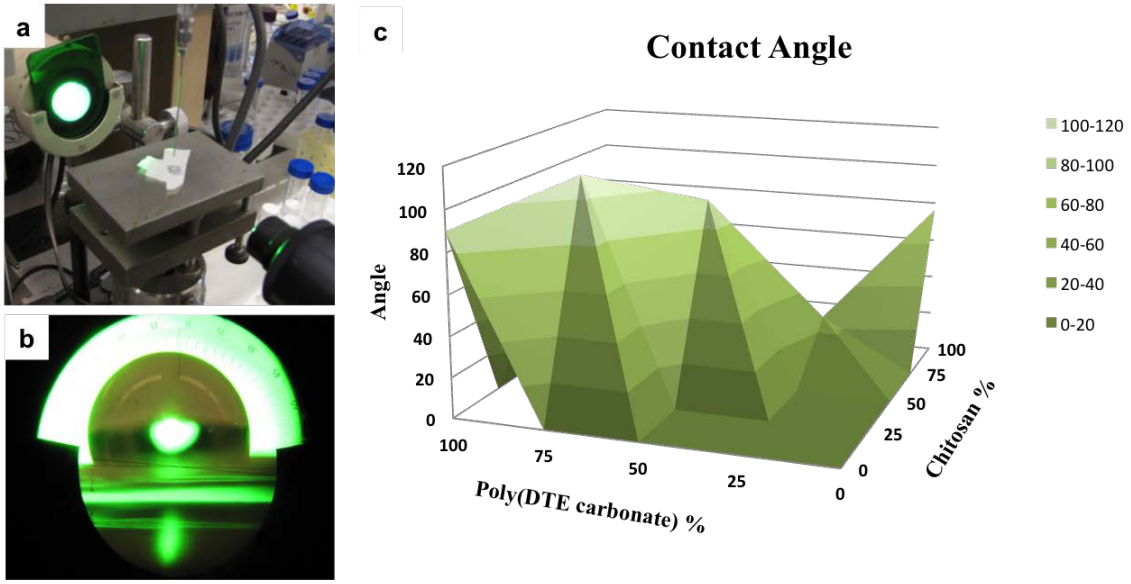

Figure 5.19 Contact angle goniometer instrument (a), image of water droplet on a poly(DTE carbonate) fiber mat (b) and resulting contact angle of electrospun chitosan-poly(DTE carbonate) fiber mats.

5.3.7. Cell proliferation on chitosan-poly(DTE carbonate) scaffolds

In order to investigate cell matrix interaction of keratinocytes and fiber mats, human keratinocyte cell line (HaCaT) was seeded on to chitosan-poly(DTE carbonate) scaffolds. Proliferation of cells was measured on day 1, 4, and 7 by metabolic activity from AlamarBlue® assay (Figure 5.20). The chitosan- poly(DTE carbonate) scaffolds

with different chitosan/poly(DTE carbonate) blend ratios showed decreased proliferation of HaCaT and the 100% poly(DTE carbonate) electrospun from THF/DMF solvent remained the preferable proliferation. The fluorescent images of HaCaT-Lag on scaffolds post 7 days seeding confirmed this trend.

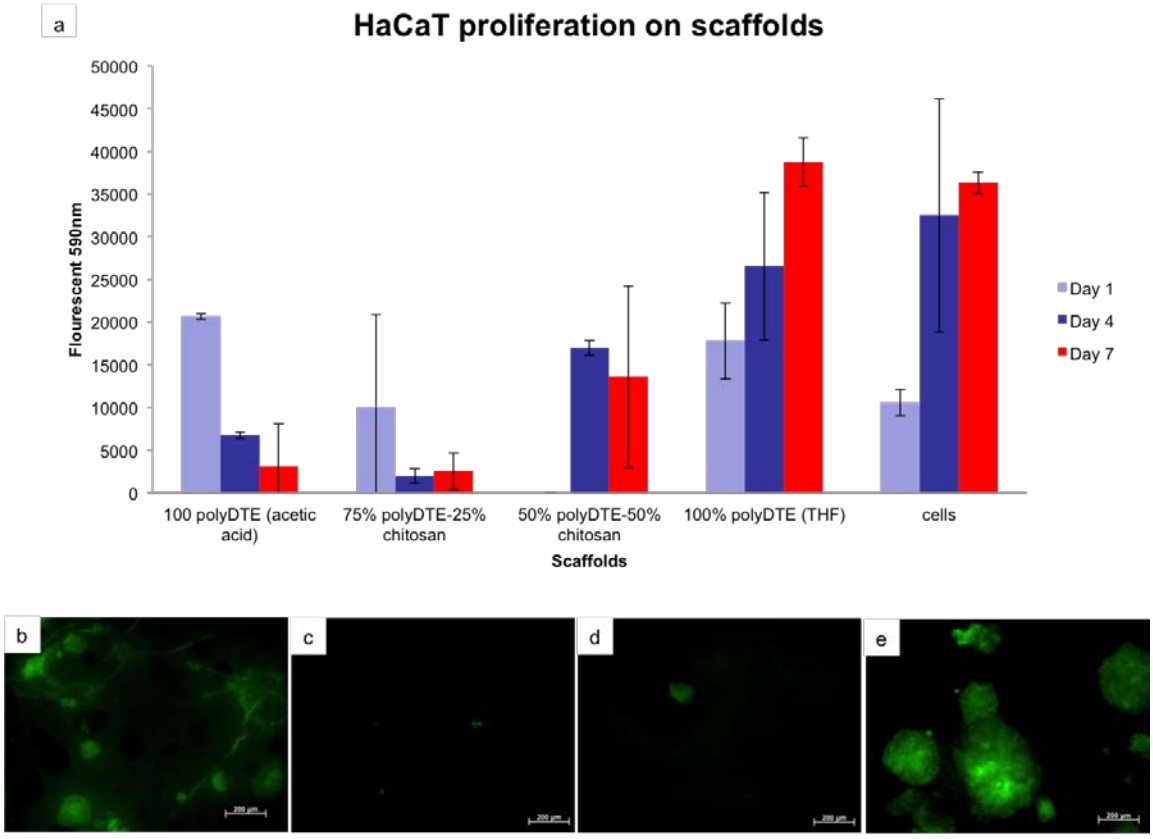

Figure 5.20 Cell metabolic activity of HaCaT-Lag on poly(DTE carbonate) scaffolds on day 1,4, and 7, (a). Fluorescence images of HaCaT-Lag on fiber mats post 7 days seeding: (b) 50% poly(DTE carbonate) + 50% chitosan, (c) 75% poly(DTE carbonate) + 25% chitosan, (d) 100% poly(DTE carbonate) from acetic acid, (e) 100% poly(DTE carbonate) from THF/DMF. Bar indicates 200 μm.

5.3.8. Poly(DTE carbonate) based HSEs

Based on the above results, electrospun poly(DTE carbonate) in THF/DMF solvent remained the best for skin cell attachment and proliferation. The poly(DTE carbonate) fiber mats were further co-cultured with HDF and HaCaT to establish HSEs.

Characterization of the poly(DTE carbonate) based HSEs were performed by histology cross-section H&E staining and immunohistochemical staining of keratinocyte differentiation marker, involucrin and keratinocyte proliferation marker, keratin 15 (Figure 5.21). Three week cultured poly(DTE carbonate) based HSEs exhibited epidermis with multiple layers and a thickness around 44.7 ± 15 μm (cadaver human skin epidermis = 110.8 ± 17μm). The epidermal organization and morphology of poly(DTE carbonate) based HSEs were slightly irregular compared to cadaver human skin, where layer of *stratum corneum* was absent on human skin. However, epidermal layers such as *stratum basale*, *stratum spinosum,* and *stratum granulosum* were present on the of poly(DTE carbonate) based HSEs (Figure 5.21- b). Involucrin is expressed by keratinocytes (above basal layers) that have committed to terminal differentiation (Figure 5.21-c). Keratinocyte differentiated marker, involucrin was detected in all of the epidermal layers of poly(DTE carbonate) based HSEs (Figure 5.21- d). However, keratinocyte proliferation marker, keratin 15, which is normally expressed at basal layer was not detected on the epidermis of poly(DTE carbonate) based HSEs (Figure 5.21- f). Overall, poly(DTE carbonate)-HSEs resulted in partially differentiated epidermis and absence of proliferation marker (keratin 15). Hoever, the poly(DTE carbonate)-HSEs exhibited *stratum spinosum,* and *stratum granulosum* layers that were similar to those of human skin.

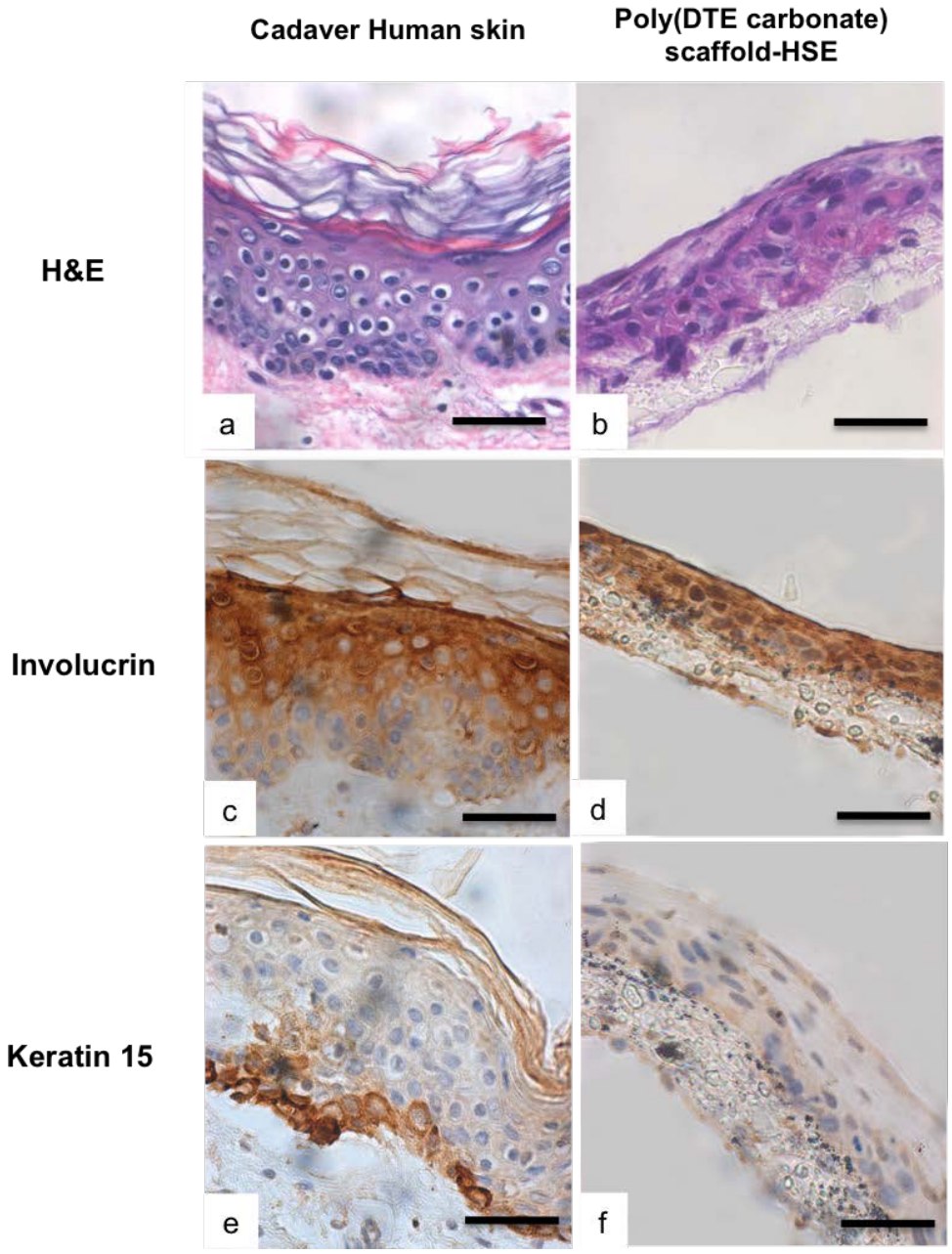

Figure 5.21 Histology H&E and immunohistochemistry staining of cadaver human skin and three week cultured poly(DTE carbonate) based –HSEs. Cross-section H&E staining of cadaver human skin (a) and poly(DTE carbonate) based –HSEs (b). Immunohistochemistry staining of keratinocyte differentiation marker, involucrin on cadaver human skin (c) and poly(DTE carbonate) based –HSEs (d). Immunohistochemistry staining of keratinocyte proliferation marker, keratin 15 on cadaver human skin (e) and poly(DTE carbonate) based –HSEs (f). Scale bar indicates 50 μm.

The development of HSEs was examined by confocal imaging. One, two and three weeks cultured poly(DTE carbonate)-HSEs were stained with fluorescent dyes that labeled nuclei and F-actin filaments. The samples were fixed and imaged with confocal microscopy. The epidermal and dermal surfaces of the poly(DTE carbonate) HSEs were shown in Figure 5.22. For the HaCaT, the actin filaments slightly increased from week one to week three. For the HDF, the actin filaments were similar at week one and week two but slightly decreased at week three. The confocal Z-stacking provided cross-section images of the poly(DTE carbonate)-HSEs (Figure 5.23). While the HDF on the dermal layer remained a similar trend of actin and nuclei expression, the HaCaT on the epidermal layer have increased expression of actin filaments, which confirmed the keratinocyte differentiation at week three.

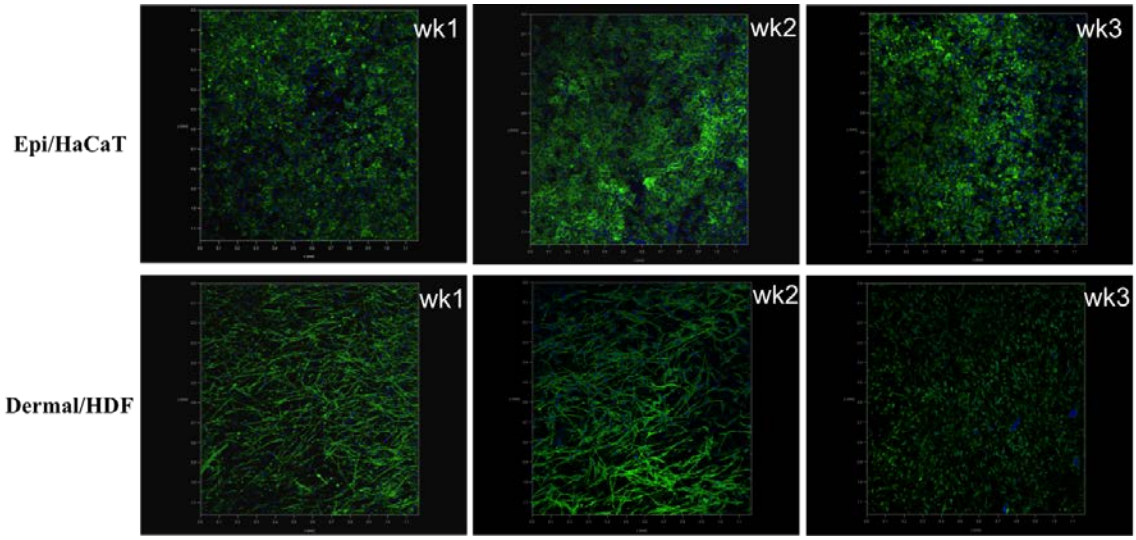

Figure 5.22 Confocal images of the epidermis and dermis surfaces of poly(DTE-carbonate)-HSEs at week one, two and three. The F-actin filaments were stained in green and nuclei were stained in blue.

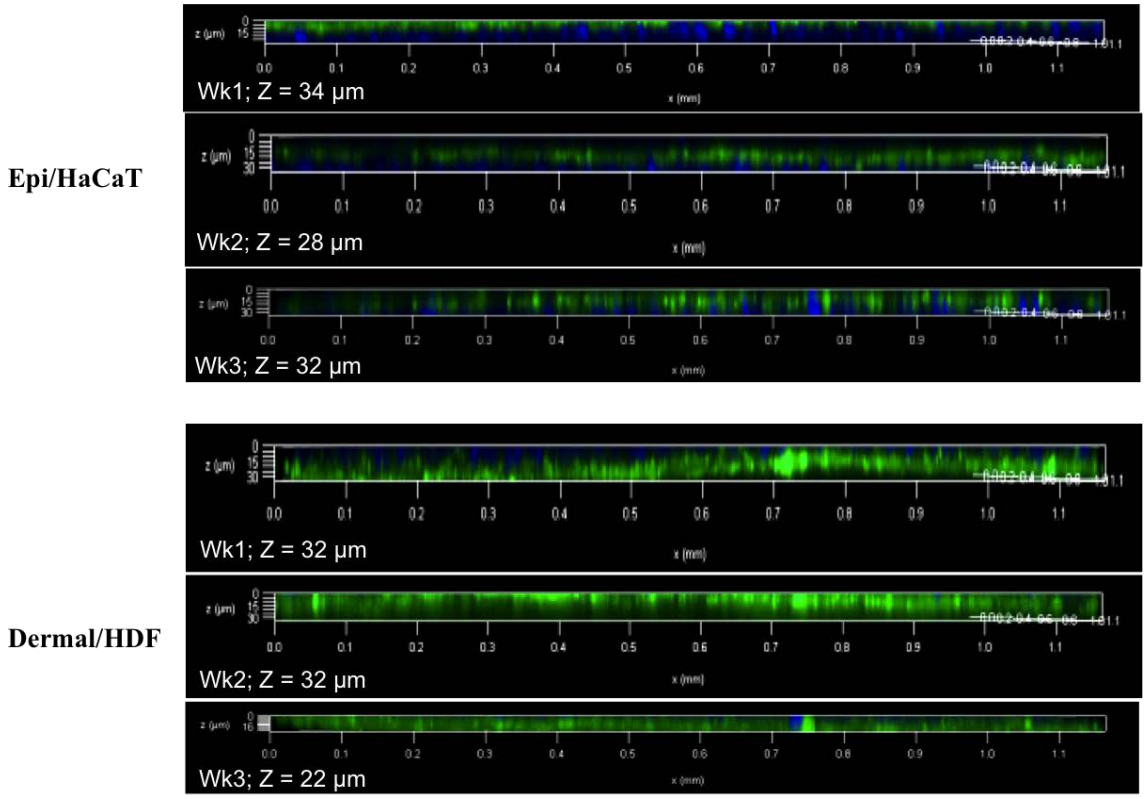

Figure 5.23 Confocal Z-stacking images of poly(DTE carbonate)-HSEs at week one, two and three with imaging depth ranging from 28 to 34 µm. The F-actin filaments were stained in green and nuclei were stained in blue.

5.4. Conclusions

Electrospinning is a simple and versatile technique to produce nano and microfiber scaffolds from synthetic, natural or blend polymers. Poly(DTE carbonate) with drug loading and chitosan blend were successfully electrospun into non-woven fiber mats. The fiber mats were homogeneous in appearance with average fiber size ranging from 1.8 ± 0.5 to 2.4 ± 1.0 µm. Mechanical properties of the mats were desired with Young's modulus of 48.4 ± 9.1 MPa and the hydrophobic surface of the mats were able to tune with addition blends of chitosan. Retinoic acid loaded poly(DTE carbonate) fiber

mats were able to display controlled delivery of retinoic acid into aqueous media. Drug release kinetics was best described with Higuchi and zero order models.

This study investigated the fabrication, optimization and cellular interaction of several electrospun poly(DTE carbonate) fiber mats. The cell-matrix interactions were greatly affected by the addition of drug loading (i.e., retinoic acid) and additional polymer blend (i.e., chitosan). In our study, the addition of retinoic acid and chitosan did not improve the cell attachment and proliferation of the fiber mats compared to blank poly(DTE carbonate). However, fiber mats with poly(DTE carbonate) resulted in excellent cell attachment (>75%) and proliferation of HDF and HaCaT were higher than type 1 collagen gel and TCPS. Therefore, the poly(DTE carbonate) fiber mats were further selected for constructing HSEs *in-vitro*.

The resulting poly(DTE carbonate) fiber mat based HSEs exhibited multiple layers of epidermis which were similar to those of human epidermis. Although keratinocyte proliferation marker, keratin 15 was absent from the 3 week-HSEs, extensive expression of keratinocyte differentiation marker, involucrin was found. In conclusion, the poly(DTE carbonate) based HSEs are a promising 3D human skin equivalent and may be applied in future *in-vitro* drug screening application such as high-throughput screening and skin-on-a-chip platform.

5.5. References

1. Farrugia, B.L., Brown, T.D., Upton, Z., Hutmacher, D.W., Dalton, P.D., and Dargaville, T.R. Dermal fibroblast infiltration of poly(epsilon-caprolactone) scaffolds fabricated by melt electrospinning in a direct writing mode. Biofabrication 5, 025001, 2013.
2. Kobsa, S., Kristofik, N.J., Sawyer, A.J., Bothwell, A.L., Kyriakides, T.R., and Saltzman, W.M. An electrospun scaffold integrating nucleic acid delivery for treatment of full-thickness wounds. Biomaterials 34, 3891, 2013.
3. Yang, Y., Xia, T., Chen, F., Wei, W., Liu, C., He, S., and Li, X. Electrospun fibers with plasmid bFGF polyplex loadings promote skin wound healing in diabetic rats. Mol Pharm 9, 48, 2012.
4. Bonvallet, P.P., Culpepper, B.K., Bain, J.L., Schultz, M.J., Thomas, S.J., and Bellis, S.L. Microporous dermal-like electrospun scaffolds promote accelerated skin regeneration. Tissue Eng Part A 20, 2434, 2014.
5. Chen, H.L., Huang, J., Yu, J.H., Liu, S.Y., and Gu, P. Electrospun chitosan-graft-poly (epsilon-caprolactone)/poly (epsilon-caprolactone) cationic nanofibrous mats as potential scaffolds for skin tissue engineering. International Journal of Biological Macromolecules 48, 13, 2011.
6. Powell, H.M., and Boyce, S.T. Engineered human skin fabricated using electrospun collagen-PCL blends: morphogenesis and mechanical properties. Tissue Eng Part A 15, 2177, 2009.
7. Wang, T.W., Wu, H.C., Huang, Y.C., Sun, J.S., and Lin, F.H. Biomimetic bilayered gelatin-chondroitin 6 sulfate-hyaluronic acid biopolymer as a scaffold for skin equivalent tissue engineering. Artif Organs 30, 141, 2006.
8. Wang, T.W., Huang, Y.C., Sun, J.S., and Lin, F.H. Organotypic keratinocyte-fibroblast cocultures on a bilayer gelatin scaffold as a model of skin equivalent. Biomed Sci Instrum 39, 523, 2003.
9. El Ghalbzouri, A., Commandeur, S., Rietveld, M.H., Mulder, A.A., and Willemze, R. Replacement of animal-derived collagen matrix by human fibroblast-derived dermal matrix for human skin equivalent products. Biomaterials 30, 71, 2009.
10. Ertel, S.I., and Kohn, J. Evaluation of a series of tyrosine-derived polycarbonates as degradable biomaterials. J Biomed Mater Res 28, 919, 1994.
11. Kohn, J., Darr, A., and Schut, J. Polymers Derived From L-Tyrosine. Florida: CRC Press; 2011.
12. Gunatillake, P.A., and Adhikari, R. Biodegradable synthetic polymers for tissue engineering. Eur Cell Mater 5, 1, 2003.
13. Ingavle, G.C., and Leach, J.K. Advancements in electrospinning of polymeric nanofibrous scaffolds for tissue engineering. Tissue Eng Part B Rev 20, 277, 2014.
14. Tan, W., Krishnaraj, R., and Desai, T.A. Evaluation of nanostructured composite collagen--chitosan matrices for tissue engineering. Tissue Eng 7, 203, 2001.
15. Flemming, R.G., Murphy, C.J., Abrams, G.A., Goodman, S.L., and Nealey, P.F. Effects of synthetic micro- and nano-structured surfaces on cell behavior. Biomaterials 20, 573, 1999.
16. Sun, T., Mai, S., Norton, D., Haycock, J.W., Ryan, A.J., and MacNeil, S. Self-organization of skin cells in three-dimensional electrospun polystyrene scaffolds. Tissue Eng 11, 1023, 2005.
17. Rho, K.S., Jeong, L., Lee, G., Seo, B.M., Park, Y.J., Hong, S.D., Roh, S., Cho, J.J., Park, W.H., and Min, B.M. Electrospinning of collagen nanofibers: effects on the behavior of normal human keratinocytes and early-stage wound healing. Biomaterials 27, 1452, 2006.
18. Powell, H.M., Supp, D.M., and Boyce, S.T. Influence of electrospun collagen on wound contraction of engineered skin substitutes. Biomaterials 29, 834, 2008.

19. Dhandayuthapani, B., Krishnan, U.M., and Sethuraman, S. Fabrication and characterization of chitosan-gelatin blend nanofibers for skin tissue engineering. J Biomed Mater Res B Appl Biomater 94, 264, 2010.
20. Noh, H.K., Lee, S.W., Kim, J.M., Oh, J.E., Kim, K.H., Chung, C.P., Choi, S.C., Park, W.H., and Min, B.M. Electrospinning of chitin nanofibers: degradation behavior and cellular response to normal human keratinocytes and fibroblasts. Biomaterials 27, 3934, 2006.
21. Kohn, J., Welsh, W.J., and Knight, D. A new approach to the rationale discovery of polymeric biomaterials. Biomaterials 28, 4171, 2007.
22. Asikainen, A.J., Pelto, M., Noponen, J., Kellomaki, M., Pihlajamaki, H., Lindqvist, C., and Suuronen, R. *In-vivo* degradation of poly(DTE carbonate) membranes. Analysis of the tissue reactions and mechanical properties. Journal of Materials Science-Materials in Medicine 19, 53, 2008.
23. Manohar, A., Shome, S.G., Lamar, J., Stirling, L., Iyer, V., Pumiglia, K., and DiPersio, C.M. Alpha 3 beta 1 integrin promotes keratinocyte cell survival through activation of a MEK/ERK signaling pathway. J Cell Sci 117, 4043, 2004.
24. Watt, F.M., Jordan, P.W., and O'Neill, C.H. Cell shape controls terminal differentiation of human epidermal keratinocytes. Proc Natl Acad Sci U S A 85, 5576, 1988.
25. Roos, T.C., Jugert, F.K., Merk, H.F., and Bickers, D.R. Retinoid metabolism in the skin. Pharmacol Rev 50, 315, 1998.
26. Dash, S., Murthy, P.N., Nath, L., and Chowdhury, P. Kinetic modeling on drug release from controlled drug delivery systems. Acta Pol Pharm 67, 217, 2010.
27. Chang, H.I., and Wang, Y. Cell responses to surface and architecture of tissue engineering scaffolds: INTECH; 2011.
28. Lee, J.H., Jung, H.W., Kang, I.K., and Lee, H.B. Cell behaviour on polymer surfaces with different functional groups. Biomaterials 15, 705, 1994.
29. Bush, K.A., Driscoll, P.F., Soto, E.R., Lambert, C.R., McGimpsey, W.G., and Pins, G.D. Designing tailored biomaterial surfaces to direct keratinocyte morphology, attachment, and differentiation. J Biomed Mater Res A 90, 999, 2009.
30. Fong, H., Chun, I., and Reneker, D.H. Beaded nanofibers formed during electrospinning. Polymer 40, 4585, 1999.
31. Garg, K., and Bowlin, G.L. Electrospinning jets and nanofibrous structures. Biomicrofluidics 5, 13403, 2011.

6. Chapter 6. Future perspectives and conclusions

Three-dimensional human skin equivalents have significant potential for being useful *in-vitro* tools for testing the safety and efficacy of topically applied agents. The ability to mimic the *in-vivo* environment allows the HSEs to provide tissue responses that are similar to those of *in-vivo* native skin. From our study, dermal scaffolds fabricated using the top-down approach (i.e., decellularized APM) and bottom-up (i.e., electrospun poly(DTEcarbonate)) approach both resulted in HSEs that supported the growth of human dermal fibroblasts in the dermis and differentiation of keratinocytes in the epidermis. In addition, the ability for APM-based HSEs to screen topical irritants based on cell viability and cytokine production provided promising *in-vitro* applications for 3D skin models.

Future work for will include a series of direct comparisons of the two dermal scaffold fabrication approaches. The morphologies and *in-vitro* responses of HSEs based on poly(DTE carbonate) and HSEs based on APM will be compared. In addition, commercially available models based on Type 1 collagen based materials will be used as a control group. Future studies such as comparing the mechanical strength, cell distribution, phenotypes and keratinocyte differentiation markers between the poly(DTE carbonate)-HSEs and APM-HSEs will be conducted. The sensitivity and specificity of the different HSEs test models using an expanded panel of topically applied test substances will also be compared side by side.

In conclusion, the development and optimization of 3D HSEs into standardized, reliable, robust *in-vitro* screening tool that aid the discovery of future drug candidates will assist the research and development endeavors of the pharmaceutical industry.

A Appendix 1

Combined Atomistic Molecular Calculations and Experimental Investigations for the Architecture, Screening, Optimization, and Characterization of Pyrazinamide Containing Oral Film Formulations for Tuberculosis Management

Oluwatoyin Adeleke, Nkwe Monama, Pei-Chin Tsai, Happy M.Sithole, and Bozena Michniak-Kohn

Published in Mol Pharmaceutics, 2016, 13(2):456-471

A.1. INTRODUCTION

Tuberculosis (TB) is a highly contagious, airborne disease mainly caused by the bacillus, *Mycobacterium tuberculosis* which most commonly infects the lungs (pulmonary TB) and rarely any other part of the body (extra-pulmonary TB).[1-4] It is considered a serious, life threatening infection worldwide and it remains one of the world's most lethal communicable diseases.[1,2] An estimate of 9 million new TB cases occur annually and about 1.5 – 2 million of these cases have led to death.[1,5] Nonetheless, it can be successfully treated and also prevented in highly susceptible individuals by employing existing anti-TB drugs but poor patient compliance with recommended treatment regimens is a major challenge impeding successful pharmacotherapeutic outcomes.[1-4] This constitutes a major contributing factor to the rising incidences of the various types of resistances such as multi-drug resistance (MDR), single drug resistance (SDR) and extensive drug resistance (XDR) which are the major causes of multiple deaths globally.[3,4] Additionally, TB co-infection in HIV (Human Immunodeficiency Virus) patients has significantly amplified the severity of the disease, complicated its management processes as well as decreased the life expectancy of such individuals.[3,5]

Drug treatment still remains the most effective way of curing TB-infected individuals, averting fatality and relapse, preventing its spread to healthy persons and stopping the development and transmission of drug resistant strains.[1,2,6] Pyrazinamide (PYZ) also known as pyrazinecarboxamide is a synthetic analogue of nicotinamide.[1] It is amongst the primary drugs recommended by the World Health Organization (WHO) for the effective management of TB.[6,9] PYZ is a bactericidal antimycobacterial agent used (in combination with isoniazid, rifampicin and ethambutol) at the first stage of TB treatment.[1,6,9] It acts by killing slowly metabolizing/dormant TB causing bacilli more effectively than those at the actively metabolizing phases leading to a low occurrence of bacteriological relapse after completion of the pharmacotherapeutic course.[6,9,10-12] PYZ is known to significantly shorten the treatment duration in TB patients (from ~11 months to ~6 months) and this makes it difficult to exclude PYZ in any currently employed anti-TB combination regimens.[11,12]. In addition, PYZ is a clinically important bioactive molecule for the treatment of HIV/TB co-infected patients, cases of MDR and XDR tuberculosis as well as tuberculosis meningitis as it is able to cross the inflamed meninges[10,11]. Adverse reactions associated with PYZ usage are usually dose and treatment duration dependent but can happen at any moment within the therapy period.[9] The most common severe adverse effect of PYZ is hepatotoxicity which can have fatal consequences if not well managed.[9-11] PYZ is a class III drug according to the Biopharmaceutics Classification System (BCS) typified by it high solubility (15 mg/mL at 25°C) and relatively low permeability (log P = -1.88)[9,11].

The emergence of drug resistant TB strains and the fact that the processes of synthesizing and approving new, safe anti-TB bioactive molecules are quite slow constitute major constraints with regards to the ongoing attempts to control its global spread and fatal impacts.[5,12] In fact, thus far, only two new drugs, bedaquiline and delamanid, have been recently approved.[5] The development of drug resistant TB is majorly attributable to the exposure of bacteria strains to sub-therapeutic levels of one or more anti-TB agent.[12] This is mainly caused by poor patient adherence with prescribed treatment schemes due to the occurrence of unbearable side effects, high drug dosing especially for the oral route, prolonged treatment durations and poor bioavailability (due to reduced cell permeability, untimely drug degradation).[4,5,12] Therefore, the invention of more efficient delivery systems for the existing, still potent TB drugs (as single moieties or combinations), which can potentially minimize adverse effects, high doses and treatment duration is crucial to alleviating the problem of patient non-compliance and its detrimental global effects.[5,12]

Therefore, the use of an orally disintegrating, permeable film delivery system can serve as an alternative and a more efficient approach to deliver orthodox anti-TB drugs. The oral route is the most commonly acceptable way of administering drugs because of its non-invasiveness, simplicity, stability, dose accuracy, production flexibility and convenience which results in a high level of compliance.[1] Orally disintegration films are generally slim drug-loaded solid dosage forms which readily disintegrate/dissolve within the oral cavity enhancing rapid mucosal penetration, systemic absorption and onset of action.[1,2,13] They are a remarkable class of delivery systems with enormous advantages which include but are not limited to: (i) promoting patient compliance[14], (ii) flexibility,

inherently easy to use anywhere and scarcely spitted out[13-15], (iii) usefulness in paediatric, geriatric, dysphagic and unconscious/bedridden and difficult patients [13,14], (iv) allowing the fabrication of patient-tailored drug targets[14], (v) effectiveness for the delivery of drugs with narrow therapeutic windows[14], (vi) not requiring water/liquid for swallowing[13-15] and (vii) enhancing bioavailability of drug that are susceptible to hepatic metabolism by promoting transmucosal absorption for therapeutic activity and can also minimize the occurrence of adverse effects[14].

Computer-aided molecular modeling (CMD) forms an essential component of pharmaceutical research nowadays and has been shown to be an absolutely useful tool for the thorough evaluation and optimization of multi-component drug delivery systems at both complex and atomistic structural levels.[16-21] Systematic molecular modeling can be employed to study structural intricacies and transitions, salient physical properties as well as optimize drug delivery systems.[16] CMD is a cost-effective method because expensive, time-consuming and labor intensive experimental procedures can be significantly reduced or completely excluded.[16,20,21] A major advantage of the CMD is that it facilitates the screening processes which implies that evidently substandard compositions can be identified and excluded while promising lead compositions can be focused on for formulation and optimization.[20]

The current investigation focuses on developing an optimized rapidly disintegrating oral film formulation containing PYZ, a key drug indicated for the treatment of new TB infection, drug resistant TB (MDR and XRD), pediatric TB, HIV/TB co-infection.[5,6,9-12] Considering the enormous advantages of orally disintegrating films highlighted above, loading PYZ unto these unique and convenient matrices can

potentially address the challenge of patient non-adherence encountered during typical TB management schemes leading to improved pharmacotherapeutic efficacy and eventually marketing advantages. These PYZ containing films were initially constructed *in silico* employing relevant biocompatible polymeric and non-polymeric molecules. All computation steps were based on the COMPASSII (Condensed-phase Optimized Molecular Potentials for Atomistic Simulation Studies) version 1.0 force-field of the *Forcite* and *Amorphous Cell* components of the Materials Studio, version 7.0. Mutual miscibility between PYZ and utilized excipients was simulated based on systems' energy dynamics to compare various film-drug matrices in order to effectively select the most stable/compatible one as the optimized film formulation. Simulated outputs were validated against experimental results and finally the selected optimal film formulation was characterized employing *in-vitro, ex-vivo* and *in silico* approaches.

A.2. MATERIALS AND METHODS

A.2.1. Materials

Polyvinyl alcohol-polyethylene glycol graft copolymer (Kollicoat®IR) was a gift received from BASF, The Chemical Company (Ludwigshafen, Germany), citric acid anhydrous, glycerol, pyrazinamide, sodium chloride, anhydrous sodium phosphate dibasic and potassium dihydrogen phosphate monobasic buffer salt were purchased from Sigma Chemical Company (St. Louis, MO, USA). Phosphoric acid (85%, ACS Grade) was obtained from Fisher Scientific Company (Fair Lawn, NJ, USA). All other reagents were used as received. Primary neonatal human dermal fibroblasts, Dulbecco's modified eagle's medium, AlamarBlue cell viability reagent, fetal bovine serum, penicillin,

streptomycin, amphotericin B, phosphate buffered saline, pH 7.4 were purchased from Life Technologies (Grand Island, NY, USA).

A.2.2. *In silico* construction and evaluation of the PYZ-Loaded Oral Film Variants

Four oral film (OF) formulas were independently explored. This selection of excipients was based on the one-variable-at-a-time approach employing different ratio combinations of Kollicoat®IR, glycerol, anhydrous citric acid and PYZ as the model drug. Each component compound was built *in silico* using the *Polymer* and *Molecule Builders* of the Materials Studio (version 7.0, Accelrys Inc., San Diego, CA, USA) based on the *in silico* combinations presented in Table 1 below. To minimize the complexity of the calculation and the accuracy of the available computing resource[22], the copolymer, Kollicoat®IR, chain was fixed at 20 units while all other non-polymeric components were built based on their standard chemical structures. A number of available options for joining the polymeric chains were explored and screened. The options included homopolymer, block copolymer, random copolymer and dendrimer. The homopolymeric structure of the Kollicoat®IR had the most stable, lowest total energy configuration and was selected and employed for subsequent molecular calculation. Total energy computations in this case included non-bond, hydrogen bond, van der Waals forces, electrostatic forces, diagonal forces, bond, bending angle, torsion, inversion and cross terms interaction components within the molecules.

All built compounds were subjected to geometry optimization employing the *Forcite* module as non-periodic structures within the Materials Studio modeling environment. An atom based geometry optimization was performed for all excipients. The *Smart* algorithm[22,23] (cascade of the steepest descent, conjugate gradient, quasi-Newton and adjusted basis set Newton-Raphson methods) coupled with the COMPASSII force-field was used for the geometry optimization of all component compounds. Research has shown that the COMPASSII force field is highly efficient and accurate for the simultaneous calculations of molecular interactions and properties of both gas and condensed phases of a broad range of molecules and polymers.[16,22] Optimization calculations were run continuously until the points of convergence and minimum energy were reached. The geometrically optimized structural configurations of all the excipients and their total energy values are illustrated in Figure A.1.

Table A. 1 *In silico* composition of the different PYZ-loaded oral films

Formulation	***In Silico* Weighting**			
Description	**Kollicoat®IR**	**Citric Acid**	**Glycerol**	**Pyrazinamide**
OF 1	72.60	2.90	16.10	8.40
OF 2	71.70	4.30	13.81	10.12
OF 3	68.20	5.52	15.80	10.50
OF 4	71.90	4.30	11.80	12.00

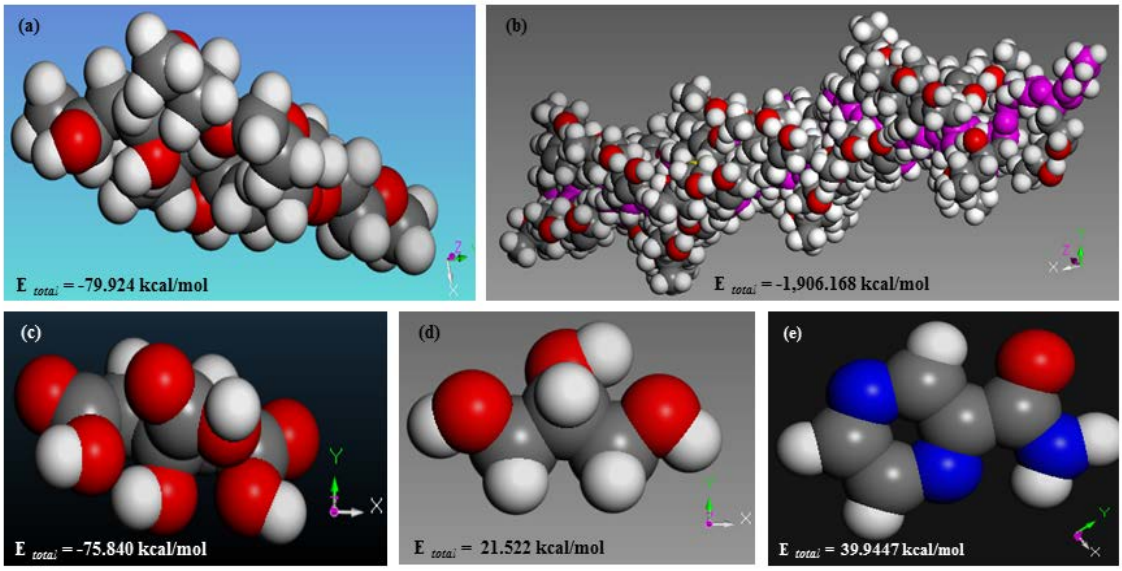

Figure A. 1 Corey-Pauling-Koltun (CPK) models of geometrically optimized structural configurations of the constituents of the oral film: (a) single-unit Kollicoat®IR, (b) twenty-unit Kollicoat®IR, (c) anhydrous citric acid, (d) glycerol and (e) pyrazinamide.

In order to build each dry PYZ containing oral film based on the combinations highlighted in Table A.1, the *Amorphous Cell* module was utilized. All component molecules were loaded into a single frame cubic lattice under periodic boundary conditions. Computer-aided construction of the films was atom-based and performed under standard room temperature (298 K) and a density of 1 g/cm^3. Simulations were performed systematically until the point of convergence characterized by the lowest energy level employing the COMPASSII force field and *Smart* algorithm. The films were constructed *in silico* in a dry environment (absence of water molecules) to mimic the final product after processing and drying. Figure A.2(a)-2(d) presents the stable, ellipsoidal periodic structural configuration of each oral film at the point of convergence. The total interaction energy (E_T), kinetic energy (E_K), solubility parameter (S) and cohesive energy density (*CED*) were calculated for each construct.[22,23]

In addition, an attempt was made to predict the behavior of the film formulations in the presence of simulated saliva. In order to accomplish this, each film construct was packed with water molecules (1:1) employing the *Amorphous Cell* module, the COMPASSII force field and *Smart* algorithm. Water was selected for this purpose because it is the major component of pH 6.8 simulated saliva (2.382 g anhydrous sodium phosphate dibasic, 0.19 g potassium dihydrogen phosphate monobasic buffer salt, 8 g sodium chloride, phosphoric acid for pH adjustment and 1 L distilled water).[24,25] Computer-based simulations focusing on molecular interactions are capable of providing insight into the effect of water molecules (hydration) on the physical properties of polymer-based systems.[22] Also, the E_T, E_K, S and *CED* were calculated for all hydrated film constructs.[22,23,26] A typical *in silico* image of the film formulation soaked in water molecules (representing simulated saliva) is shown in Figure A.2 (e).

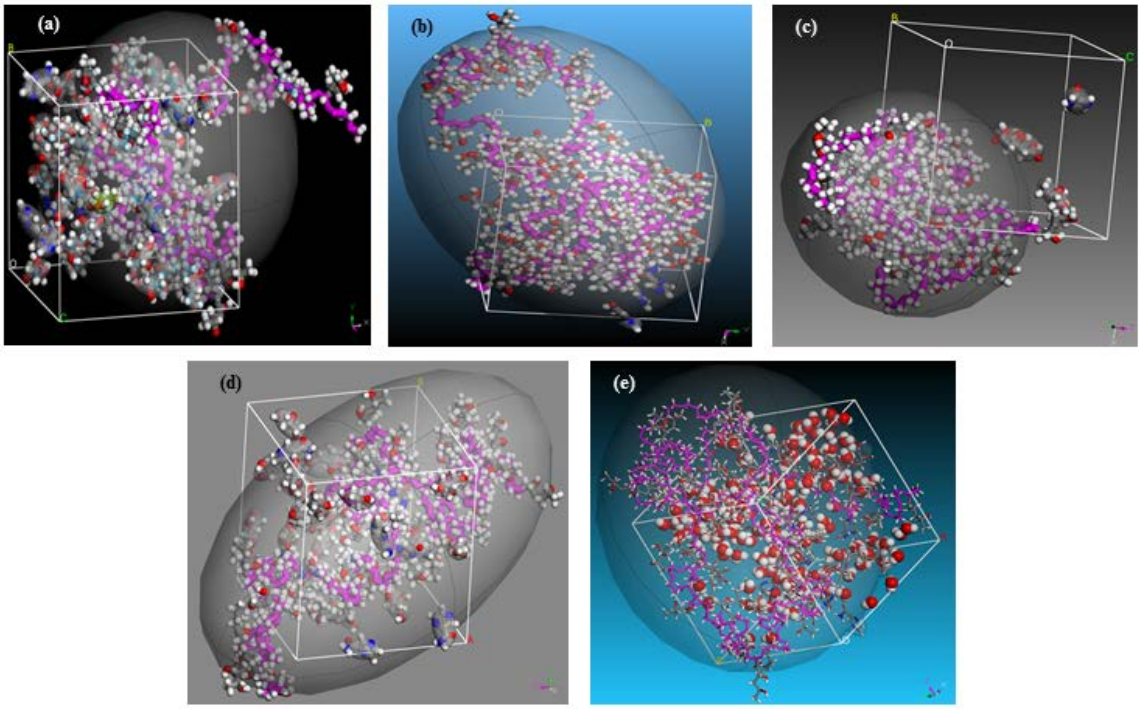

Figure A. 2 Ellipsoidal periodic images of geometrically optimized constructs at the point of convergence: (a) OF 1, (b) OF 2, (c) OF 3, (d) OF 4 and (e) the optimal film soaked in an aqueous milieu.

A.2.3. *In-Vitro* Preparation of the Oral Film variants

A.2.3.1. *In-Vitro* preparation of the Four Oral Film formulations

Four different oral film formulations of PYZ were prepared based on the specifications outlined in Table A.1 employing the solvent casting technique.[27,28] The respective solutes (Kollicoat®IR, glycerol, citric acid and pyrazinamide) were accurately weighed on a calibrated weighing balance (AT200 Electronic Analytical Weighing Balance, Mettler Toledo, Greifensee, Switzerland) and directly dispersed in appropriate quantities of deionized water under continuous magnetic stirring at a speed of about 400

rpm (Five-Position Hot Plate/Stirrer, Model 51450 series, Cole-Parmer, IL, USA) for 2 hours under room conditions. The resulting aqueous solution was kept stationary, away from light and moisture for 1 hour to release entrapped air bubbles. Subsequently, the final solutions were separately casted onto clean 5 cm diameter circular teflon plates and allowed to dry to constant weight in a manual convection chamber containing silica gel plates (to aid drying process) under room conditions (temperature = 24 ± 2°C, humidity = 60 ± 2%) over 15 hours. Dried films were cut into smaller circular discs (1.59 cm diameter) using a manual punch, photographed quickly and stored separately away from direct sunlight in airtight packets under room conditions for further testing.

A.2.3.2. Film Thickness and Mass Uniformity

Film mass was determined utilizing an analytical weighing balance (Mettler AT 200, Mettler Toledo, LLC, Columbus, OH, USA). Film thickness was measured with a digital micrometer screw gauge (Mitutoyo Deutschland GmbH, Neuss, Germany). Each film was measured at five different spots around its circumference and at the center. Measurements were done using three replicate samples of films with surface areas of 2.49 cm^2 at each time-point.

A.2.3.3. Determination of Film Disintegration Time, Dissolution Time and Dissolution pH

A modification of the petri dish method reported by Garsuch et al.[29] Each tested film were circular in geometry and had a diameter of 1.59 cm with a calculated surface area of 2.49 cm^2. Each sample was inserted into 5 mL of pre-heated (37 ± 0.1°C) simulated saliva contained in a closed cylindrical glass vial and placed into a shaking

water bath (Julabo, SW 22, Julabo, Labortechnik, GmBH, D-77960, Seelbach, Germany) maintained at 37 ± 0.1°C and 10 rpm. Changes in sample appearances were physically observed against a white fluorescent light background to enhance visibility. The disintegration time ($t_{disintegration}$) was recorded using a digital stopwatch (EXTECH, Nashua, NH, USA) as the time-point when the collapse of film matrix (loss of film's original conformation) commenced while the dissolution time ($t_{dissolution}$) was recorded at the time-point when the respective film was completely dissolved in the simulated saliva resulting in a clear solution. At this point, the pH of the resulting clear solution was recorded as the dissolution pH ($pH_{dissolution}$) utilizing a portable pH meter (Accumet® AP 61, Fisher Scientific, Pittsburgh, PA, USA). All measurements were performed in triplicate.

A.2.3.4. Drug Content Uniformity Assessment

Each test sample was placed in 5mL simulated saliva and magnetically stirred at a speed of about 200 rpm (Five-Position Hot Plate/Stirrer, Model 51450 series, Cole-Parmer, IL, USA) over 60 minutes to ensure complete dissolution and release of the PYZ molecules. The produced solution was then appropriately diluted and passed through a nylon syringe filter (Whatman™, GE Healthcare UK Limited, Buckinghamshire, UK) of pore size 0.2 µm. The collected filtrate was analyzed by Ultra Violet Visible (UV-Vis) spectrophotometry (Cary® 50 UV-Vis machine equipped with the UV dissolution software version 4.1, Varian, Belrose, Australia) at λ_{max} = 268 nm to detect PYZ absorbance value. The absorbance values generated were then fitted into a linear

polynomial equation ($y = 77.16x; R^2 = 0.97$) of the calibration curve of PYZ in simulated saliva to calculate the actual PYZ content. Measurements were carried out in triplicate.

A.2.3.5. Evaluation of the Surface Topographical Characteristic of the Oral Films

The surface topography of the formulations OF 1 – OF 2 was examined under a scanning electron microscope (Field Emission Scanning Electron Microscope, JSM 7500 F, JEOL, Peabody, MA, USA) at a magnification of ×250. Samples were cut into regular pieces (0.5 cm^2), mounted on stainless steel stubs and carbon sputter coated using a carbon vacuum evaporator (Emitech K950x, Quorum Technologies Ltd, Ashford Kent, UK). Microscopical observations were made employing an accelerating voltage of 3 kV.

A.2.3.6. Criteria for the Selection of the Optimal Film Formulation

The careful selection of the ideal film formulation was objective and based on generated computed and experimental outputs.

A.2.4. Physicochemical and Physicomechanical Characterization of the Selected Optimal Oral Film Formulation

A.2.4.1. *In-Vitro* Dissolution Behavior and Kinetics

For the evaluation of the drug release performance of the selected optimized film formulation, samples were tested in triplicate under biorelevant conditions. Each optimal film (diameter = 1.59 cm) was immersed into 5 mL preheated (37 ± 0.1 °C) simulated saliva contained in a closed glass vial (to prevent evaporation) which was then placed in a shaking water bath (Julabo, SW 22, Julabo, Labortechnik, GmBH, D-77960, Seelbach, Germany) set at 37 ± 0.1°C and 10 rpm. At each predetermined time-points (1, 4, 7, 10, 13, 16, 19, 22, 25, 30 minutes), 1 mL sample was collected and replaced with equal amount of freshly prepared simulated saliva maintained at 37 ± 0.1°C. Collected samples were appropriately diluted and filtered through a Millex-GP (Millipore Express membrane) 0.2µm pore size filter unit (Merck Millipore Corporation, Billerica, MA, USA) and analyzed spectrophotometrically (Cary® 50 UV-Vis Varian, Belrose, Australia) at 268 nm. The actual concentration of PYZ released per time was calculated utilizing the linear calibration equation ($y = 77.16x;\ R^2 = 0.97$). The kinetics of drug release was mathematically determined by fitting the generated profile into a selection of mathematical models using the KinetDS, version 3.0 open source software. The selection of the model of best-fit was based on the value of the correlation coefficient (R) closest to 1. The mathematical models employed were zero order (eq 1), first order (eq 2), Korsmeyer-Peppas (eq 3) and Higuchi (eq 4).[30-32]

$$Q_t = Q_0 + K_0 t \qquad (\textbf{\textit{Zero order}}) \qquad (1)$$

where Q_t is the quantity of PYZ released or dissolved, Q_0 is the initial amount of PYZ in solution , K_0 is the zero order rate constant and t is time.

$$logQ_t = logQ_0 - K_1t / 2.303 \qquad (\textbf{\textit{First order}}) \qquad (2)$$

where Q_t is the quantity of PYZ released or dissolved, Q_0 is the initial amount of PYZ in solution , K_1 is the first order rate constant and t is time.

$$Q_t/Q_\infty = K_pt^n \qquad (\textbf{\textit{Korsmeyer-Peppas}}) \qquad (3)$$

where Q_t/Q_∞ is the fraction of PYZ released at a particular time t, K is the rate constant and n is the release exponent which is employed for the characterization of different release mechanisms.

$$Q_t = K_ht^{1/2} \qquad (\textbf{\textit{Higuchi}}) \qquad (4)$$

where Q_t is the quantity of PYZ released, K_h is the Higuchi model release rate constant and t is time.

A.2.4.2. Powder X-ray diffraction (PXRD)

A qualitative PXRD study was performed on the optimized film formulation employing the X-ray diffractometer equipped with the X'Pert PRO data collector software (PANalytical Inc. Westborough, MA, USA). The machine was operated with the Cu K-alpha radiation of 1.540598 Å with a generator set at a voltage of 45 kV and current of 40 mA. Scanning was continuous and ranged between 1° and 80° 2θ at 0.026 scan step size and a rate of 126.99 seconds/step. The divergence slit was fixed at 0.05 mm and measurements were made under both reflection and transmission mode. About 2

mg of the test sample was loaded onto standard sample holders and tested. The samples were continuously scanned between a range of 5.0° and 90.5° with a scan step size of 0.03.

A.2.4.3. Differential Scanning Calorimetry (DSC)

The thermal properties of the optimized film formulation were analyzed using the DSC machine (Q2000 Differential Scanning Calorimeter equipped with 50-position Autosampler, TA Instruments, New Castle, DE, USA) equipped with a STARe Thermal Analysis Software version 12.0 (Mettler Toledo, Switzerland). 8.30 mg of each test sample was placed in separate aluminium pans with perforated lids while an empty crucible served as the reference. Measurements were performed employing three test samples with each heated in three cycles within the range of 0°C - 220°C at a rate of 10°C/minute under inert nitrogen flow of 25 mL/minute.

A.2.4.4. Fourier transform infrared spectroscopy (FTIR)

The FTIR spectra for the optimized film formulation and pure PYZ were recorded on the Perkin Elmer Spectrum 100 Series FTIR Spectrophotometer equipped with the Spectrum V 6.2.0 software (Beaconsfield, Buckinghamshire, UK). The sample holder and machine stage were thoroughly cleaned with ethanol and blank scans were recorded. Thereafter, 10 mg of each sample was placed on the holder situated on the machine stage for analysis. All measurements were performed at wave numbers ranging from 4000-600 cm^{-1}, scan time = 32 scans and resolution of 4 cm^{-1}. All recorded output scans were computed as an average of three repeated readings.

A.2.4.5. Ex vivo Permeation Studies Employing Porcine Buccal Tissue

The porcine buccal mucosal tissue samples obtained from the cheek region of freshly slaughtered pigs were supplied by Tissue Source^{LLC} (Lafayette, IN, USA). Tissue specimens (Group ID: WHI010414, Batch Number: 262010414-20) were shipped in phosphate buffered saline in a refrigerated transport box. Once received, they were stored away at -70°C until needed. For the permeation experiments, frozen tissue samples were thawed and rehydrated by placing them in freshly prepared phosphate buffered saline (pH 7.4 at 37°C) for about 20 minutes. After rehydration, the mucosal specimens were carefully dissected employing a surgical scissor and scalpel to produce circular tissue disks (thickness = 602 ± 10 µm, diameter = 1.00 ± 0.06 cm and surface area = 0.79 ± 0.02 cm^2) which were immediately carefully mounted between the donor and receiver compartments of the dry heat Franz cell (Drive Console System, Model FDC 24, Logan Instruments Corp, Somerset, NJ, USA) with the epithelial layer facing the donor region. A constant, biorelevant temperature (37 ± 0.1°C) was maintained throughout the whole permeation system and it was ensured that air bubbles were excluded from the whole unit. The receptor compartment contained 5 mL simulated plasma (pH 7.4)[33] prepared by dissolving 0.144 g potassium dihydrogen phosphate monobasic, 0.795 g anhydrous sodium phosphate dibasic and 9 g sodium chloride in 1 L of deionized water. The donor compartment on the other hand contained a solution of the PYZ-loaded optimized film formulation in 1 mL simulated saliva (pH 6.8). The receptor component was subjected to continuous magnetic stirring enabling constant mixing of its constituents and accurate sampling. Each tissue specimen was allowed to equilibrate with the simulated plasma for

10 minutes before the PYZ-loaded film formulation in simulated saliva solution was added to the donor compartment. 1 mL sample was pipetted from the receptor compartment and replaced with freshly prepared simulated plasma maintained at 37 ± 0.1°C. Sampling was done at predetermined time intervals of 1, 10, 20, 30, 60, 90 and 120 minutes. Collected samples were assayed for their PYZ content at 268 nm using the Cary® 50 UV-Vis spectrophotometer.

PYZ flux (J_{ss}) through the excised porcine buccal mucosa was calculated at steady state per unit area employing eq 5[34,35] while the permeability coefficient (k_p)[31] was obtained from eq 6 below.

$$J_{ss} = Q / A \times t \qquad (5)$$

where J_{ss} = steady state drug flux (mg/cm^2 min), Q = quantity of PYZ that permeated through the porcine buccal mucosa (mg), A = active cross sectional area accessible for diffusion (cm^2) and t = exposure time (minutes).

$$k_p = Jss/C_d \qquad (6)$$

where k_p = permeability coefficient (cm/minute), J_{ss} = steady state drug flux (mg/cm^2/min), C_d = drug concentration present within the donor compartment (mg/cm^3).

A.2.4.6. *In-vitro* and in silico Determination of the Mechanical Properties

The Sintech 5/d mechanical tester (MTS Systems Corporation, Eden Prairie, MN, USA) equipped with the TestWorks 4 software was used for the measurement of the mechanical properties of the optimal film under room conditions. The optimal film formulation specimen was tested in triplicate. Test samples were trimmed into equal rectangular strips with a length of 50 mm and width of 5 mm. An initial speed of 10 mm/min was set for all determinations. Mechanical parameters measured included maximum force at break, percentage strain (measure of elongation), tensile strength and Young's modulus.

To better comprehend the mechanical characteristics of the optimized PYZ-loaded film, the *Forcite* module based on an atomistic summation process coupled with the COMPASSII force field and *Smart* algorithm was employed for calculations. Computed mechanical parameters included bulk density, shear modulus, compressibility, sound velocity, Lamé constants, viscosity, Young's modulus and bulk modulus.

A.2.5. Stability Studies on the Selected Optimal Oral Film Formulations

A.2.5.1. Short-term *in-vitro* Stability Testing

The optimal film formulation was stored in glass vials under room condition (temperature: 23 ± 3°C; humidity: 65 ± 5%) for 14 days. Investigated indicators of formulation stability included dissolution and disintegration time, drug content uniformity, film thickness and mass.

A.2.5.2. *In silico* Evaluation of Optimal Formulation Stability

In an attempt to better comprehend the stability patterns of the selected film formulation within different surroundings, *in silico* calculations were performed to evaluate the influence of environmental pressure, temperature and humidity fluctuations. The change in the systemic E_T at the different measurement points was employed as the stability indicator. In a nutshell, the system that had lower E_T values was considered more stable and vice versa and calculations were based on atom-to-atom interaction within the *Forcite* and *Amorphous Cell* milieu. The effect of pressure changes was set at 0, 100, 200, 500, 800, 1000 and 1500 MPa under constant ambient temperature = 25°C. The summation was atom-based using the NPT ensemble, thermostat = Nosé-Hoover dynamics, Q ratio = 0.01, barostat = Berendsen, decay constant = 0.1 and forcefield = COMPASSII. Also, the impact of temperature variations on the stability of the optimized film was calculated at room pressure of 0.1 MPa at 0, 5, 25, 30, 40, 50 and 60°C under the same conditions.

Likewise, the influence of water molecules on the stability of the optimized film formulation was systematically calculated employing 5, 50, 100, 150, 300, 400, 500, 650 and 744 water molecules which is equivalent to 0.68, 6.75, 13.50, 20.25, 40.50, 53.99, 67.49, 87.74 and 100.43%w/w. This computation was related to the effect of fluctuations in surrounding humidity on the systemic E_T of the optimized matrix. The various hydrated matrices were built within the *Amorphous Cell* environment using the single frame packing task, density = 1 g/cm^3, temperature = 25°C, loading steps = 1000,

external pressure = 0.1 MPa, algorithm = *Smart*, force field = COMPASSII, summation method = atom-based and truncation = cubic spline. Subsequently, the built hydrated optimized film platform was geometrically optimized and subjected to systematic dynamic calculations employing the *Forcite* tool with the following settings: NPT ensemble, temperature = 25°C, pressure = 0.1 MPa, thermostat = Nosé, barostat = Berendsen, Q ratio = 0.01, force field = COMPASSII and summation = atomistic. *In silico* snapshots of both the unhydrated and hydrated optimized film constructs are shown in Figure A.3.

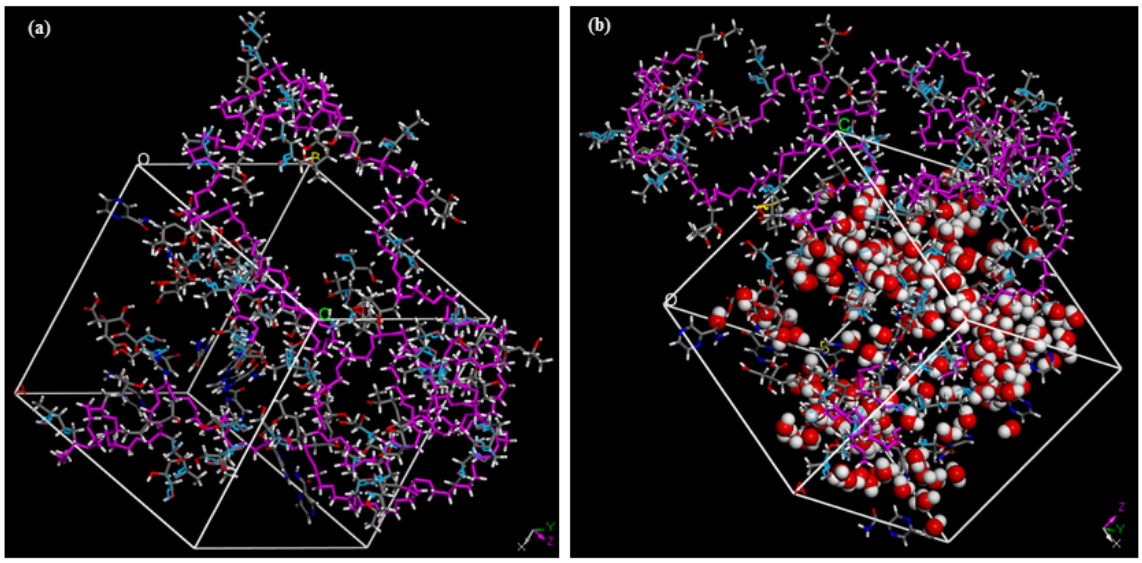

Figure A. 3 Snapshots of typical: (a) unhydrated (b) hydrated *in silico* optimized film architectures (the water molecules are displayed as the red and white CPK style molecules).

A.2.6. *In- vitro* Cytotoxicity Assay

The toxicity of the PYZ-loaded and placebo optimal formulations as well as the free PYZ was examined and compared using the primary neonatal human dermal fibroblasts (HDF) cell line.

A.2.6.1. Cell culture

The HDF cells were cultured in Dulbecco's modified Eagle's medium (DMEM) supplemented with 10% fetal bovine serum (FBS) and 100 units penicillin/ 100 µg units streptomycin/0.25 µg per mL amphotericin B maintained at 37 ± 0.1°C and circulated with 5% carbon dioxide. Medium was changed every other day and early passages with no more than five were used in cytotoxicity assay.

A.2.6.2. *In-vitro* cytotoxicity assay

A day before the experiment, 5,000 per well of HDF were seeded in a 96 well plate. Samples tested included free PYZ, placebo OF 2 and PYZ-loaded optimized film (PYZ-loaded OF 2). Each test sample was separately dissolved in 2 mL of serum-free DMEM. 200 µL of the prepared solutions were added to the top well on the 96 well plates and then a two-fold serial dilution was carried out using the DMEM medium. For the free PYZ and PYZ-loaded OF 2, concentrations tested were based on 0.63, 1.25, 2.5 and 5 mg/mL of PZY. The placebo OF 2 concentration was based on the film weight and test values employed were 20, 10, 5, 2.5 and 1.25 mg/mL. The control group was HDF cells treated with DMEM medium only. The HDF cells were treated with the respective test samples over 24 and/or 48 hours at 37°C/5% CO_2. At each predetermined time-point,

the HDF cells were washed thrice with phosphate buffered saline (pH 7.4). Afterwards, cell viability was measured utilizing the AlamarBlue® assay according to the manufacture's manual. Briefly, 100 µL of DMEM containing 10% of the AlamarBlue® reagent were added to the HDF cells and incubated at 37°C for 3 hours. Each experimental 96 well plates were placed inside the Infinite® 200 PRO series multimode microplate reader equipped with the Tecan i-control™ software (Tecan Group LtD, Männedorf, Switzerland). Fluorescence intensity (FI) was then measured at excitation and emission wavelengths of 560 nm and 590 nm respectively. Excitation and emission bandwidths were set at 9 nm and 20 nm respectively with an integration time of 20 µs. The cell viability was calculated mathematically (eq 7). Each experimental group was treated in triplicate and two independent experiments were performed. Statistical difference between two groups were employed for the Student's T-Test ($p<0.05$) while the difference within multiple groups were applied for the ANOVA-post hoc Dunnette's test ($p<0.05$).

$$\% \text{ Cell Viability} = (\text{FI of experimental group} / \text{FI of control group}) \times 100 \quad (7)$$

where FI is the Fluorescent Intensity.

A.3. RESULTS AND DISCUSSION

A.3.1. *In silico* and *in-vitro* Evaluation of the Prepared Oral Film Formulations

A.3.1.1. Calculated Functionalities for the Modeled Oral Film Formulations

So as to better understand the intrinsic behavior of the dry film formulations (OF 1 – OF 4) as well as facilitate the optimal formulation selection process, the E_T, E_K, *S* and *CED* were computed (Table A.2) for both the dried and hydrated film matrices (Figure A.2). Briefly, the E_T can be described as the sum of contributory inter-particulate interactions (attraction and repulsion potentials) amongst component atoms within a particular system while the E_K is a measure of matrix internal disorder.[36-38] The calculated E_T for each configured film matrix listed in Table A.2 indicates that OF 2 had the lowest total energy value (E_T = -8006.28 kcal/mol) amongst the 4 variants studied. Thus OF 2 is the most stable configured formulation with a well-established inter-atom interaction within its component compounds resulting in the formation of a thermodynamically robust and well-defined film network. In addition, the computed OF 2 E_K value of 1052.98 kcal/mol (Table A.2) shows that it is a moderately dispersed/flexible matrix when compared with OF 1 characterized by the highest level of intra-molecular mobility and disarray as well as OF 3 and OF 4 which are stiffer platforms based on the magnitude of their kinetic energies presented in Table A.2. The *S* and *CED* for each multi-particulate film structures were calculated based on the atomistic intermolecular contributions of their component compounds. The values of *S* and *CED* are both quantitative and depict the intensity of the attractive intermolecular forces (miscibility) amongst the neighboring molecules.[23] Table A.2 shows that OF 2 had the highest *S* and *CED* values compared to OF 1, OF 3 and OF 4 with significantly lower values. This illustrates good intermolecular miscibility and compatibility amongst PYZ, the polymeric and non-polymeric

components of present in the OF 2 formulation resulting in the formation of a thermodynamically stable film structure, which can be related to its low E_T value.

The effect of water-based simulated saliva on the oral films was also evaluated by calculating the E_T, E_K, *S* and *CED* values for each formulation (Table A.2). The magnitude of E_T decreased significantly for all the films matrices indicating their stability even within an aqueous environment. An increase in E_K which can be explained by the process of matrix mobility due to disentanglement and dissolution was also noted for all the formulations. This is further supported by the increase in *S* and *CED* values indicating the stable intermolecular interactions formed between the film matrix and water molecules contained in the simulated saliva. Overall, OF 2 was the most stable in solution based on its lowest E_T , intermediate E_K, highest *S* and *CED* (Table A.2).

Table A. 2 Magnitude of the *in silico* parameters calculated for the dry and hydrated film formulations

Formulations	**Calculated Quantities**			
	E_T (kcal/mol)	**E_K (kcal/mol)**	***S* $(J/cm^3)^{0.5}$**	***CED* (J/m^3)**
Dry Films				
OF 1	-7804.66	1893.73	41.08	1.69×10^9
OF 2	-8006.28	1052.98	44.55	1.99×10^9
OF 3	-5087.03	788.29	32.88	1.08×10^9
OF 4	-7434.77	946.25	42.20	1.78×10^9
Hydrated Films				
OF 1	-25940.02	2232.25	83.81	7.02×10^9
OF 2	-26861.44	1518.49	84.71	7.18×10^9
OF 3	-18736.03	1129.44	78.50	6.16×10^9
OF 4	-21153.43	1946.28	79.26	6.97×10^9

A.3.1.2. Evaluation of Prepared Film Variants using Experimental Methods

On the basis of the physical examination carried out, the film formulations were whitish in color with OF 1, OF 3 and OF 4 (Figures A.4a, 4c and 4d) showing visible surface segregation and non-homogeneity while OF 2 (Figure A.4) appears to be the most physically homogenous and continuous surfaced formulation. The film formulations can be described as thin, light-weighted and flexible with thicknesses ranging between 161.67 µm and 272.67 µm and masses which spanned from 39.33 mg to 59.57 mg. The discrepancies observed in the formulation thicknesses and masses are mainly dependent on the levels of excipients and active drug present within the matrix (Table A.1) Amongst the four formulations, OF 2 had the narrowest weight and thickness differences based on the calculated standard deviation (Table A.3) and this can be associated with its displayed uniform surface integrity (Figure A.4).

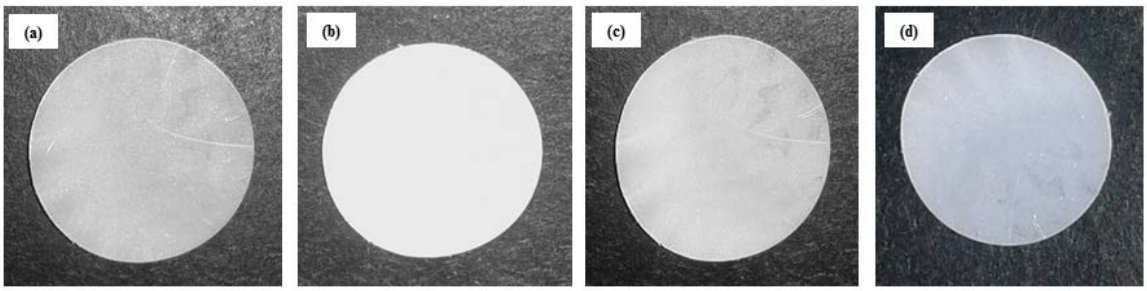

Table A. 3 *In-vitro* analyses of the PYZ-loaded film formulations

Experimental Outputs	PYZ Film Formulations			
	OF 1	**OF 2**	**OF 3**	**OF 4**
Mass (mg)	59.57 ± 2.75	39.33 ± 1.12	40.30 ± 1.54	57.20 ± 3.65

Figure A. 4 Digital photographs showing the observed surface appearance of the film formulations: (a) OF 1, (b) OF 2, (c) OF 3 and (d) OF 4.

Thickness (µm)	272.67 ± 31.18	166.00 ± 5.20	161.67 ± 10.59	245.00 ± 17.78
$t_{disintegration}$ (seconds)	57.00 ± 1.64	56.49 ± 3.49	61.83 ± 3.81	109.04 ± 4.50
$t_{dissolution}$ (minutes)	20.27 ± 0.60	9.96 ± 0.80	11.43 ± 1.17	12.78 ± 0.94
$pH_{dissolution}$	6.51 ± 0.04	6.70 ± 0.01	6.31 ± 0.06	6.24 ± 0.02
Drug content (%w/w)	98.00 ± 3.07	98.04 ± 1.31	98.46 ± 1.55	94.37 ± 4.32

The films collapsed and dissolved quite quickly with OF 2 displaying the lowest disintegration (56.49 ± 3.49 secs) and dissolution times (9.96 ± 0.80 mins) (Table A.3) which is also confirmed by the simulated robust intermolecular interactions between OF 2 and water molecules (representing simulated saliva) measured with the *S* and *CED* highlighted in Table A.2. Also, some interesting trends were noted for OF 1 and OF 4. With OF 1, the film structure collapsed quite quickly ($t_{disintegration}$ = 57.00 ± 1.64 secs) while its complete dissolution was the most prolonged phase ($t_{dissolution}$ = 20.27 ± 0.60 mins). This suggests that a level of polymeric swelling may have occurred after the rapid wetting/hydration phase leading to a delay in the duration of complete solvation of the formulation. OF 4 on the other hand exhibited a delayed strucutral collapse ($t_{disintegration}$ = 109.04 ± 4.50 secs) which was then followed by a quite rapid dissolution phase ($t_{dissolution}$ = 12.78 ± 0.94 mins) compared to the other formulations. A noticeable decrease in the

pH of simulated saliva (pH 6.8) was displayed by the formulations (Table A.3) However, solvated OF 2 still had pH values closest to the pH (6.70 ± 0.01) of simulated saliva. This can be as a result of the citric acid content of the film variants. However, the impact of citric acid content of each film on the pH of simulated saliva seems to be significantly influenced by the other excipients and PYZ as no particular pattern is observed. The drug loading potential of the four films can be described as high with the standard deviations values showing the uniformity of distribution of the PYZ molecules within the film matrix. The films exhibited varibilities at different levels and OF 2 showed the least variability in PYZ content (Table A.3) which is consistent with its observed *in silico* stability and *in-vitro* surface uniformity and constancy. Furthermore, the surface geometry of the film formulation were visualized using the scanning electron microscopic analysis. All obtained surfaces can be described as bi-layered with OF 2 possessing the most well-defined and robust surface configuration while OF 1, OF 3 and OF 4 have quite irregular surface geometries (Figure A.4).

A.3.1.3. Measures for Selecting the Optimal Film Formulation

The optimized oral film was carefully chosen based on findings obtained from the *in silico* arithmetics and *in-vitro* experiments. Considering computational outputs, the film that displayed minimum total interaction energy, high solubility parameter, maximum cohesive energy density and intermediate kinetic energy was desirable (Table A.2). In view of the *in-vitro* experiments, the formulation which showed the lowest dissolution and disintegration times, dissolution pH closest to that of saliva, light weight with minimal variation, relatively regular slim dimension, high and uniform drug loading

capacity (Table A.3) and well-layered surface morphology (Figure A.5) was considered. On these grounds, OF 2 was selected as the optimal formulation for further characterization because it complied with all the outlined specifications.

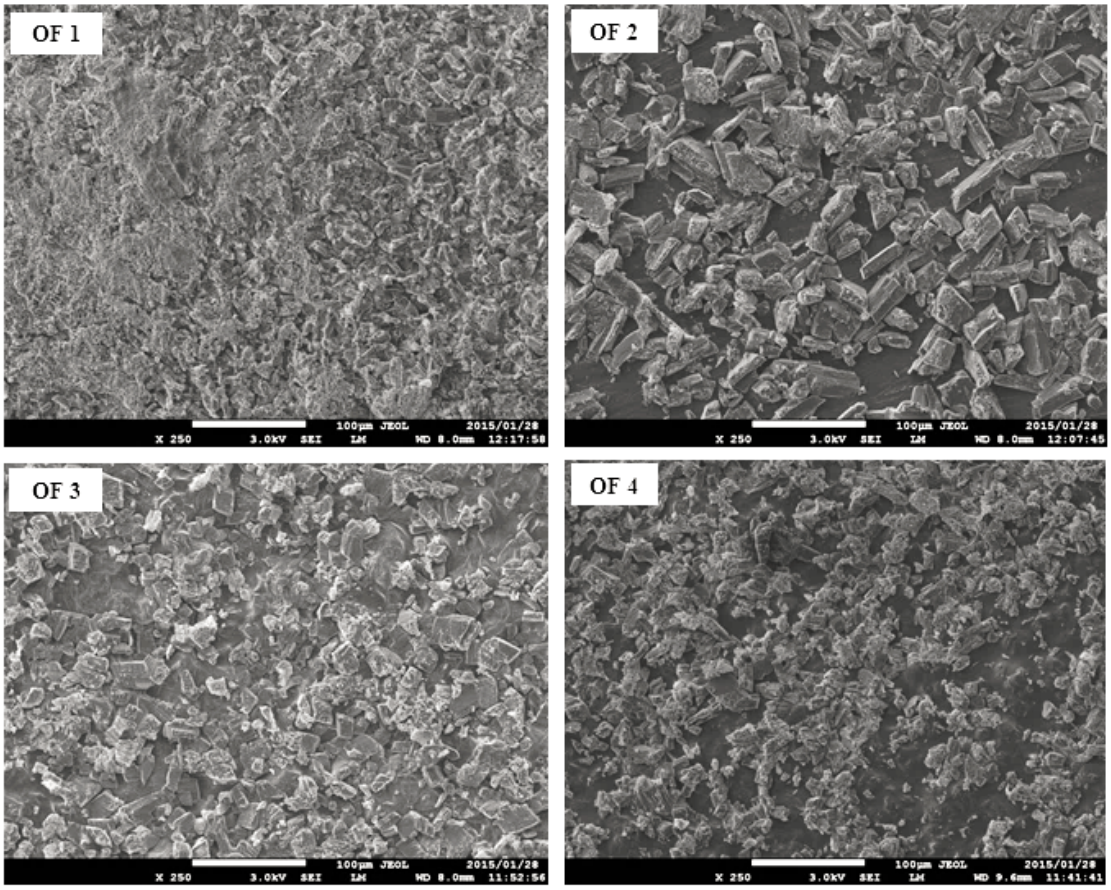

Figure A. 5 Scanning electron micrographs showing the surface topography of the OF 1, OF 2, OF 3 and OF 4 formulations respectively (magnification 250×).

A.3.2. Characterization of the Chosen Optimal Formulation

A.3.2.1. *In-vitro* Drug Release and Kinetics

To date, no standardized official guidelines exist for assessing the drug release behavior of rapidly disintegrating oral films.[13] This study employed a modified petri dish approach conducted under timed, biorelevant conditions described earlier. The pattern of PYZ release from the OF 2 formulation in simulated saliva can be described as monophasic with a consistent increase in the amount of the PYZ released over time. 100% PYZ release was attained in about 30 minutes (Fig. A.6). The release kinetics of PYZ from the OF 2 formulation were assessed employing the zero order, first order, Korsmeyer-Peppas and Higuchi mathematical models (eq 1 – eq 4). Measured parameters included the intercept (*a*), slope (*b*) and the correlation coefficient (R^2) (Table A.6). The point of best fit was based on the value of R^2 closest to one. The R^2 values obtained for each model fitting analysis is also presented in Table A.6.

The drug release mechanism of the OF 2 formulation was best explained with the zero order (R^2 = 0.97) and Korsmeyer-Peppas (R^2 = 0.99) mathematical models as the profile displayed the highest linearity employing these models. The fit of the PYZ release profile into the zero order model suggests that PYZ release from the OF 2 formulation remained consistent until 100% drug liberation was achieved and was independent of the residual PYZ concentration at any time-point. Focusing on the Korsmeyer-Peppas model characterized with the highest R^2 value, PYZ release behavior from the polymer-based OF 2 formulation can be further described as being dependent on the film matrix dynamic swelling and eventual dissolution.[38,40] In addition, the calculated *n* value (eq 3) described as the release exponent was 1.06 which indicates a $n > 0.89$ instance. Consequently, the release mechanism of the PYZ molecules from the OF 2 matrix can be further described as a super case-II transport[39,41] which shows that PYZ release from the polymer-based OF

2 matrix was regulated by swelling, diffusion and relaxation/disentanglement/erosion processes which validates the zero order kinetic behavior explained previously.

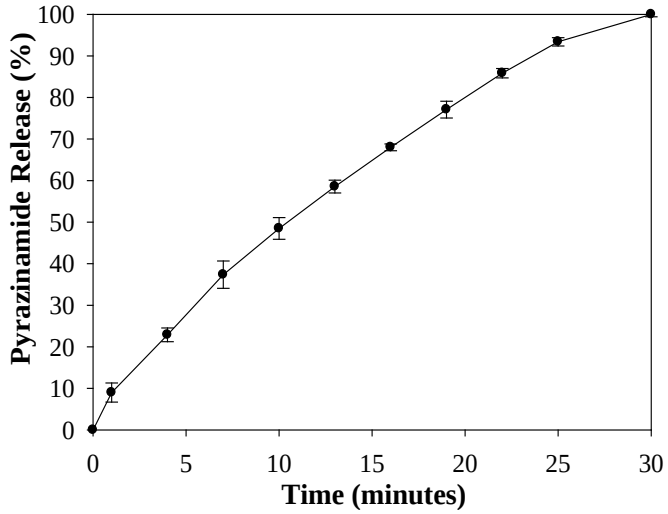

Figure A. 6 Dissolution profile of the PYZ-loaded OF 2 formulation in simulated saliva under biorelevant conditions (n=3 and standard deviation ≥ 3.28% in all cases).

Table A. 4 Outputs of the mathematical model fitting of the OF 2 drug release profile

Mathematical Model	*a*	*b*	R^2
Zero order	3.37	9.57	0.97
First order	0.42	-4.14	0.26
Korsmeyer-Peppas	1.06	1.40	0.99
Higuchi	0.50	1.43	-1.21

A.3.2.2. X-ray Diffraction Patterns

The powder XRD diffractogram of the OF 2 formulation is shown in Figure A.7(a). Figure A.7(b) illustrates an expanded view of the salient peaks of the encircled portion of Figure A.7(a). The recorded diffraction patterns (Figures A.7(a) and A.7(b))

showing many blunt and a few sharp peaks confirms that the OF 2 formulation was made up of multiple components which were physically mixed as a result of non-destructive reversible interactions amongst the constituent atoms and molecules. The intermittent low and high intensity sharp peaks observed at 1.27, 17.20, 27.28, 29.44 and 32.78 (2θ) can be related to the presence of crystalline components namely pyrazinamide[42], citric acid[43] and glycerol[44] which are contained at lower levels relative to Kollicoat®IR in formulation OF 2 (Table A.1). The presence of Kollicoat®IR, a semi-crystalline polymer[45,46], within the OF 2 matrix could also have contributed to the sharp crystalline peaks recorded in the diffractogram especially the high intensity peak situated at 1.27 (2θ) as well as the wide spread, broad bands located at different points on the diffractogram (Figures A.7(a) and A.7(b)). Furthermore, Janssens *et al*. reported an investigation which further confirms that the major broad bands are characteristic of Kollicoat®IR especially the extended blunt peak situated around 19.7 (2θ).[47] Visualizing the whole diffractogram (Figures A.(a) and A.7(b)), OF 2 appears to be predominantly amorphous in nature which explains the quite rapid release behavior (Table 3 and Figure 6) characterized with a well-controlled and consistent release characteristic which may be as a result of the presence of the intermittent crystalline domains (Figures A.7(a) and A.7(b)) which potentially reinforced the whole OF 2 frame.

A.3.2.3. Thermal behavior

The DSC scan generated for the pure PYZ and OF 2 formulation are presented in Figures A.7(c) and A.7(d) respectively. The sharp melting endotherm observed at 190.93°C in Figure A.(c) confirms the purity and crystallinity of PYZ.[42] The multiple thermal peaks noted on the scan recorded for OF 2 (Figure A.7(d)) shows that it

contains multiple, physically combined component molecules. The broad nature of the endothermic and exothermic peaks generated for OF 2 (Figure A.7(d)) shows that the matrix is semi-crystalline in nature. These outcomes further corroborate the finding of the XRD analysis. The major indicators of thermal activities and transitions considered for this analysis are the glass transition temperature (T_g), crystallization temperature (T_c) and the melting temperature (T_m). Focusing on Figure A.7(d), the melting temperature of PYZ shifted slightly from 190.93°C (Figure A.7(d)) in its pure state to 189.32°C which is still within the reported range in literature.[42] Minor changes in the melting points of glycerol[48] (18.17°C) and citric acid (153°C) to 19.27°C and 148.04°C respectively were noted. A reversible endothermic glass transition peak characteristic of the polymeric component was recorded at 48.37°C. Subsequently, an exothermic crystallization peak characteristic of the polymer was also noted at 124.71°C followed by another exothermic peak at 175.11°C which may be attributable to the initiation of melting of some residual components within the OF 2 matrix. Melting continued as other exothermic peaks were recorded at 189.32°C (for pyrazinamide), 208.52°C (Kollicoat® IR) and the eventual decomposition of the OF2 matrix beyond 210°C (Figure A.7(d)).

A.3.2.4. Elucidation of structural features

Characteristic FTIR peaks at specific vibrational frequencies representing functional moieties that are typical of each component molecule contained in OF 2 were studied (Figure A.7(f)). The different peaks considered for evaluation are presented in Table 5.

Changes in the band frequencies recorded for the functional moieties peculiar to each compound were within standard limits (Table 5) indicating that the processes employed for the production of the OF 2 formulation were based on physical interactions. Furthermore, very slight variations were noted with the characteristic band frequencies recorded for the pure PYZ and PYZ-loaded onto the OF 2 matrix. Overall, the generated FTIR spectra for OF 2 showed that the matrix was made up of a stable mixture of multiple compounds as common bands overlapped and some shifts were recorded in terms of frequency magnitudes and transmittance intensities as a result of the influence of other compounds present within the same formulation.

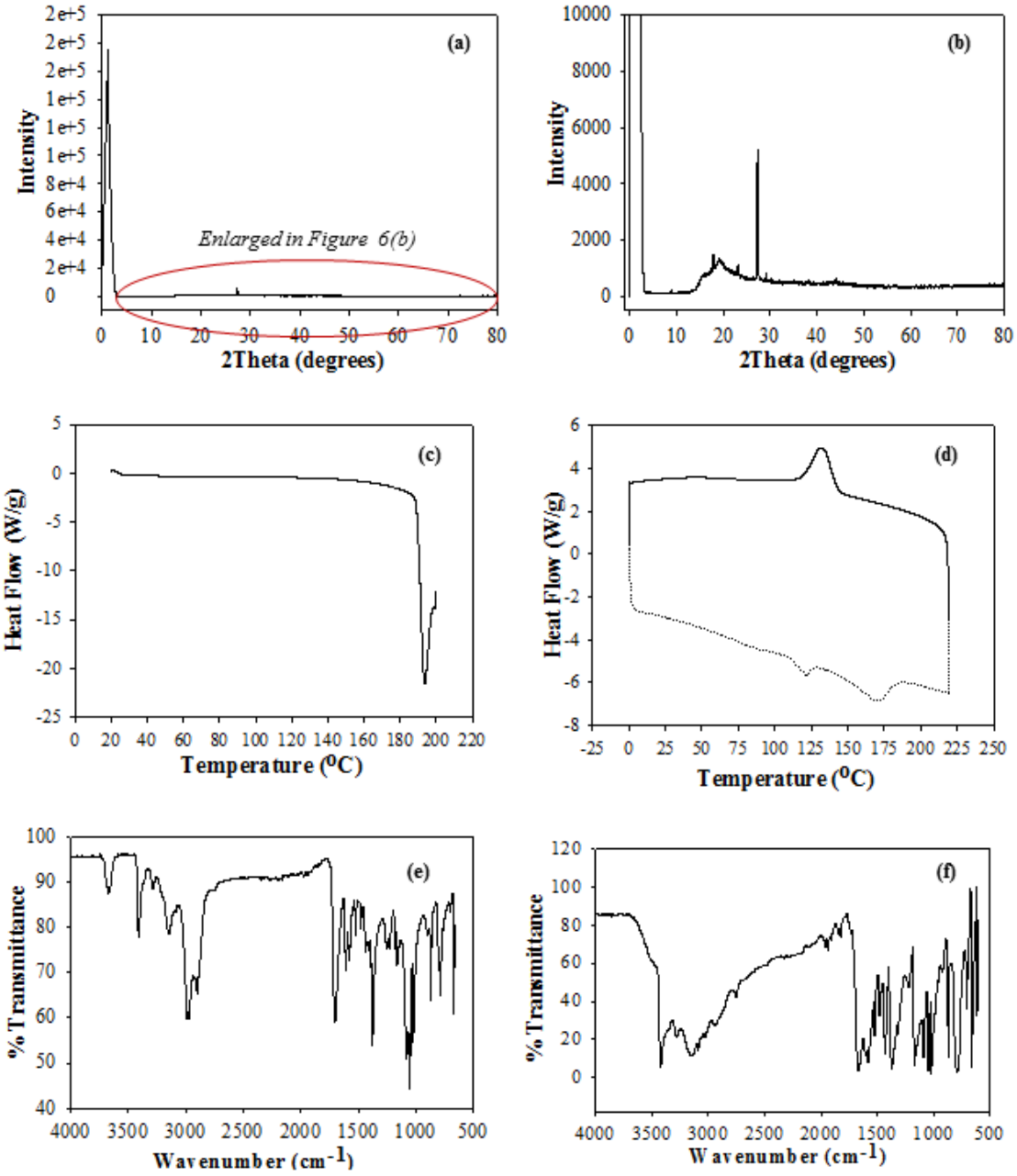

Figure A. 7 *In vitro* physicochemical characterization outcomes illustrating: (a) OF 2 XRD diffractogram, (b) enlarged depiction of the encircled portion in (a), (c) DSC plot for pure PYZ, (d) DSC plot for OF 2, (e) FTIR spectrum for pure PYZ and (f) FTIR spectrum for OF 2.

Table A. 5 A highlight of the vibrational frequencies of the respective salient functional moieties of the respective OF 2 component compounds

Compound	Salient Functional Moieties	Reference Vibrational Frequency (cm^{-1})[49-51]	Measured Vibrational Frequency in OF 2 formulation (cm^{-1})
Kollicoat® IR	-C-O-C *stretch*	1150-1050	1089.47
	-C-H_2 (methylene):		
	asymmetric stretch	2935-2915	2925.91
	symmetric stretch	2865-2845	2842.72
	bend	1485-1445	1480.68
	rocking	750-720	732.58
	-C-O- (hydroxy) *stretch*	~1050	1046.16
	-O-H (polymeric) *stretch*	3400-3200	3422.97
	-C-H (methane):	2900-2880	2854.20
	stretch	1350-1330	1348.44
	bend		
	-C-C vibrations (skeletal)	1300-700	1171.81, 1021.78, 790.63
Citric acid	-C-O- (tertiary) *stretch*	~1150	1158.67
	-O-H (tertiary) *stretch*	2500-3300	3089.98
	-O-H (tertiary) *bend*	1410-1310	1373.37
	-C-O-H	1400-1440	1432.11
Glycerol	-C-O- (secondary) *stretch*	~1100	1111.66
	-O-H (tertiary) *stretch*	3620-3540	3529.87
	-O-H (tertiary) *bend*	1410-1310	1316.48
	-C-H (methylene):	2935-2915	2936.70
	asymmetric stretch	2865-2845	2854.20 (overlap)
	symmetric stretch	1485-1445	1480.68 (overlap)
	bend	750-720	732.58 (overlap)
	rocking		
Pyrazinamide	-N-H- *stretch*	3400-3380 and 3345-3325	3339.97 (3399.00)*
	-N-H- *wag*	910-665	693.90 (708.39)*
	-C=O	1665-1760	1669.66 (1680.65)*
	-C-N- (secondary) *stretch*	1190-1130	1147.23 (1158.61)*
			1336.48 (1371.98)*

-C-N- (cyclic) *stretch*	1360-1280	1680.65 (1704.13)*
-C=C- (cyclic)	1620-1680	1656.47 (1645.09)*
-C=N- (cyclic)	1650-1680	

*__Note__: Vibrational frequencies recorded for pure PYZ (Figure 6(e))

A.3.2.5. Permeation of PYZ through the Porcine Buccal Tissue

The permeation pattern of the PYZ-loaded OF 2 formulation over 120 minutes is graphically depicted in Figure A.8(a). Plots of calculated steady state flux and permeability coefficient are also represented with Figures A.8(b) and A.8(c). PYZ permeation through the porcine tissue can be described as two-phased with an initial rapid penetration phase of about 32.06% within the first minute and subsequently relatively consistent permeation pattern from 20 -120 minutes. Overall, a total of 78.32% of PYZ permeated through the porcine tissue in 120 minutes. The initial spike in the permeation trend of PYZ can be related to the highest value steady state flux and permeability coefficient values (Figure A.8(b) and A.8(c)). Afterwards, a sharp decrease in the steady state flux due to a decrease in permeability coefficient followed leading to the relatively constant, plateau-type release pattern recorded from around 20 minutes and beyond (Figure A.8(a)).

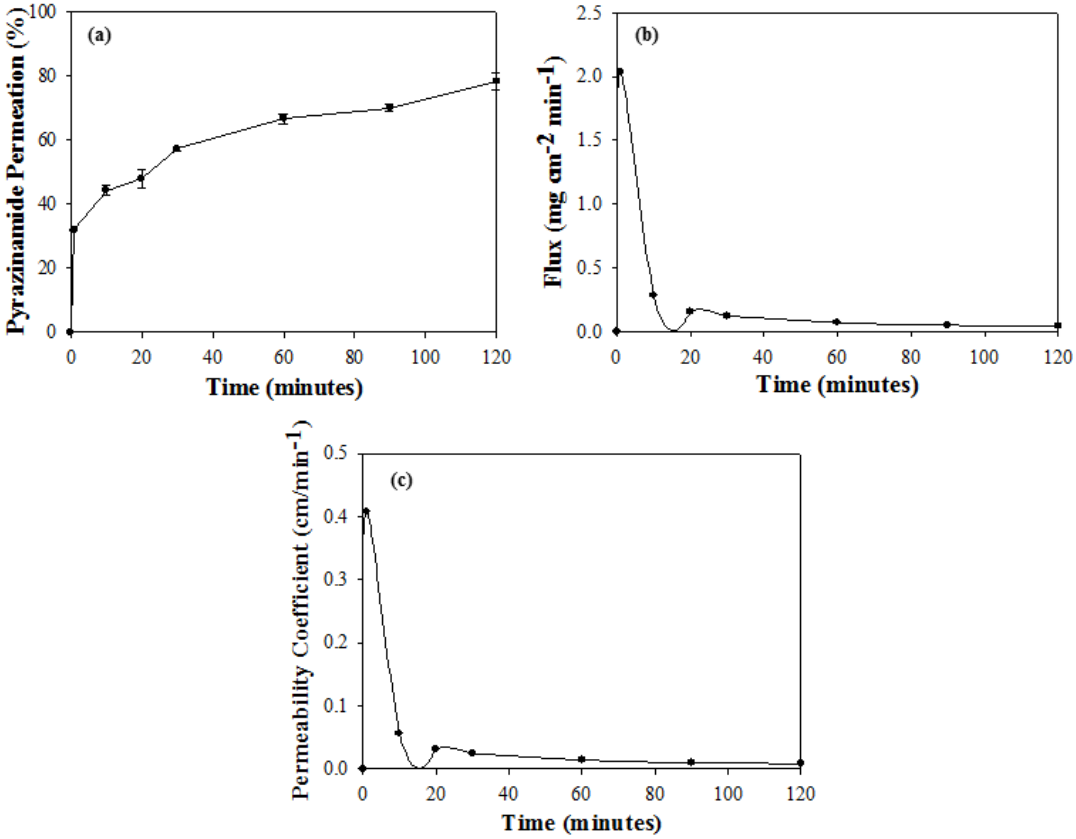

Figure A. 8 Graphical representations of: (a) *Ex vivo* permeation of PYZ molecules from formulation OF 2 through the porcine buccal mucosa (standard deviation ≤ 2.89% in all cases), (b) steady state PYZ flux (standard deviation ≤ 2.89 × 10^{-2} mg/cm^2/min in all cases), (c) permeability coefficient (standard deviation ≤ 1.30× 10^{-3} cm/min in all cases) (n = 3 in all cases).

A.3.2.6. Experimental and Computed Values of Mechanical Properties

The European Pharmacopoeia recommends that orodispersible film formulations should have appropriate mechanical strength to prevent damage during physical handling.[13] The numerical values of the experimentally measured mechanical parameters namely force at break, percentage strain (measure of elongation), tensile strength and Young's modulus are presented in Table A.6. In addition, the calculated values for the

assessed *in silico* mechanical measures are presented in Table A.6. The COMPASS force field is a reliable and useful tool for calculating and studying physicochemical and physicomechanical properties of a wide-range materials.[16,22] Its stability and applicability has also been ascertained from the above-mentioned experimentally validated outcomes of this study. Overall, OF 2 displayed good and quantifiable physicomechanical strength parameters in terms of its rigidity/resistance to deformation, robustness, compressibility and flexibility quantified by the measured and calculated mechanical properties listed in Table A.6.

Table A. 6 Experimental and calculated mechanical properties

Mechanical Properties	**Numerical Values**
Experimental Parameters	
Force at break (N)	2.90 ± 0.89
Elongation (%)	12.65 ± 1.32
Tensile strength (MPa)	2.34 ± 0.61
Young's modulus (MPa)	48.57 ± 3.01
Calculated Parameters	
Bulk modulus (MPa)	3.93×10^3
Shear modulus (MPa)	1.43×10^3
Compressibility (1/TPa)	270.66
Sound velocity (m/sec)	2.46
Lamé constants (MPa)	4.55 (Lambda), 8.76 (Mu)
Viscosity (cP)	0.29
Bulk density (g/cm^3)	0.81
Young's modulus (MPa)	42.92

A.3.3. Assessment of Optimal Formulation Stability

The stability of the OF 2 formulation was evaluated employing both experimental and computational methods.

Stability tests are fundamental tools employed throughout the different developmental phases of pharmaceutical formulations for investigating the influence of varying storage condition on their safety, quality and efficacy.[52,53] This provides better understanding of how the quality of the active drug or drug product differs under varying common environmental storage condition (e.g. temperature, humidity, light etc.). For a well-established stability testing, relevant stability indicators (physical, chemical, biological etc.) need to be checked. The stability indicators generated for the respective formulations can be employed in determining the most suitable storage, packaging and shelf life.[52-54]

A.3.3.1. Short-Term Stability Testing Utilizing an Experimental Approach

The stability indicators measured after storing OF 2 in transparent, closed glass vials for 14 days are dissolution and disintegration time, drug content uniformity, film thickness and mass (Table A.7). Comparing the numerical values of the stability indicators of the freshly prepared versus the stored formulation, OF 2 can be described as potentially stable under controlled room conditions (temperature: 23 ± 3°C; humidity: 65 ± 5%).

Table A. 7 Experimental stability indicators for OF 2

Stability indicators	OF 2 (freshly prepared)	OF 2 (after 14 days)
$t_{disintegration}$ (seconds)	56.49 ± 3.49	60.00 ± 2.01
$t_{dissolution}$ (minutes)	9.96 ± 0.80	9.97 ± 0.72
Drug content (%w/w)	98.04 ± 1.31	97.99 ± 1.67
Film thickness (µm)	166.00 ± 5.20	169.01 ± 3.99
Film mass (mg)	39.33 ± 1.12	38.81 ± 0.98

A.3.3.2. Studying the Stability Patterns of the OF 2 Formulation using in silico Analyses

Computer assisted calculations were performed to provide more in-depth understanding of the stability patterns of the OF 2 formulation and predict its most suitable storage conditions. *In silico* calculations were based on the impact of varying values of *in silico* environmental pressure, temperature and humidity on the OF 2 systemic E_T values. As mentioned earlier, the E_T is a measure of the intrinsic *in silico* stability of the system with an increase in its magnitude indicating an increase in the system's instability while the reverse is the case with a decrease in the E_T value. For computational measurements involving changes in pressure and temperature, 0.1 MPa and 25°C were respectively selected as references points for comparative purposes. Figures 8(a) and 8(b) illustrate the changes in the magnitude of E_T as temperature and pressure varied respectively. With reference to the 25°C point (E_T = -5725.12 kcal/mol), an increase in temperature from 30°C to 60°C generally increased the magnitude of E_T (-5540.55 kcal/mol to -4824.47 kcal/mol) (Figure 8). In other words, the intrinsic stability of the OF 2 matrix was predicted to decrease as the environmental temperature increased indicating an upsurge in the degree of disorderliness within the system's internally stable

and robust configuration. On the contrary, a decrease in the *in silico* environmental temperature reduced calculated E_T from -5725.12 kcal/mol at 25°C to -5867.17 kcal/mol and -5756.58 kcal/mol at 5°C and 0°C respectively. On the basis of the computer-aided extrapolations, the storage of the OF 2 formulation at temperatures between 0°C and 25°C would be the best for maintaining optimum stability. Studying the generated calculations for the impact of variations in *in silico* environmental pressure on the E_T, no definite trend was observed. However, it can be inferred from the outputs that at a surrounding pressure equal to or less than 1000 MPa, the value of E_T was generally lower demonstrating better internal stability compared to when the environmental pressure was above 1000 MPa (Figure A.9(b)). Ultimately, the computational outcomes indicate that storing the OF 2 formulation in a surrounding with controlled and preferably lower environmental pressure values will be most appropriate to mainitain optimum stability. The calculated outputs generated for the influence of exposure to different concentrations of water molecules on the stability of the OF 2 matrix showed no particularly methodical pattern. To sum up, Figure A.9(c) shows that between the 0.68%w/w and 67.49%w/w hydration points, the magnitude of E_T was lower relative to hydration points above 67.49%w/w, which is characterized by high E_T values indicating the level of intrinsic instability within the OF 2 matrix. Based on the outcomes of the computerized calculations illustrated in Figure A.9(c), OF 2 is sensitive to humidity changes and it will be best to store it within an environment with controlled and low (< 65%) humidity levels. Overall, the calculated stability studies results aligned well with the outcome of the short term experimental analysis conducted under room temperature, humidity and pressure conditions.

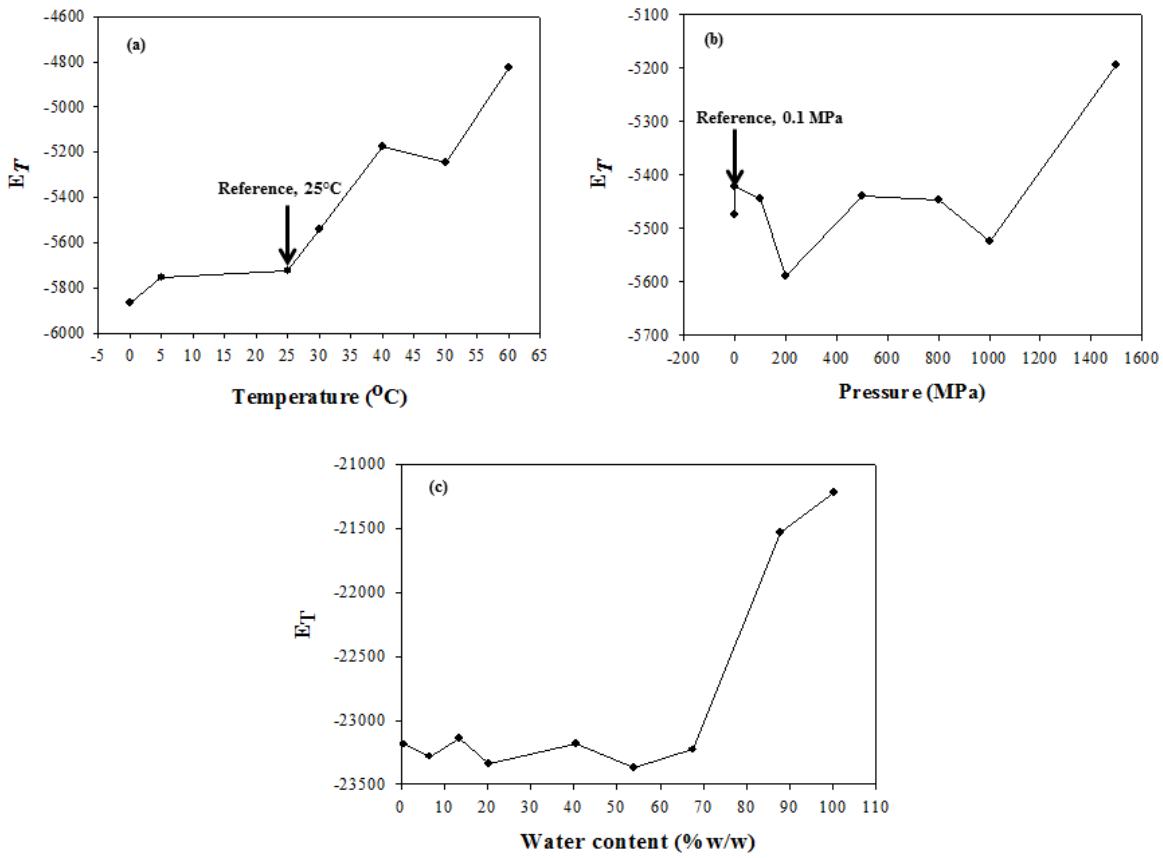

Figure A. 9 Plots showing the impact of changes in calculated: (a) temperature and (b) pressure on the magnitude of the E_T within the OF 2 matrix employing room temperature (25°C) and pressure (0.1 MPa) as reference points.

A.3.4. *In-vitro* Cytotoxicity Assay

Graphical representations of the mean percentage cell viability with standard deviation of each HDF cell culture to free PYZ, PYZ-loaded OF 2 and placebo OF 2 are presented in Figures 9(a), 9(b) and 9(c). In general, the percentage viability of the HDF cells was higher at the 24 hour time-point compared to the 48 hours period. At both 24 and 48 hour, at drug concentrations of 2.5 and 5 mg/mL, free PYZ showed significantly lower viability

compared to the PYZ-loaded OF 2 and placebo OF 2 film. However, free PYZ enhanced cell growth over 48 hours except at the highest concentration (5 mg/mL) level where a statistically significant (*p<0.05*, Student's T test) reduction was noticed (from 100% to 67.39% at 24 hours and 60.67% at 48 hours). The PYZ-loaded and placebo OF 2 formulation at all test concentrations had no toxic effect on the HDF at 24 hours and 48 hours. Placebo OF 2 with film concentration of 1.25-10 mg/mL had significant increase of viability compared to 20 mg/mL. Overall, it can be concluded that the placebo OF 2 and PYZ-loaded OF 2 formulations are potentially non-cytotoxic and biocompatible to HDF.

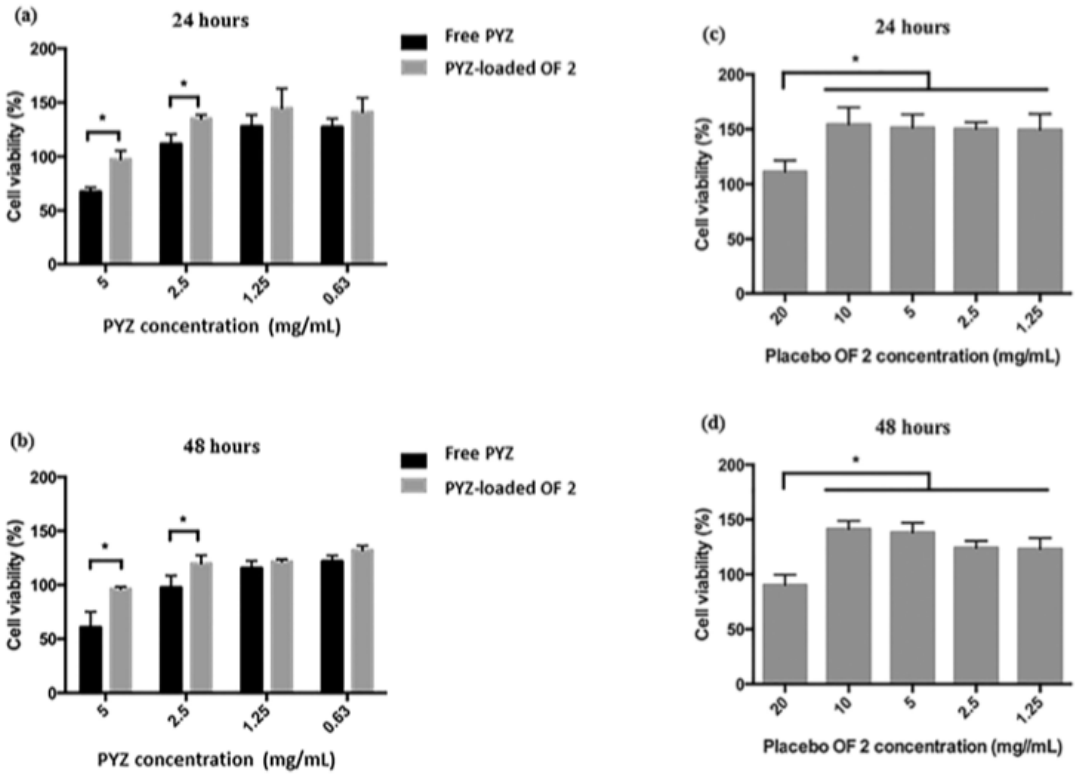

Figure A. 10 Graphical representations of the percentage viability of the HDF cell line after exposure to the free PYZ, PYZ-loaded OF 2 and placebo OF 2 over (a) 24 hours and (b) 48 hours (represented data from two independent experiment, n=3). * indicates statistical significant difference at p<0.05, Student's T-test (a) (b) and ANOVA-Dunnett's test (c).

A.4. CONCLUSION

This study investigated the construction, screening, optimization and evaluation of novel rapidly disintegrating oral film formulations containing PYZ employing both experimental methods and atomistic molecular simulations. The fabrication and optimization of the oral film variants were based on computer-assisted molecular calculations and the one-variable-at-a-time experimental approach. Computed outputs were well related to experimental results. The selected thermodynamically stable PYZ containing oral film formulation (OF 2) had characteristically low E_T, moderate E_K, high *S* and *CED* values as well as low dissolution and disintegration times, dissolution pH bordering that of saliva, minimally varied light weight, slim-nature, high and uniformly distributed drug content and relatively evenly distributed surface topography. Furthermore, the optimal film formulation, OF 2, was physically and mechanically robust, homogenous in appearance and displayed release kinetics centred on the Korsmeyer-Peppas and zero-order models. XRD assessment showed that OF 2 was semi-crystalline in nature with a predominance of the amorphous domains, which explained its rapid but well controlled release behaviour. Besides, the XRD, DSC and FTIR evaluations revealed that the assembling of the OF 2 matrix is as a result of the non-destructive, physical interactions amongst its component compounds. The OF 2 formulation maintained the permeation of PYZ molecules through the porcine buccal tissue and showed no significant toxic effect upon exposure to the HDF cell line. Both calculated and experimentally determined physicomechanical parameters showed that OF 2 possessed noticeable inherent strength and flexibility. The *in silico* and *in-vitro* stability examinations showed that the OF 2 formulation was stable under carefully regulated

environmental (temperature, pressure and humidity) conditions. Overall, the capability of the high performance atomistic molecular modeling approach to provide in-depth understanding of the physicochemical and physicomechanical properties as well as facilitate the screening and optimization of drug delivery systems/pharmaceutical formulations was well established.

A.5. ACKNOWLEDGEMENTS

This work is financially supported by grants from the William J. Fulbright; National Research Foundation/Department of Science and Technology, South Africa and L'Oréal-UNESCO for Women in Science. Thanks to the New Jersey Centre for Biomaterials, Rutgers-The State University of New Jersey; the Encapsulation and Delivery Division and National Centre for Nano-Structured Materials of the Council for Scientific and Industrial Research (CSIR), South Africa for provision of research facilities. The authors would also like to thank the Centre for High Performance Computing, CSIR, South Africa for provision of computing resources and complimentary funds.

A.6. REFERENCES

1. World Health Organization. *WHO Global Tuberculosis Report*. 2013; 2013.
2. Aziz, M. A.; Wright, A.; Laszlo, A.; De Muynck, A.; Portaels, F.; Van Deun, A.; Wells, C.; Nuun, P.; Blanc, L.; Raviglione, M. Epidemiology of antituberculosis drug resistance (the global project of antituberculosis drug resistance surveillance): an updated analysis. *Lancet*. 2006, *368* (9553), 2142-2154.
3. Shahid, S. K. Newer patents in antimycobacterial therapy. *Pharm. Pat. Anal.* 2015, *4* (3), 219-238.
4. Garg, T.; Rath, G.; Goyal, A. K. Current nanotechnological approaches for an effective delivery of bioactive drug molecules to overcome drug resistance tuberculosis. *Curr. Pharm. Des.* 2015. (In press).
5. Garcia-Contreras, L.; Sung, J.; Ibrahim, M.; Elbert, K.; Edwards, D.; Hickey, A. Pharmacokinetics of inhaled rifampicin porous particles for tuberculosis treatment:

Insight into rifampicin absorption from the lungs of guinea pigs. *Mol. Pharm.* 2015. (In press).
6. World Health Organization. *WHO Global Tuberculosis Report*. 2014; 2014.
7. World Health Organization. Treatment of tuberculosis guidelines. 2010. *Fourth Edition*. http://whqlibdoc.who.int/publications/2010/9789241547833_eng.pdf (06/03/2015).
8. Nuermberger, E. L.; Spigelman, M. K.; Yew, W. W. Current development and future prospects in chemotherapy of tuberculosis. *Respirology*. 2010, *15* (5), 764-778.
9. Becker, C.; Dressman, J. B.; Amidon, G. L.; Junginger, H. E.; Kopp, S.; Midha, K. K.; Shah, V. P.; Stavchansky, S.; Barends, D. M. Biowaiver monographs for immediate release solid oral dosage forms: Pyrazinamide. *J. Pharm. Sci.* 2008, *97* (9), 3709-3720.
10. Momekov, G.; Ferdinandov, D.; Voynikov, Y.; Stavrakov, G.; Peykov, P. Pyrazinamide – Pharmaceutical, biochemical and pharmacological properties and reappraisal of its role in the chemotherapy of tuberculosis. *Pharmacia*. 2014, *61* (1), 38-67.
11. Pyrazinamide. *Tuberculosis*. 2008, *88* (2), 141-144.
12. Pham, D.-D.; Fattal, E.; Ghermani, N.; Guiblin, N.; Tsapis, N. Formulation of pyrazinamide-loaded large porous particles for the pulmonary route: Avoiding crystal growth using excipients. *Int. J. Pharm.* 2013, *454* (2), 668-677.
13. Brniak, W.; Maślak, E.; Jachowicz, R. Orodispersible films and tablets with prednisolone microparticles. *Eur. J. Pharm.Sci.* 2015, *75*, 81-90.
14. Borges, A. F.; Silva, C.; Coelho, J. F. J.; Simões, S. Oral films: Current status and future perspectives I – Galenical development and quality attributes. *J. Control Release*. 2015, *206*, 1-19.
15. Wagh, M. A.; Dilip, K. P.; Salunkhe, K. S.; Chavan, N. V., Daga, V. R. Techniques used in orally disintegrating drug delivery system. *Int. J. Drug. Deliv.* 2015, *2*, 98-107.
16. Razmimanesh, F.; Amjad-Iranagh, S.; Modarress, H. Molecular dynamics simulation study of chitosan and gemcitabine as a drug delivery system. *J. Mol. Model.* 2015, *21* (7), 165.
17. Adeleke, O. A.; Choonara, Y. E.; du Toit, L. C.; Kumar, P.; Pillay, V. *In vitro*, *ex vivo*, and *in silico*, mechanistic elucidation of the performance of an optimized porosity-controlled multi-elemental transbuccal system. *Pharm. Res.* 2015, *32* (7), 2384-2409.
18. Tian, Y.; Shi, C.; Sun, Y.; Zhu, C.; Sun, C. C.; Mao, S. Designing micellar nanocarriers with improved drug loading and stability based on solubility parameter. *Mol. Pharm.* 2015, *12*, 816-825.
19. Tokarský, J.; Andrýsek, T.; Čapková, P. Molecular modeling of gel nanoparticles with cyclosporine A for oral drug delivery. *Int. J. Pharm.*2011, *410*, 196-205.
20. Macháčková, M.; Tokarský, J.; Čapková, P. A simple molecular modeling for the characterization of polymeric drug carriers. *Eur. J. Pharm. Sci.* 2013, *48* (1-2), 316-322.
21. Wang, X-Y.; Zhang, L.; Wei, X-H.; Wang, Q. Molecular dynamics of paclitaxel encapsulated by calicylic acid-grafted chitosan oligosaccharide aggregates. *Biomaterials*. 2013, *34* (7), 1843-1851.

22. Hu, D.; Sun, S.; Yuan, P.; Zhao, L.; Liu, T. Evaluation of CO2-philicity of poly(vinyl acetate) and poly(vinyl acetate-alt-maleate) copolymers through molecular modeling and dissolution behaviour measurement. *J. Phys. Chem.* 2015, *119* (7), 3194-3204.
23. Yin, Q.; Zhang, L.; Jiang, B.; Qinjian, Y.; Du, K. Effect of water in amorphous polyvinyl formal: insights from molecular dynamics simulation. *J Mol Model*. 2015, *21* (2), 1-9.
24. Lou, H.; Liu, M.; Qu, W.; Hu, Z.; Brunson, E.; Johnson, J.; Almoazen, H. Evaluation of chlorpheniramine maleate microparticles in orally disintegrating film and orally disintegrating tablet for paediatrics. *Drug. Dev. Ind. Pharm*. 2014, *40* (7), 910-918.
25. Koland, M.; Charyulu, R. N.; Vijayanarayana, K.; Prabhu, P. In vitro and in-vivo evaluation of chitosan buccal films of ondasetron hydrochloride. *Int. J. Pharm. Investig.* 2011, *1* (3), 164-171.
26. Goudeau, S.; Charlot, M.; Vergelati, C.; Müller-Plathe, F. Atomistic simulation of the water influence on the local structure of polyamide 6, 6. *Macromolecules*. 2004, *37*(21), 8072-8081.
27. Mahajan, H. S.; Deshmukh, S. R. Development and evaluation of gel-forming ocular films based on xyloglucan. *Carbohyd. Polym.* 2015, *122*, 243-247.
28. Woertz, C.; Kleinebudde, P. Development of orodispersible polymer films with focus on the solid state characterization of crystalline loperamide. *Eur. J. Pharm. Biopharm.* 2015, *94*, 52-63.
29. Garsuch, V.; Breitkreutz, J. Comparative investigations on different polymers for the preparation of fast-dissolving oral films. *J. Pharm. Pharmacol.* 2010, *62*(4), 539-545.
30. Djekic, L., Martinovic, M., Stepanović-Petrović, R., Tomić, M., Micov, A., & Primorac, M. Design of Block Copolymer Costabilized Nonionic Microemulsions and Their In Vitro and In-vivo Assessment as Carriers for Sustained Regional Delivery of Ibuprofen via Topical Administration. 2015. *J. Pharm.Sci*. (In Press).
31. Yang, X., Trinh, H. M., Agrahari, V., Sheng, Y., Pal, D., & Mitra, A. K. Nanoparticle-Based Topical Ophthalmic Gel Formulation for Sustained Release of Hydrocortisone Butyrate. *AAPS PharmSciTech*. 2015. 1-13.
32. Dash, S.; Murthy, P. N.; Nath, L.; Chowdhury, P. Kinetic modeling on drug release from controlled drug delivery systems. *Acta Pol Pharm.* 2010. *67*(3), 217-23.
33. Giannola, L. I.; De Caro, V.; Giandalia, G.; Siragusa, M. G.; Tripodo, C.; Florena, A. M.; Campisi, G. Release of naltrexone on buccal mucosa: Permeation studies, histological aspects and matrix system design. *Eur. J. Pharm. Biopharm.* 2007. *67*, 425-433.
34. Taevernier, L.; Detroyer, S.; Veryser, L.; De Spiebeleer, B. Enniatin-containing solutions for the oromucosal use: Quality-by-design *ex vivo* transmucosal risk assessment of composition variability. *Int. J. Pharm.*2015. *491*, 144-151.
35. Adeleke, O. A.; Pillay, V.; du Toit, L. C.; Choonara, Y. E. Construction and in vitro characterization of an optimized porosity-enabled amalgamated matrix for sustained transbuccal drug delivery. *Int. J. Pharm.*2010. 3*91*, 79-89.
36. Saunders, S. R.; Anand, M.; You, S. S.; Roberts, C. B. Total interaction energy model to predict nanoparticle dispersability in CO_2-expanded solvents. *Comput. Aided Chem. Eng.* 2010. *28*, 1651-1656.

37. Huron, M. J.; Claverie, P. Calculation of the interaction energy of one molecule with its whole surrounding. I. Method and application to pure nonpolar compounds. *J. Phys. Chem.* 1972. *76*(15), 2123-2133.
38. Volkov, A.; Coppens, P. Calculation of electrostatic interaction energies in molecular dimers from atomic multipole moments obtained by different methods of electron density partitioning. *J. Comput. Chem.*2004. *25*(7), 921-934.
39. Singhvi, G.; Singh, M. Review: in-vitro drug release characterization models. *Int. J. Pharm. Stud. Res.* 2011. *2*(1), 77-84.
40. Korsmeyer, R.W.; Gurny, R.; Doelker, E.; Buri, P.; Peppas, N. A. Mechanisms of solute release from porous hydrophilic polymers. *Int. J. Pharm.* 1983. *15*(1), 25-35.
41. Walke, S.; Srivastava, G.; Nikalje, M.; Doshi, J.; Kumar, R.; Ravetkar, S.; Doshi, P. Fabrication of chitosan microspheres using vanillin/TPP dual crosslinkers for protein antigens encapsulation. *Carbohydr. Polym.*2015.*128*, 188-198.
42. Gad, S. Effect of a particle engineering process on polymorphic transition of pyrazinamide. *Int. J. Pharm. Pharm. Sci.* 2015. *7*(2), 581-584.
43. Apelblat A. Properties of citric acid and its solutions. In *Citric acid*. XII; Springer International Publishing.: Switzerland, 2014; pp 13-22.
44. Bermejo, F. J.; Criado, A.; de Andres, A.; Enciso, E.; Schober, H. Microscopic dynamics of glycerol in its crystalline and glassy states. *Phys. Rev. B.*1996. *53*(9), 5259-5267.
45. Guns, S.; Kayaert, P.; Martens J. A.; Van Humbeeck, J.; Mathot, V.; Pijpers, T.; Evgeny, Z.; Schick, C.; Van den Mooter, G. Characterization of the copolymer poly (ethyleneglycol-g-vinylalcohol) as a potential carrier in the formulation of solid dispersions. *Eur. J. Pharm. Biopharm.*2010. *74*(2), 239-247.
46. Litvinov, V. M.; Guns, S.; Adriaensens, P.; Scholtens, B. J. R.; Quaedflieg, M. P.; Carleer, R.; Van den Mooter, G. Solid state solubility of miconazole in poly [(ethylene glycol)-g-vinyl alcohol] using hot-melt extrusion. *Mol. Pharm.* 2012. *9*(10), 2924-2932.
47. Janssens, S.; de Armas, H. N.; Remon, J. P.; Van den Mooter, G. The use of a new hydrophilic polymer, Kollicoat® IR, in the formulation of solid dispersions of Itraconazole. *Eur. J. Pharm. Sci.* 2007.*30*(3), 288-294.
48. Lide, D. R. Ed. CRC Handbook of Chemistry and Physics. 88th ed.; CRC Press, Taylor & Francis.: Boca Raton, Florida, 2007-2008. , pp 3-268.
49. Coates, J. Interpretation of infrared spectra, a practical approach. In *Encyclopedia of Analytical Chemistry*, Meyers, R. A., Ed.; John Wiley and Sons Ltd.: Chichester, 2000; pp 10815-10837.
50. Silverstein, R. M. Bassler, G. C.; Morril, T. C., Ed. Spectrometric identification of organic compounds. Wiley.: New York, 1991; pp 91-131.
51. Sethia, S.; Squillante, E. Solid dispersions of carbamazepine in PVP K30 by conventional solvent evaporation and supercritical methods. *Int. J. Pharm.*2004. *272*, 1-10.
52. Kopp, S. Stability testing of pharmaceutical products in a global environment. *RAJ Pharma*. 2006. *May Edition*, 291-294.
53. Patel, A. R.; Vavia, P. R. Preparation and in-vivo evaluation of SMEDDS (self-microemulsifying drug delivery system) containing fenofibrate. *AAPS J.* 2007. *9*(3), E344-E352.

54. Guideline - ICH Harmonized Tripartite. Stability testing of new drug substances and products. *Current Step 4*. 2003.*Q1A* (R2), 1-14.